

**Density Variation with Time and Radius in a
Miniature Shock Tube Using X-ray Densitometry**

BY

RIZWAN A. SHAIK
B.E., Osmania University, Hyderabad, India, 2016

THESIS

Submitted as partial fulfillment of the requirements
for the degree of Master of Science in Mechanical Engineering
in the Graduate College of the
University of Illinois at Chicago, 2018

Chicago, Illinois

Defense Committee:

Patrick T. Lynch, Chair and Advisor, Mechanical and Industrial Engineering
Kenneth Brezinsky, Mechanical and Industrial Engineering
Alan L. Kastengren, Argonne National Laboratory

This thesis is dedicated to my parents, Arshed Sultana and Abdul Rahiman Shaik, without their unconditional love and support this would not have been possible.

ACKNOWLEDGEMENTS

I am truly grateful to my advisor Dr. Patrick T. Lynch for giving me the opportunity to carry out this research. His tremendous amount of support, patience and timely guidance at every step helped in completing this work.

I would like to thank my thesis committee members– Dr. Patrick T. Lynch, Dr. Kenneth Brezinsky and Dr. Alan Kastengren for agreeing to be a part of my committee. The guidance and useful advice provided by them over the course of this research helped me in achieving this goal and improving this thesis.

I would also like to thank my lab mates for creating an encouraging and enthusiastic lab environment day in and day out. This research would be incomplete without their helpful discussions, support and encouragement.

Finally, I would like to thank my family back at home for their unconditional and never-ending support and encouragement to pursue my goals.

TABLE OF CONTENTS

1	INTRODUCTION.....	1
1.1	Motivation: Boundary layer effects on miniature shock tube measurements	1
1.2	Uncertainty in state histories in Miniature High Repetition Rate Shock Tube	9
1.3	Background: Synchrotron sources	11
1.4	Motivation for Miniature High Repetition Rate Shock Tube	13
1.5	Motivation for performing Quantitative Density Measurements using X-ray Densitometry	14
2	METHODS AND EXPERIMENTAL.....	17
2.1	Ideal Shock tube theory.....	17
2.2	X-ray densitometry technique	19
2.3	A miniature high repetition rate shock tube.....	21
2.4	Experimental setup for X-ray densitometry experiments at APS	24
2.4.1	Optical access for X-ray densitometry experiments	26
3	COMPUTATIONAL MODELLING.....	29
3.1	Capability of Ensemble Averaged Data.....	29
3.2	Analysis Scheme for processing the experimental data	30
3.2.1	Processing and alignment of Raw Data	31
3.2.2	Calibration of empty and pre-shock data	32
3.2.2.1	Demonstration of calibration method.....	36
3.2.3	Time Resolved Density measurement.....	40
3.2.3.1	Binning of data – Performed in later stages	40
3.2.3.2	Uncertainty analysis using error propagation	41
3.2.4	Time resolved density variation with various transverse x-locations	42
3.2.5	Radially resolved density measurements in miniature HRRST	43
3.2.5.1	Abel Inversion - Onion Peeling Approach.....	43
4	RESULTS AND DISCUSSION	46
4.1	Time varying density measurement at a specific Y location	46
4.1.1	Density variation with time after reflection from end wall at different Y locations	54
4.1.2	Density validation by end wall pressure transducer trace	56
4.1.2.1	Temperature trace evaluation.....	57
4.1.2.2	Boundary layer thickness calculation.....	59
4.2	Estimation of uncertainties in experimental and calculated densities	68
4.3	Time varying density along transverse ‘x’ locations	78

4.4	Radially varying density profiles using abel inversion – Onion Peeling Approach	81
4.4.1	Estimation of boundary layer thickness from radially resolved density profiles	83
4.4.2	Radially resolved density measurement using fitting functions and their distributions.....	87
5	SUMMARY AND CONCLUSIONS	90
6	RECOMMENDATIONS AND FUTURE WORK.....	93
	CITED LITERATURE	94
	APPENDIX.....	100
	NOMENCLATURE.....	109
	VITA	112

LIST OF TABLES

Table 1. List of Synchrotron based experimental techniques associated with their combustion applications	12
Table 2. List of parameters governing the experimental and calculated densities	28
Table 3. Averaged experimental conditions for all scans of experiments	29
Table 4. List of five parameters associated with different scans of experiments.....	34
Table 5. Experimental pressures and temperatures associated with each scan. Upper value = average, lower value = 2σ	46
Table 6. Average values of calculated and measured densities for different y locations, upper value = average density, lower value = uncertainty in density	56
Table 7. Uncertainty in individual parameters for experimental density at different scans of experiments	69
Table 8. Contributions of individual parameters to the final variance of uncertainty in experimental density in pre-shock conditions, Upper value = Contribution value, Lower value = % contribution.....	70
Table 9. Contributions of individual parameters to the final variance of uncertainty in experimental density behind incident shock conditions, Upper value = Contribution value, Lower value = % contribution	71
Table 10. Contributions of individual parameters to the final variance of uncertainty in experimental density behind reflected shock conditions, Upper value = Contribution value, Lower value = % contribution	72
Table 11. Uncertainties in calculated densities for individual and binned experiments for different scans. Upper value- individual, lower value- binned	75
Table 12. Uncertainties in experimental densities for individual and binned experiments for different scans. Upper value- individual, lower value- binned.....	76

LIST OF FIGURES

Figure 1. Mole fraction of TFE and HF varying with radius of the shock tube.....	3
Figure 2. Mole fraction and concentration of HF varying with time from shock reflection.....	4
Figure 3. Comparison of HF absorption for different cases 1) No boundary layer) 2) Boundary layer model -1 3) Boundary layer model -2 4) Adjusted boundary layer model -2 (adjusted T core).....	5
Figure 4. Ignition delay times for n-Heptane for different pressures.....	8
Figure 5. Comparison of end wall pressure traces for 1) Miniature HRRST 2) Brezinsky's HPST (UIC) 3) Brezinsky's LPST (UIC) 4) Ronald Hanson's HPST (Stanford)	10
Figure 6. X-ray diagnostics and its applications in combustion studies	15
Figure 7. (a) Schematic representation of a conventional shock tube (b) Shock tube operation (c) x-t diagram (d) Pressure profile along the length of the shock tube (e) Temperature profile along the length of the shock tube adapted from [6,34].....	17
Figure 8. (a) Schematic of conventional shock tube post reflected shock conditions (b) Pressure profile for post reflected shock conditions (c) Temperature profile for post reflected shock conditions.	19
Figure 9. X-ray transmission through different mediums	21
Figure 10. Picture showing Miniature HRRST situated at UIC.....	22
Figure 11. Side cross sectional view and top view of miniature HRRST in horizontal position [4]	22
Figure 12. X-ray densitometry experimental setup at 7BM-B hutch at APS (ANL).....	25
Figure 13. Schematic of HRRST while conducting X-ray densitometry experiments	26
Figure 14. Schematic representation of different transverse x locations and distances from end wall and the optical section with polycarbonate tube sitting inside	27
Figure 15. Analysis scheme for data processing of X-ray densitometry experiments performed in miniature HRRST	30
Figure 16. Transmitted intensity profiles for a random of 3 experiments for scan 2390 and scan 2391	31
Figure 17. Flattened transmitted intensity for 1710 experiments associated with scans 2390 and 2391	32

Figure 18. Half sectional view of the miniature HRRST viewed along the axis of the shock tube representing varying path length and polycarbonate wall thickness along transverse x-locations	33
Figure 19. Calibration plot for empty data fit to calculated empty model	36
Figure 20. Pre-shock calibration plot w.r.t polycarbonate wall thickness	37
Figure 21. Combination calibration plot for empty, pre-shock data and their corresponding models.....	38
Figure 22. Calibration of pre-shock data involving pre-shock transmissivity and model varying with shock tube path length	39
Figure 23. Chord lengths associated with different annuli along different transverse x locations	45
Figure 24. Incident and transmitted intensities for an individual experiment (Y=-5mm, X=0.03mm) left and binned experiment (Y=-5mm, X=0.03mm) right.....	47
Figure 25. Time varying transmissivity through shock tube for a binned experiment (Y=-5mm, X=0.03mm).....	48
Figure 26. Density associated with an individual and binned experiment (Y=-22mm, X=-0.03mm).....	49
Figure 27. Experimental and calculated density for a binned experiment (Y=-5mm, X=0.03mm)	50
Figure 28. Endwall pressure trace for binned experiment at Y=-5mm, X = 0.03mm.....	50
Figure 29. Temperature distribution across the length of the miniature shock tube (behind reflected shock region).....	51
Figure 30. Temporally resolved density profiles associated with different scans of experiments (Y=-5, -10, -20, -22, -79 mm) with $P_1 \approx 0.2505 \pm 0.01$ bar, $T_1 \approx 27.5 \pm 0.3$ °C and $P_5 \approx 6.58 \pm 0.12$ bar and $T_5 \approx 1452.42 \pm 46$ K	53
Figure 31. Density variation with time along with error bars from shock reflection at different y locations	54
Figure 32. Temperature profile from end wall pressure trace for a binned experiment (Y=-5mm, X=0.03mm) with conditions $P_1 = 0.2445$ bar, $T_1 = 300.7$ K and $P_5 = 6.5$ bar, $T_5 = 1463.49$ K	58
Figure 33. Experimental density and back calculated density for a binned experiment (Y=-5mm, X=0.03mm) with conditions $P_1 = 0.2445$ bar, $T_1 = 300.7$ K and $P_5 = 6.5$ bar, $T_5 = 1463.49$ K	59

Figure 34. Temperature distribution along the line-of-sight (radius through symmetry) tube divided into core gas and boundary layer gas region	60
Figure 35. Comparison of boundary layer temperature profiles at different times $t = 30, 300, 600, 900 \mu s$ using Equation 20 for $y = -5 \text{ mm}$ location	63
Figure 36. Density distribution along the line of sight divided into core gas and boundary layer density region separated by markers	64
Figure 37. (a) Boundary layer thickness as a function time (b) Path length integrated density using the measured boundary layer thickness measured from Lifshitz's temperature profiles	65
Figure 38. Boundary layer thickness calculated as a function of time at $y = -5 \text{ mm}$ using Equations 21 and 22 starting from $t = 0$ to $900 \mu s$	65
Figure 39. Comparison of boundary layer thickness as a function of time obtained from 1) Lifshitz's temperature profiles 2) Experimental density data	67
Figure 40. Uncertainties for calculated and experimental densities represented as error bars for individual experiments ($Y = -5 \text{ mm}$)	73
Figure 41. Uncertainty measurement in calculated and experimental densities for binned experiments ($Y = -5 \text{ mm}$)	74
Figure 42. Uncertainties for individual experiments associated with different scans with different y locations	77
Figure 43. Density variation with time and x locations ranging from -6.25 to $+6.25 \text{ mm}$	79
Figure 44. Time dependent average density variation along various transverse x locations	80
Figure 45. Chord lengths associated with 26 annuli and transverse x locations	82
Figure 46. Time averaged radial density profile at a specific r location	83
Figure 47. Time dependent density variation along various r locations obtained by Abel transform	84
Figure 48. Time varying density variation along the radius of the shock tube obtained by Abel transform- Normalized to density at the center of the shock tube	85
Figure 49. Estimated boundary layer thickness varying with time averaged intervals of $60 \mu s$	86

Figure 50. Profiles for fitting functions and their respective radial distributions of projected data at different times	88
-----------------------------------------------------------------------------------------------------------------------------------	----

LIST OF ABBREVIATIONS

ANL	Argonne National Laboratory
APS	Advanced Photon Source
CVD	Chemical Vapor Deposition
HRRST	High Repetition Rate Shock Tube
PCB	PCB Piezoelectronics, Inc.
PIPECO	Photoion-Photoelectron Coincidence
SAXS	Small Angle X-ray Scattering
TDL	Tunable Diode Laser
TFE	Tri-fluoroethane
TOF-MS	Time of Flight Mass Spectroscopy
UIC	University of Illinois at Chicago
VUV-PIMS	Vacuum Ultraviolet Photoionization Mass Spectroscopy
XAS	X-ray Absorption Spectroscopy
XRF	X-ray Fluorescence

SUMMARY

The presence of non-ideal gas dynamic effects is evident in almost every shock tube conducting various combustion studies. However, as the diameter of the shock tube is decreased these effects tend to get magnified. The major contribution of these effects come from the boundary layer growth behind the incident shock travelling towards the test region. Most of the shock tube studies conducted focus on the region behind the reflected shock as the pressure and temperature conditions in this region reach the practical combustion conditions. However, this boundary layer effect also prevails in this test region affecting the measurement data and hence needs to be investigated.

One of the methods to interpret the boundary layer formation is to conduct density measurements and for which X-ray densitometry technique was used in a miniature high repetition rate shock tube. This type of analysis is only possible because of the unique features of the miniature HRRST. Some of these features include: high repeatability, reproducibility, diaphragm-less operation, and modularity. The X-ray densitometry experiments require X-ray radiation to be passed through the test location and was accomplished by using a synchrotron source at the Advanced Photon Source. Several line-of-sight measurements were conducted across different regions of the optical section of miniature HRRST.

The data obtained from these experiments were analyzed using a custom python code. The analysis performed resulted in time-resolved measurements of density along various measurement locations. The high repeatable and reproducible nature of the shock tube helped in performing the ensemble average of the data both for the experiments associated with each scan and experiments performed at different transverse x locations. A deviation in the density behind the reflected shock was observed which led to the calculation of thermal boundary layer thickness using two different models. This measurement was carried out for all measurement locations and the variation of the boundary layer thickness as a function of time was established. The models used here are based on the assumption that the thermal boundary layer is pre-dominant over the viscous boundary layer considering the high temperature dwell time of the miniature shock tube. However, the model works for the isentropic assumption of temperature profile and when there

SUMMARY (continued)

is a slow growing boundary layer but fails in the continuity as it disregards the mass flow in test region. Having said that, the model presented here is used to estimate the thermal boundary layer thickness as a function of time.

The existence of uncertainty in experimental observation is almost inevitable. For this purpose, a comprehensive uncertainty analysis was performed and the variation in calculated and experimental uncertainties was studied. Density measurements were conducted across various transverse x locations, where the binning of data was performed. The variation in density at different averaged times along various transverse x locations was studied. This served as the stepping stone to evaluate the radially resolved density profiles using Abel Inversion technique. The differences in the boundary layer interpretation by Abel Inversion and the calculated thermal boundary layer are also addressed. A preliminary evaluation of the radial densities with less noise was also conducted.

1 INTRODUCTION

1.1 Motivation: Boundary layer effects on miniature shock tube measurements

Several different types of experiments exist which could use the miniature HRRST technique. The small size of the miniature HRRST leads to concerns about the boundary layer formation in the device. Although this growing boundary layer is evident in almost every shock tube [1–3], it becomes a matter of concern in the case of miniature HRRST due to the presence of relatively large boundary layer thickness when compared to the small bore of the shock tube. It is important to understand the effect of the boundary layer on experiments conducted in the miniature shock tube. One possible effect of growing boundary layers is to affect the temperature and pressure history of the shock tube and cause it to deviate from non-ideal behavior. This will be explored in further detail later. Additionally, growing boundary layers present temperature gradients. These temperature gradients can affect chemical conversions in conditions assumed homogeneous and affect the interpretation of line-of-sight measurements [4].

The optical measurements conducted in shock tubes are line-of-sight averaged measurements. When traversing an optical path that contains cold sidewall boundary layers, these regions can be observed and affect the interpretation of path length integrated measurements. For instance, as most reaction rates are strongly temperature dependent, the gases in cold sidewall boundary layers would have less chemical conversion from reactants to products. A path averaged measurement could misinterpret chemical conversion at an assumed core temperature low because of less conversion in the boundary layer. This is not the only effect though. Path averaged measurements like emission and absorption might preferentially measure the concentration in the cold boundary conditions. In absorption measurements this is possible because the absorption coefficient is inversely temperature dependent. [1] In emission experiments, like ignition delays measured by chemiluminescence, reabsorption in the boundary layer is problematic. Additionally, should ignition happen first in the colder boundary layer regions (possible if the conditions are those of the negative temperature coefficient region) this would change the interpretation of ignition delay measurements.

Three of these scenarios are tested below to show the impact of thick boundary layers on shock tube measurements:

i. Chemical conversion: Reactive cases

The first scenario is based on the effect of growing boundary layer on the chemical conversion rates of reactive species. As mentioned earlier, the boundary layer effect on the conversion of reactants into products would lead to inaccuracies in estimating reaction rates and rate constants. This is because the path averaged measurements made using the miniature HRRST would account the low temperature region of growing boundary layer where there is no chemical conversion. Therefore, to address this issue a previous study on chemical thermometry [4] using the miniature shock tube was chosen where 1,1,1 – trifluoroethane dissociates into HF and difluoroethylene (1,1-C₂H₂F₂). The analysis presented here is based on estimation of chemical conversion rates in different situations such as homogeneous temperature distribution (no boundary layer) and the situation where there is a growing thermal boundary layer. The unimolecular dissociation of TFE (1,1,1-C₂H₃F₃) into difluoroethylene (1,1-C₂H₂F₂) and HF is given by



With $k_\infty = A * e^{\left(\frac{-E_a}{R*T}\right)}$ where $A = 3.33\text{e}^{14}$, $E_a = 74.24 \text{ kcal/mol}$, $R = 8.314 \text{ J/mol-K}$ and T is temperature in K.

Most of the chemical kinetic studies have considered the chemical conversion of the reactants into products to be consistent throughout the section of the shock tube due to the large bore factor where there is negligible boundary layer growth in comparison to the diameter of shock tube. However, several other studies [3] have been performed where the issue of presence of unreactive gas causes irregularities in the measurement of rate constants and concentrations. However, the effect of boundary layer formation on the chemical conversion can be interpreted by analyzing the conversion of TFE into HF using the assumed boundary layer models.

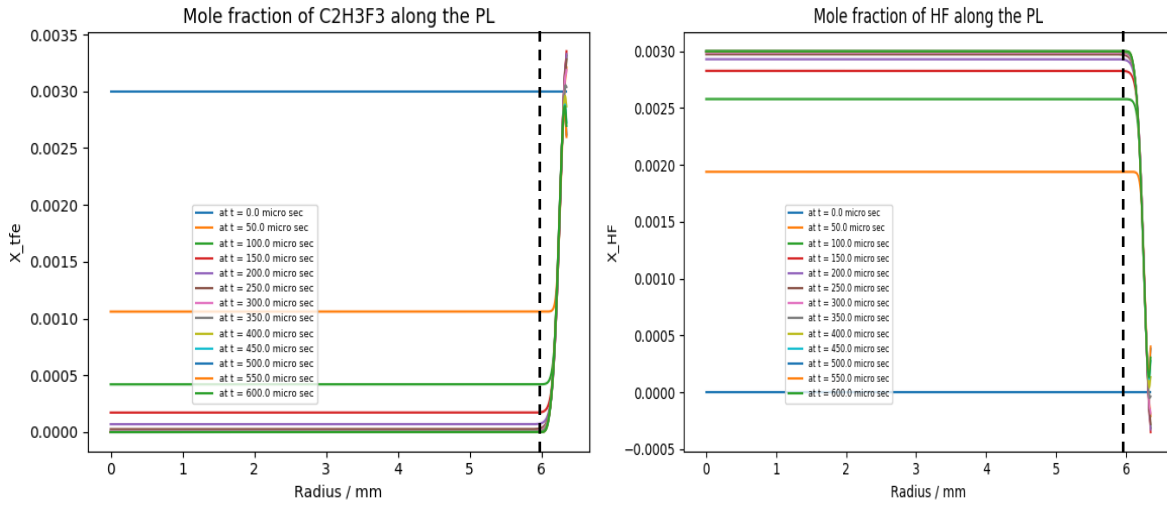


Figure 1. Mole fraction of TFE and HF varying with radius of the shock tube

The rate at which the TFE converts into the HF is governed by the rate equation which accounts for the change in rate of change of concentration of TFE and rate of change of total molar concentration. Mole fractions of TFE and HF as a function of radius of miniature shock tube assuming a cold side wall boundary layer growth are shown in Figure 1. It is evident that the mole fraction of HF along the path length of the shock tube decreases as the side wall is approached meaning the cold gas temperature region has a little amount of HF being formed. In addition to this, Figure 1 also shows that the C2H3F3 reacts in the high temperature core gas region but is unreactive in the cold boundary layer region suggesting a low rate of conversion into HF in this region.

Accompanying the above plot, the chemical conversion rates of TFE into HF for different conditions have been estimated by using four different models. The original or the simulation generated model estimates the concentrations and reaction rates based on homogeneous temperature assumption. However, the non-ideal case of boundary layer growth along the side wall of the miniature shock tube has been accounted by the boundary layer model -1 and 2 by assuming a temperature profile which includes cold side wall temperature and hot core gas temperature.

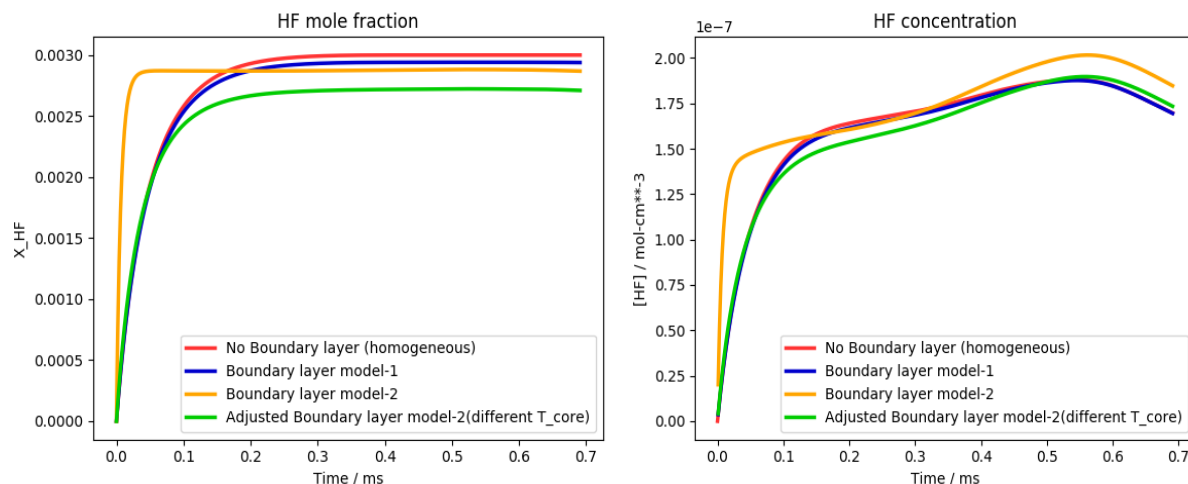


Figure 2. Mole fraction and concentration of HF varying with time from shock reflection

A comparison plot for the mole fraction and concentration of HF as a function of time from the shock reflection is shown in Figure 2 where the mole fraction of HF increases initially and remains constant in all the cases. The mole fraction estimated by no boundary layer model and boundary layer model -1 are close to each other as this model accounts for a slower growing boundary layer. However, there is a significant difference between the no boundary layer and boundary layer model -2 case as the mole fraction and concentration of HF rise immediately accounting for a faster boundary layer growth. Hence, an evident deviation in chemical conversion rates of TFE and HF suggests that the problem of thicker and faster boundary layer growth would affect the path length averaged measurements which are dependent on the reaction rates.

ii. HF Absorption – Dissociation of 1,1,1 – Trifluoroethane

The second scenario is of the optical measurements such as absorption measurements which generally require the absorption cross-section coefficient (σ) value which is a function of concentration of absorbing species and temperature. Normally, absorption measurements in shock tubes assume a homogenous path length through the shock tube. However, this would not be the case if there were a significant boundary layer formation present in the miniature shock tube and in specific behind the reflected shock wave. Therefore, a different temperature profile instead of homogeneous temperature would lead to

different path length averaged concentrations inciting competing effects on sigma value and hence the absorption. For instance, in a system like 1,1,1-trifluoroethane, the production of HF (which is detectable by laser absorption [4]) is mostly produced by the unimolecular dissociation of TFE ($C_2H_3F_3$) into difluoroethylene ($C_2H_2F_2$) and HF as described previously in chemical conversion scenario.

Using this reactive mechanism, the known pressure state in the miniature shock tube, and data about the temperature and pressure dependences of the absorption coefficient of HF, the absorption can be simulated along an assumed homogeneous shock tube bore (Fig 3). The presence of cold boundary layers would change the apparent absorption and are evaluated using the previously described boundary layer models 1 and 2.

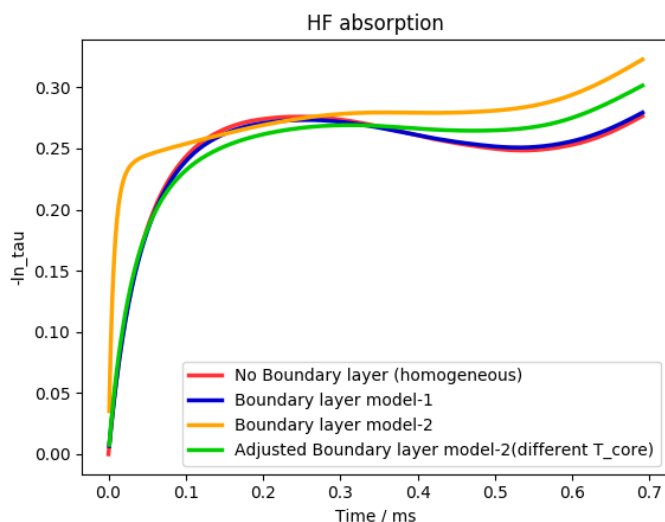


Figure 3. Comparison of HF absorption for different cases 1) No boundary layer) 2) Boundary layer model -1 3) Boundary layer model -2 4) Adjusted boundary layer model -2 (adjusted T core)

It is evident that the absorption in the case of boundary layer model -1 is close to the original absorption (no boundary layer model) suggesting this model is not sensitive to the boundary layer formation in the miniature shock tube i.e. presence of a slower growing boundary layer. However, there is evident disagreement (immediate rise in absorption) between the no boundary layer model and boundary layer

model -2 absorption which is due to a faster growing boundary layer along the side wall of miniature shock tube. This deviation also can be related to the previously discussed unreactive HF being present in the fast-growing cold boundary layer region is absorbing more than the ones in hot core gas region and leading to an immediate increase in the absorption. However, a lower temperature ($\sim 110\text{K}$ lower than original temperature) results in the absorption of boundary layer model -2 to agree with the simulated absorption suggesting that a breakdown of the different absorption related profiles is required if a faster growing boundary layer formation is present. The reasons for the disagreement between the simulated (no boundary layer) and boundary layer model -2 can be put forth by three arguments.

The first argument is based on the previously described chemical conversion rates of TFE into HF where the small amount of HF due to unreactive TFE in the boundary layer region in fact has greater absorption than the ones in the hot core gas region. The second possible reason for this deviation is that, the boundary layer growth behind the reflected shock wave is not actually as fast as the model would predict, a slower boundary layer growth would eventually minimize the effect on absorption or the chemical conversion within the reaction time of the miniature shock tube.

The third reason for the deviation using this boundary layer model is that, the model used here might not be an accurate method for estimating the boundary layer growth along the side wall of the miniature shock tube. This is because the boundary layer growth is not only affected by the heat transfer phenomena but also by mass transfer such as the bulk flow towards the end wall during the evacuation of gas after each experiment. However, the model used here to predict the boundary layer effect on these measurements could form one of the bounds of some other model which would account for all the extra factors thereby helping in formulation of an updated model which would lie somewhere between the bounds of the heat transfer and mass transfer.

iii. Ignition delay measurements:

The miniature shock tube has been used to conduct robust ignition delay measurements from time to time where the ignition delay time has been chosen to be the time at which the temperature gradient is

maximum or by using the chemiluminescence traces such as the formation of OH radical which has proven to be a good ignition delay indicator [5]. End wall pressure traces have also been used to estimate the ignition delay time but are accompanied with certain effects. These effects which contribute to the pressure change include the rise in pressure as the reflected shock wave propagates back into the incident shock region due to the growing side wall boundary layer, interaction of contact surface and rarefaction with the reflected shock wave and change in temperature and density leading to the change in pressure. However, the prime focus here is to evaluate the growing boundary layer effect on the ignition delay measurement which happens to be a dominating factor in causing the non-ideal behavior of the gas states behind the reflected shock. Therefore, a simple case of measuring the ignition delay times of n-Heptane is considered here to interpret the effect of cold temperature boundary layer along the side walls of the miniature shock tube.

The criteria for selecting n-Heptane was the presence of NTC region where the ignition delay time increases as the temperature is increased, which happens to serve the purpose of interpreting the boundary layer effect since there would be pre-ignition in this region if below the reaction time which is less than 1ms. The operating conditions of the miniature shock tube where it can reach $T > 600\text{K}$ and $P < 100$ bars have been considered here to evaluate how the NTC region would behave if the pressures were to be changed. A comparison plot for the ignition delay times is shown in Figure 4 for n-Heptane at various pressures ranging from 10 atm to 100 atm using the LLNL mechanism (Lawrence Livermore).

The ignition delay time decreases in all the cases as the temperature is increased above 1000K with the highest value associated with the lowest pressure of 10 atm and least for the highest pressure 100 atm. However, there is an increase in ignition delay time from roughly from $\sim 700\text{K}$ to 1000K where the NTC region prevails suggesting that at lower temperatures there would be pre-ignition occurring if this time were below the reaction time of the miniature shock tube (1ms)

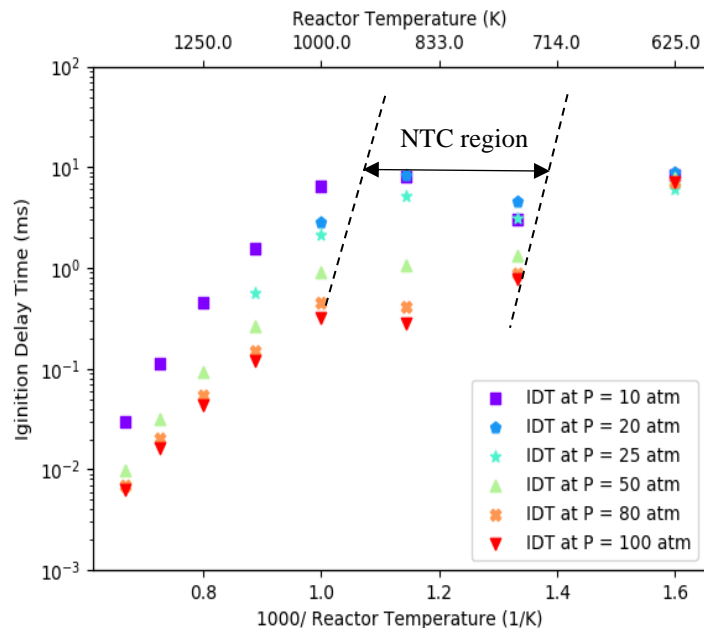


Figure 4. Ignition delay times for *n*-Heptane for different pressures

Pressure conditions ($P < 50\text{atm}$) have this NTC region way above the region of 1ms meaning this would not be a concern in the miniature shock tube ignition delay study. However, as the pressure increases above 50 atm, this poses a concern where the NTC region has the ignition delay time below the reaction time zone of 1ms. In this case, there might be a possibility of pre-ignition chemistry which would lead to inaccurate estimation of ignition delay times. Since, this anomaly happens to be at lower temperatures, the cold boundary layer region would be a suitable region to feed this pre-ignition. Although these pressures are very high when compared to the previous studies conducted using the miniature shock tube ($P < 20\text{ bar}$), the analysis put forth is to be treated as a mere possibility if there was a cold region of boundary layer growth present which might cause hindrance in IDT measurements at these high-pressure conditions.

Therefore, a brief insight on how the boundary layer growth inside the miniature shock tube would affect the various measurements and the need to develop a boundary layer model to achieve accurate results, provided the motivation to carry out further analysis of the cold boundary layer growth by interpreting other data such as density measurements. The uncertainty in the previous miniature HRRST measurements are highlighted here which leads to the question of uncertainty in the gas state histories in miniature HRRST.

1.2 Uncertainty in state histories in Miniature High Repetition Rate Shock Tube

The use of miniature HRRST has its merits but also has some uncertainty in conditions behind the shock front which become significant in small-bore shock tubes. However, a general approach to evaluate the state histories in most of the shock tube studies, such as the temperature and pressure conditions behind the incident and reflected shock, is to use the ideal normal shock equations [6] assuming that the conditions do not vary with time. However, due to the non-ideal nature in every device, including the miniature HRRST, constant conditions with respect to time are not observed. This is because of non-ideal gas dynamic effects [1] and the growing boundary layer [2,3,7] as the incident shock propagates. These non-ideal effects have a larger impact on the state histories in small-bore shock tubes [3] such as the miniature HRRST used in this study. On the other hand, these effects tend to produce results deviating from those calculated by using the ideal normal shock equations and are not constant with respect to time. Thus, it becomes important to investigate these non-ideal effects, specifically the boundary layer formation which has a greater influence on the reaction conditions behind the reflected shock in the small-bore shock tube.

One of the preliminary methods to observe the magnified effect of non-ideal gas dynamic effects in the miniature shock tube is by comparing the end wall pressure traces of different shock tubes. These pressure traces are obtained for almost every existing shock tube and are recorded for every experiment performed. Most of the shock tube pressure traces show a non-linear pressure profile after the shock reflection. However, the aspect of interest by observing the pressure traces is, how large is the deviation in pressure profile of different shock tubes from the assumed constant pressure and temperature conditions by using ideal normal shock equations. Therefore, to serve the purpose of observing the deviation in pressure profiles behind the reflected shock conditions, four different shock tubes were considered. The end-wall pressure trace for different shock tubes i.e. the miniature HRRST with a bore of 12.7 mm, Brezinsky's high pressure and low pressure shock tube at UIC with a bore of 25.4mm and an area ratio of 1.6 respectively and one of Ronald Hanson's shock tubes at Stanford with a bore of 141.2 mm[8] which have varying bores all larger than the miniature HRRST is shown in Figure 5.

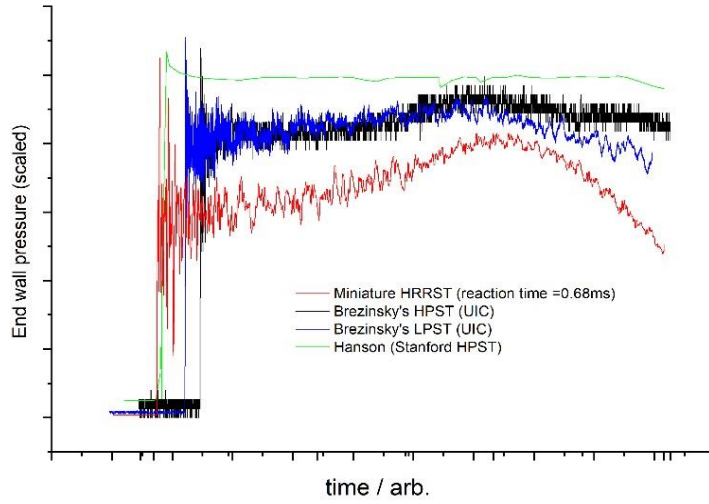


Figure 5. Comparison of end wall pressure traces for 1) Miniature HRRST 2) Brezinsky's HPST (UIC) 3) Brezinsky's LPST (UIC) 4) Ronald Hanson's HPST (Stanford)

It is evident from the Figure 5 that the end-wall pressure trace i.e. the pressure behind the reflected shock is relatively flat in the HPST (UIC), LPST (UIC) and the Stanford shock tube compared to the end wall pressure trace for the miniature shock tube. The pressure profile is flattest in the Stanford shock tube with almost constant pressure after the shock reflection. The pressure traces for HPST (UIC) and LPST (UIC) have a relatively small non-linear (bump) profile. It is important to note that, as the shock tube bore is decreased from 141.2mm to 25.4mm, the pressure profile has a significant bump which is due to the non-ideal effects. However, comparing the pressure trace of miniature HRRST to the rest of the pressure traces, it becomes evident the rise (bump) in the pressure profile is magnified in case of the miniature HRRST. This deviation is because of the small bore of miniature HRRST where the non-ideal effects are playing a magnified role in increasing the pressure and temperature conditions behind the reflected shock. Thus, the large bore shock tubes have less significant impact on the reaction conditions from the non-ideal gas dynamic effects and is least important in them. However, most of these shock tubes improve their reaction conditions by incorporating several modifications such as placing a driver section insert and tailoring of the driver and driven gas etc. It is this difference in state histories which is of interest in this study due to the boundary layer growth in non-reactive cases and is accomplished by conducting density measurements.

1.3 Background: Synchrotron sources

A significant increase in the use of synchrotron-based sources to conduct combustion studies have involved several combustion devices. These devices include flow reactors, jet stirred reactors and premixed flames etc. The techniques implemented range from vacuum ultraviolet photoionization mass spectroscopy (VUV-PIMS) to small and wide-angle X-ray scattering (SAXS and WAXS). The advantages in using synchrotron sourced radiation includes: a) relative ease in obtaining discrete photon energies, b) high brilliance, and c) safe operation and many more. Taking advantage of these features, several important studies which include studying kinetics and isomerization of gas phase and neutral chemical reactions [9] and flame chemistry [10–12] were accomplished by using VUV-PIMS technique. In addition to this, X-ray absorption spectroscopy (XAS) technique helped in probing species in pre-mixed flames [13]. The efficient use of emission characteristic of an element when exposed to intense X-ray radiation is accomplished by using the X-ray fluorescence (XRF) technique. Some of the studies conducted by using this technique include investigating distorted temperature fields of sampling probes in pre-mixed flame experiments [14].

The features such as safety and provision of high flux helped in conducting studies which involve measuring the scattered intensity of X-ray radiation through a sample by using small-angle X-ray scattering (SAXS) technique. The combined application of high speed imaging and X-ray radiation has helped researchers to conduct various combustion studies. Some of these include studying the fuel distribution from the orifice of an injector [15] and conducting a detailed analysis on the geometry effects present in the nozzles during the fuel injection by using the X-ray radiography and tomography technique. However, these applications of synchrotron-based experiments are not limited only to the combustion regime but are also spread over diverse research areas such as materials research, cell biology, lithography etc.

Some of the major combustion studies using synchrotron sourced X-ray radiation have been highlighted here. However, these studies fall short in the regime where high pressures and temperatures are involved. Therefore, the use of a combustion probing device such as a shock tube is capable of approaching the high temperatures and pressures similar to practical combustion chambers. The shock tube can be used

to conduct gas kinetic studies to measure the reaction rates, test times and species. On the other hand, several optical techniques such as laser schlieren, interferometry and X-ray absorption have also been used to conduct various optical measurements. The advantages associated with synchrotron based experimental techniques include: the ability to obtain a continuous spectrum, high flux, and high coherence. One of the previous synchrotron based studies conducted in shock tube involve the use of VUV-PIMS technique to study the pyrolysis of dimethyl ether (DME) [16].

Table 1. List of Synchrotron based experimental techniques associated with their combustion applications

Application ↓	Experimental Technique →						
	Spectroscopy				Scattering		Imaging
	VUV-PIMS	XAS	XRF	PIPECO	SAXS	WAXS	X-ray Radiography and Tomography
Flow tube reactor	D.L. Osborn et al. [9]	Jan-Dierk Grunwaldt et al. [17]		Gustavo A. Garcia et al. [18]			
Stirred reactor	F. Battin-Leclerc et al. [19]						
Flames (premixed & diffusion)	C.A. Taatjes et al. [10] Yuyang Li and Fei Qi [11] F.-X. Ouf et al. [12]	Jonathan H. Frank et al. [13]	N. Hansen, Alan L. Kastengren et al. [14]	D. Felsmann, Kai Moshamer, J. Kruger et al. [20]	P.M. De Lurgio et al. [21] J.B.A. Mitchell et al. [22]	L. Vallengaag et al. [23]	Leslie G. Butler et al. [24]
Sprays			Christopher D. Radke et al. [25]				D.J. Duke et al. [26] Mark A. Linne et al. [27] Alan L. Kastengren et al. [15]
Aerosols	Tomas Baer et al. [28]					Artur Braun [29]	

There are many combustion studies involving synchrotron-based sources including the shock tube as a combustion device. Some of the studies along with their applications apart from shock tube related have been tabulated in the Table 1.

1.4 Motivation for Miniature High Repetition Rate Shock Tube

The goal to achieve the pressures and temperatures similar to practical combustion engines requires high operating pressures which are not typical of most previous studies using synchrotron sources. Those systems had reactors with low operating pressures, typically atmospheric pressure or lower. Hence, the shock tube is considered as a logical choice which would provide high pressure operating conditions with ease. Several high temperature studies have been conducted using the shock tube which cover a wide range of temperature (450-8000 K) and pressure ($7 \times 10^{-3} - 1000$ bars) [30]. However, the integration of shock tube with synchrotron sourced techniques brings some design challenges. Some of those important challenges that need to be addressed are 1) space constraint- limited amount of space is available at the synchrotron facility to carry out the desired experiments 2) the Setup must be automated where thousands of experiments are needed to obtain a dataset. 3) high repeatability rate i.e. experiments should be repeatable over several shots to obtain a strong S/N ratio obtained by signal averaging. 4) a high cycle rate is desired to make an effective use of beam time, as mentioned in previous works [30].

The design and operation of a traditional shock tube does not tackle the mentioned challenges because they are generally large devices with long lengths and large bores depending on the experimental technique, observation time, etc. The cycle rate of these shock tubes is low, i.e. one shot over a period of 15-20 minutes to several hours, due to the changing of diaphragm after every shot and evacuating the gases in the driven section. It is difficult to perform signal averaging with a conventional shock tube since the opening of the diaphragm is slightly different each time, and the experiment is not generally repeatable shot-to-shot.

Therefore, to have the shock tube work with a synchrotron source technique, the shock tube must be highly repeatable, modular, and compact. As a result a high repetition rate miniature shock tube (HRRST) had been designed and constructed similar to the one mentioned in [30] which accounted for the mentioned

challenges effectively. The complete details on construction and operation of the miniature HRRST can be found in [4,30] and the important operational and design specifics are only mentioned here briefly in the later sections.

1.5 Motivation for performing Quantitative Density Measurements using X-ray Densitometry

The main goal of this study was to measure the boundary layer formation in the miniature high repetition rate shock tube. One way to achieve this is to measure the temperature change with respect to time behind the reflected shock region or measure the chemical conversion [3] in the test region. However, due to the absence of temperature measurement and no chemical conversion, evaluating density behind the reflected shock region was employed. Therefore, the density measurement and characterization of gas state histories in the miniature shock tube was accomplished by using the X-ray densitometry technique. The implementation of X-ray densitometry technique led to interesting observations of uncertainty or deviation in gas states due to the boundary layer growth.

The density measurements conducted by using the X-ray densitometry technique involve passing the X-ray radiation through the sample from a well-equipped source such as a synchrotron source. It is however, important to appreciate how diverse and useful the X-ray diagnostics has been to combustion researchers in studying combustion phenomena such as in premixed flames, micro flow tube reactors, gas turbines and sprays etc. as mentioned earlier. A combination of the X-ray radiation and synchrotron facilities has led to studying different combustion phenomena using different techniques available to the experimentalist. The diverse spread of the X-ray diagnostics in the combustion field can be shown in the Figure 6 with the applications attached to it. The various applications where X-ray diagnostics has provided useful insights range from flame studies to shock tube studies. The related works using these applications can be referred to Table 1.

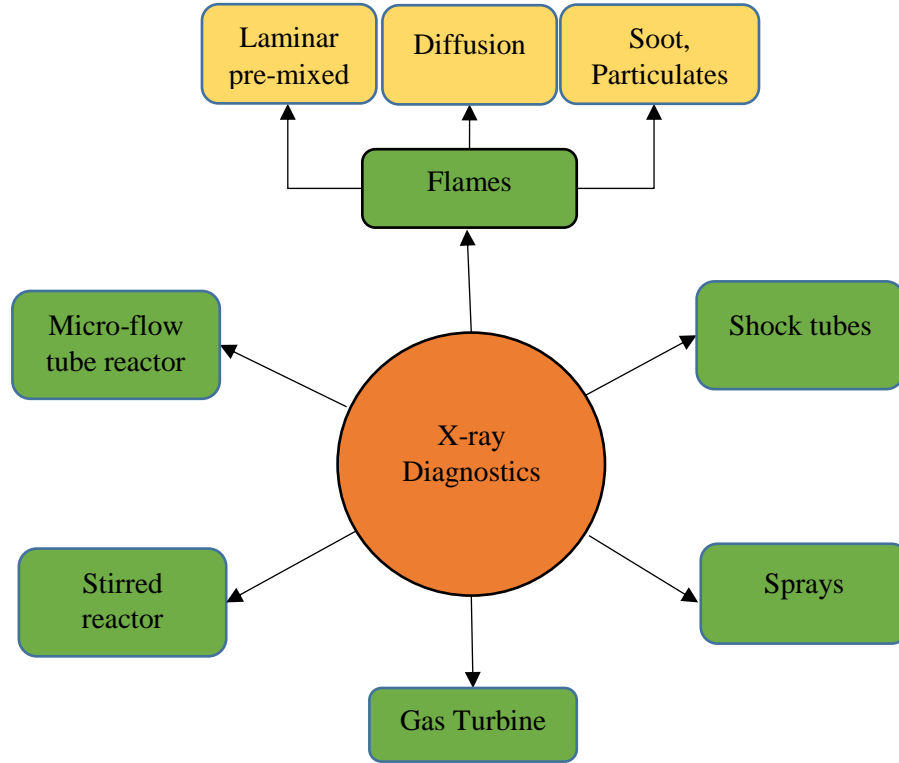


Figure 6. X-ray diagnostics and its applications in combustion studies

However, handling of X-ray generation, transmission and shielding is very crucial as X-Rays are harmful. This problem of handling the X-ray radiation was eliminated by coupling the miniature HRRST with the synchrotron X-ray radiation source which helped in achieving the desired measurements of density. Synchrotron facilities like Advanced Photon Source provide the right band of energies for density measurements of inert gases like Ar. The X-ray densitometry experiments were performed at one of the beamlines at APS, the 7-BM beamline, [31] having various advantages to it ranging from control to shielding. Although, there are various other density measurement techniques such as interferometry [32] and laser schlieren technique [33] which use the principle of measuring the density gradient using the deflection of laser beam when sent across the test section, X-ray densitometry technique was preferred

over these techniques was because of two reasons. 1) it is a direct measurement of density 2) X-ray densitometry has the advantage over laser schlieren in high pressure conditions where there is turbulent beam steering because X-ray radiation is insensitive to the refraction with the refractive index being close to 1.

As previously mentioned, the magnified impact of the non-ideal effects and in specific, the boundary layer effect in the small-bore shock tubes needs attention. Therefore, the quantitative density measurements across different sections of the shock tube helped in characterizing the density variation of the test gas with time and location. This finally led to a more important measurement of density variation along the radius of the shock tube. This interpretation helped in measuring the boundary layer growth along the side wall of the miniature shock tube which was obtained by performing a tomographic reconstruction of an assumed radially symmetric profile from various lines-of-sight measurement. This type of analysis is only possible because of the high reproducibility and repeatability nature of the miniature shock tube with high throughput rates which makes this analysis feasible and making it possible in providing the basis to develop a model which accounts for the deviations in measurements due to the presence of boundary layer growth. Different interpretations of radially varying density are reported which helped in having a deeper insight on the boundary layer formation in the miniature high repetition rate shock tube. The data obtained from performing X-ray densitometry experiments involves the reactive (acetone) and non-reactive (argon) case. However, the study presented here focuses on the non-reactive case with the test gas as argon.

2 METHODS AND EXPERIMENTAL

2.1 Ideal Shock tube theory

The shock tube is an important combustion device for probing combustion phenomena in different experimental conditions. A traditional shock tube consists of a tube with a diaphragm separating a high pressure and low-pressure gas. The bursting of the diaphragm creates a normal shock wave propagating through the low pressure or test gas region raising the pressure and temperature of the gas behind the shock and accelerating it towards the endwall. This normal shock wave travelling towards the end wall is called the incident shock wave. The incident shock wave reflects off the endwall stagnating the test gas, and further increases the pressure and temperature. The shock propagation along the length of the shock tube starting from the bursting of diaphragm is shown in Figure 7. For the standard operation and design of shock tubes can be seen in [6,34] for further information.

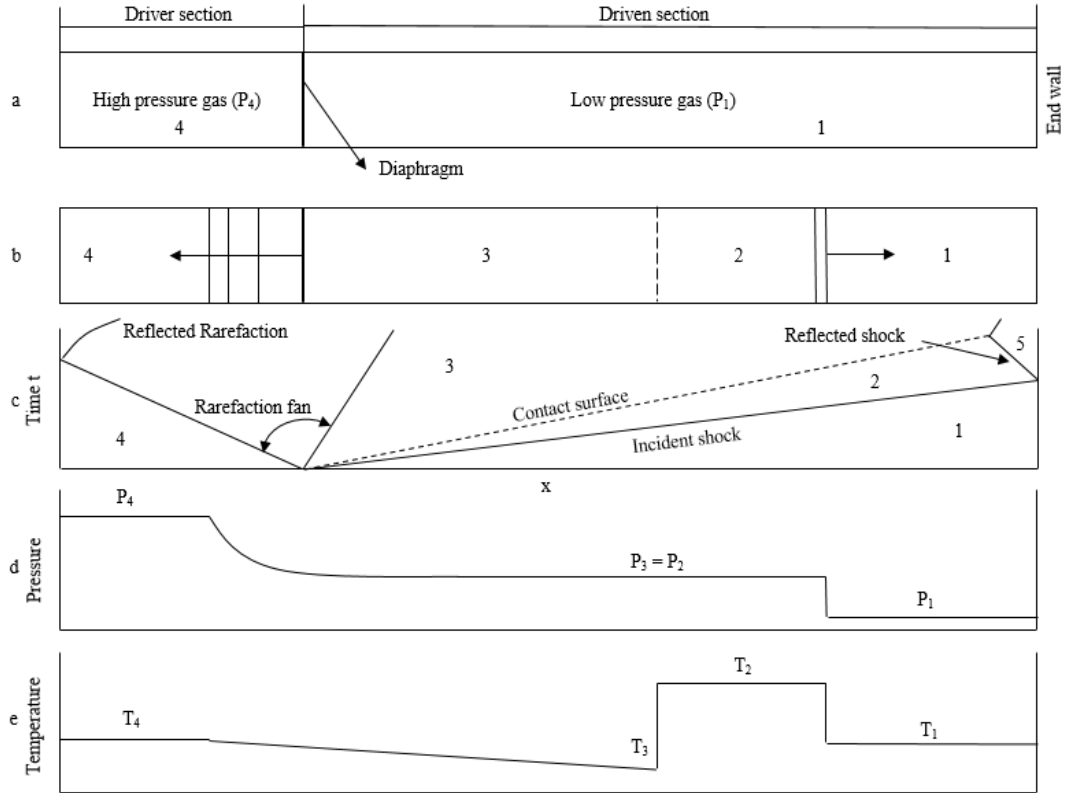


Figure 7. (a) Schematic representation of a conventional shock tube (b) Shock tube operation (c) $x-t$ diagram (d) Pressure profile along the length of the shock tube (e) Temperature profile along the length of the shock tube adapted from [6,34]

The driver gas is usually a very low molecular weight gas like He and the driven gas is a test gas which is a mixture of fuel to be tested and inert gas in case of chemical kinetic studies. In the current study, the driver and the driven gas are both inert. Figure 7(a) represents a conventional shock tube with a diaphragm separating the driver and driven sections. The Figure 7(b) shows the shock tube configuration when the diaphragm is ruptured creating the incident shock wave travelling towards the driven section end wall and an expansion fan travelling towards driver end wall.

A convenient way to interpret the unsteady motion of shock wave propagation is by constructing a wave diagram essentially an x-t plot as shown in Figure 7(c). Initially, the incident shock is at the diaphragm location at $t=0$. After a time t , the incident shock is propagating towards right before hitting the endwall. This incident shock upon hitting the endwall bounces back to the left as a reflected shock wave. To the left of x-t plot, the rarefaction fan moving towards left reflects towards right as a reflected rarefaction wave upon hitting the driver end wall. The zone and the subscript 1 and 4 denote the initial driven and driver conditions respectively whereas the zone and subscript 3 and 2 denote the region behind the contact wave and behind the incident shock region respectively. The pressure and temperature profiles varying along the length of the shock tube are shown in Figure 7(d) and Figure 7(e). The standard notations for temperatures and pressures is used as T and P.

The region behind the reflected shock as shown in Figure 8 is represented by the subscript 5. This region has the highest temperature and pressure conditions during shock tube experiments and has the conditions of most interest for the chemical kinetic studies using optical diagnostics. The Figure 8(a) shows the reflected shock propagating back towards the driver section. The contact wave which was far away from the driven section endwall has moved closer. The left section of the figure shows the reflected rarefaction fan moving towards right and eventually reaching the test location. The pressure and temperature profiles for the respective regions are shown in Figure 8(b) and 8(c). It is evident from these figures that the pressure and temperature are the highest in the region behind the reflected shock making it the prime region to be

studied in the shock tube. The gas state histories are obtained by using ideal normal shock relations assuming no change in quantities with respect to time.

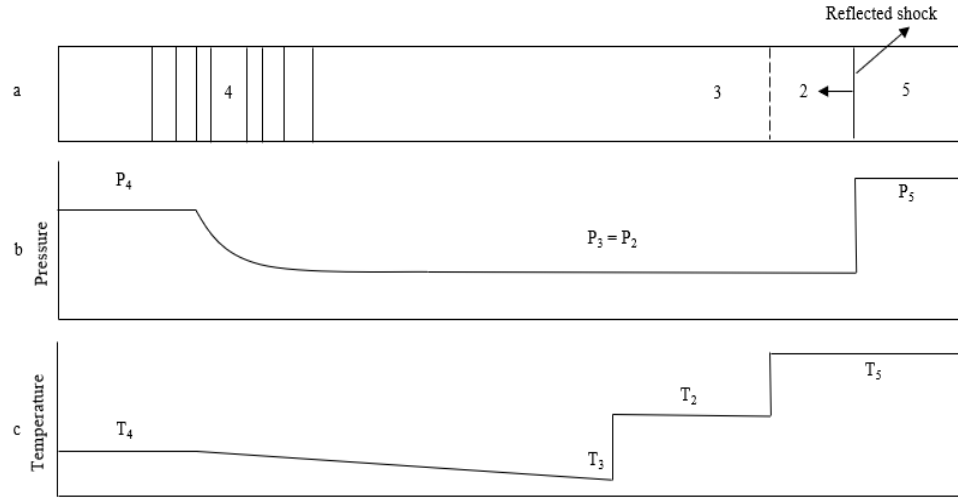


Figure 8. (a) Schematic of conventional shock tube post reflected shock conditions (b) Pressure profile for post reflected shock conditions (c) Temperature profile for post reflected shock conditions.

2.2 X-ray densitometry technique

One of the interesting (direct measurement of density) optical diagnostic techniques in combustion studies is X-ray absorption densitometry technique. This technique has been in use for 80 years in the combustion field with increasing sophistication. The basic principle in the X-ray densitometry technique is to capture the amount of X-ray absorption in the test zone and relate this to conditions in the combustion device. For instance, density changes could be related to rates of reaction, etc. The earlier techniques [35] used a X-ray densitometer operating under the desired conditions. The X-ray pulse of a specific energy was passed through slits reaching the test sample with limitation on the provision for different X-ray energies. The incident and transmitted X-rays were recorded through a photomultiplier combination which sends the signal to the oscilloscope. These signals were photographed and analyzed to obtain the density measurement from x-ray transmission.

The X-ray densitometry technique used in this study follows a similar procedure where the X-ray of specific energy required to study the test sample is passed through the test zone of the miniature shock tube through a repositionable window section along with a polycarbonate tube window. The incident and transmitted intensities signals are recorded and sent to an oscilloscope to collect the respective data. The difference in the technique used in [35] and this study is the control and handling of the X-ray energies with increased safety measures due to the use of synchrotron sourced X-ray radiation. The integration of the miniature shock tube and synchrotron sourced X-ray radiation also permitted the precise movement of the optical section to carry out various line-of-sight measurements along different sections.

The procedure to relate the density of the test gas to the recorded intensities in these studies is based on the fact that, the transmission of X-rays through a medium is directly proportional to the density of the medium, path length through the medium and the absorption coefficient and is a direct consequence of Beer's law. A general representation of the formula for Beer's law is given by Equation 1,

$$\tau = e^{-(\rho * PL * \sigma)} \quad (1)$$

where, τ is the transmissivity through the shock tube, ρ is the density of the test gas, PL is the path length and σ is the absorption coefficient of the test gas.

The transmission of X-rays through different mediums is shown in Figure 9. The transmission of X-rays through the 2mm thick polycarbonate window section is 5.7% more at 9keV energy compared to the 1mm thick CVD diamond window section [30]. The path length through the shock tube in the case of polycarbonate window was about 12.7mm and for the CVD diamond window was 6.6mm which was essentially due to the large and small bore of the shock tube. The transmission through the test gas (Ar) is also plotted for different pressures and temperatures of $P = 190$ torr, $T = 300$ K and $P = 1345$ torr, $T = 809$ K varying with different photon energies [36]. These conditions are similar to the conditions of pre-shock and behind the incident shock respectively and the variation in transmission through Ar gas in pre-shock conditions is 6.7% more than the case of incident shock condition at 9keV. The increase in photon energy tends to increase the transmission through both the polycarbonate and CVD diamond window with the

penalty of weaker absorption in the test gas. The transmission through the polycarbonate window affected the window material for which it was periodically replaced.

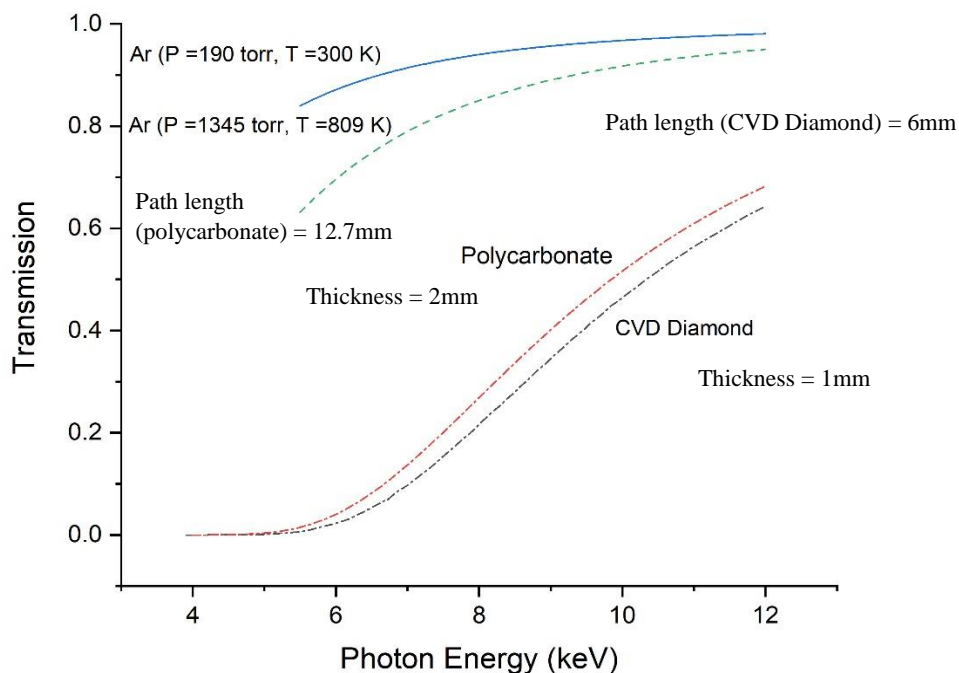


Figure 9. X-ray transmission through different mediums

However, the complexity is encountered while performing the calibration in this study as the path length is a combination of the path length through the test gas as well as the polycarbonate wall thickness which changes with each section of the shock tube as it is a curved window.

2.3 A miniature high repetition rate shock tube

A miniature high repetition rate shock tube with the capability of achieving reaction conditions of pressures ($P < 100$ bar) and temperatures ($T > 600$ K) has been designed and constructed to be used both at the synchrotron facilities and in laboratory. This shock tube is a second version of the miniature shock tube with a larger bore (twice) as compared to the shock tube at ANL [30]. Currently the miniature HRRST is situated at UIC and is shown in Figure 10.

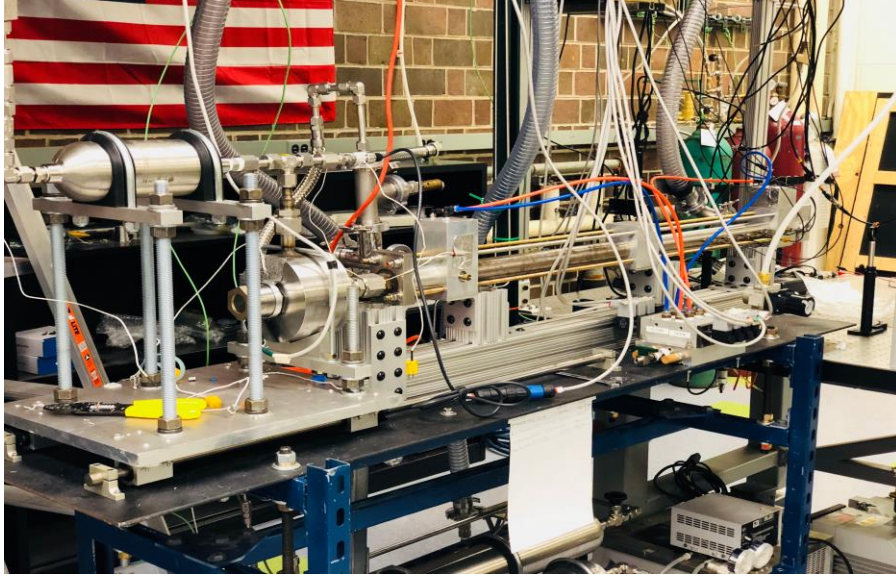


Figure 10. Picture showing Miniature HRRST situated at UIC

The shock tube used here is similar in construction and operation to the one described in [30] with the notable differences with a bore of 12.7mm and a driven section of approximately 1.495m. Only a brief amount of information on the construction of the miniature shock tube is discussed here with the focus on important specifics and its operation. A schematic representation of the miniature shock tube placed horizontally as shown in Fig 11 showing the side and top view.

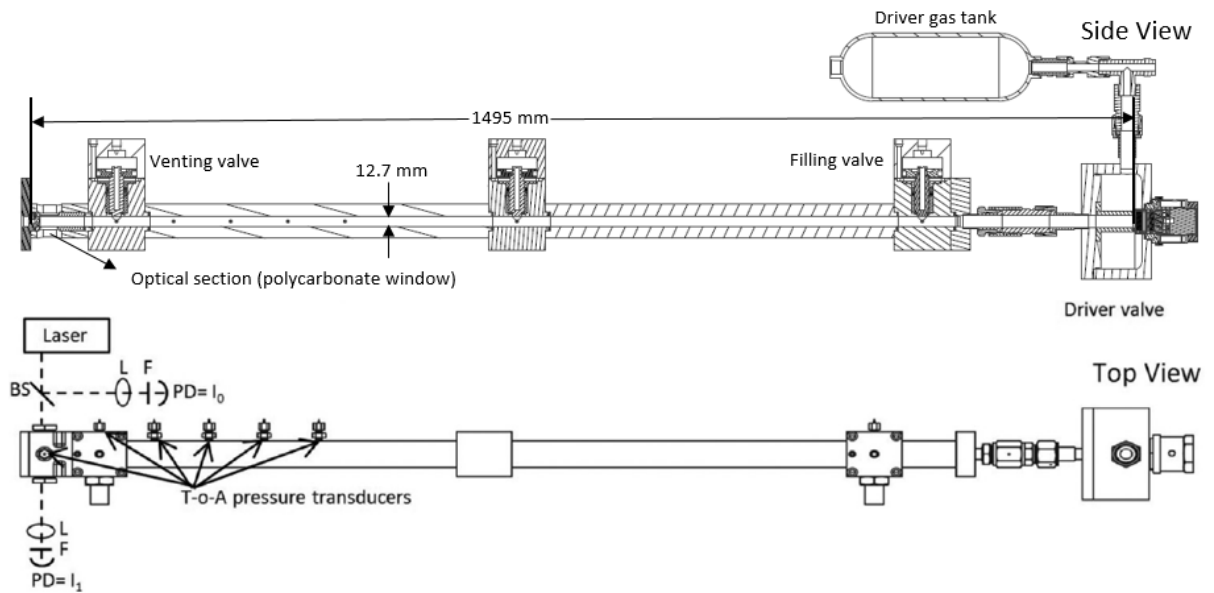


Figure 11. Side cross sectional view and top view of miniature HRRST in horizontal position [4]

The miniature shock tube consists of a driver and driven section separated by a fast-acting solenoid-driven high pressure, spring-return valve [37] . The new improved design of the valve accounts for a better sealing mechanism and better throughput rates resulting in better performance when compared to the one used in [30]. As mentioned earlier, the high repeatable nature of this shock tube is because of its diaphragm-less separation between the driver and driven section eliminating the replacement of traditional diaphragm after every shock which is the case in most traditional shock tubes.

The initial state of the miniature shock tube has the solenoid driven valve separating the driver gas and driven gas with the optical section exposed to the X-ray radiation. During each experimental shock tube cycle, the driven section is filled with the test gas to a pressure P_1 and the driver section is filled with helium to the pressure P_4 . Once the shock tube is prepared for experiment, the fast-acting solenoid is fired causing the spring-return valve to open and initiating a normal shock which propagates downstream towards the end wall driven section. Following this, the post shock gases are vented out and the cycle is repeated for the next shock to be fired. The miniature HRRST is designed to reach cycle rates of 4 Hz and to be reproducible for thousands of shots.

To monitor the passage of the shock, i.e. the measurement of incident shock velocity is done by measuring the times-of-arrival of the incident shock using the 5-sidewall mounted Dyansesn CA-1135 piezo electric transducers. The measurement of reflected shock pressure profile is carried out by using an end wall pressure transducer (PCB-105C12) which is inserted into the driven section end wall centered along the axis of the shock tube.

The end wall section of the miniature shock tube is the test section which has been previously used for various combustion studies such as tunable diode laser (TDL) absorption [4] and time-of-flight mass spectroscopy (TOF-MS) [16] in a smaller version of miniature HRRST (bore = 6.35mm). However, the end wall section serves as the optical section which is the measurement region while performing the X-ray densitometry experiments. The cycle of filling and evacuation of the test gas is handled by the custom pneumatic valves and the directional control valves (Parker Viking Extreme series) for which the fill valve

is located near to the driver section and the vent valve is located near to the driven section end wall. For the experiments performed here the test gas used was Ar (99.955% Airgas) and the driver gas used was He (99.995% Airgas).

The shock tube operation and the data acquisition for each experimental cycle is handled by custom software written in LabVIEW where every single individual experiment is tracked thereby collecting the data which includes the high-speed measurements associated with each experiment (reflected shock pressure transducer readings, incident and transmitted intensities) using a mixed signal oscilloscope (Yokogawa DLM2054). The meta-data for each experiment such as initial temperature (T_1), shock velocity (V_s) are also obtained by using a custom transducer timer readout for the time arrival sensors and the other pre-shock measurements which are necessary to calculate the important conditions behind the incident and reflected shock regions using the ideal normal shock equations.

2.4 Experimental setup for X-ray densitometry experiments at APS

X-ray densitometry experiments were performed in 7BM- B hutch at Advanced Photon Source at Argonne National Laboratory. X-ray radiation of 9keV energy was used throughout the whole experiments whereas the previous experiments were performed at 8keV and 10keV energies [30] on a different shock tube. Experiments performed at APS required the setup to occupy a limited amount of space due to the space constraint. Therefore, the vertical alignment and the miniature size of the shock tube helped solving this problem.

The X-ray densitometry experiments were performed with the miniature HRRST mounted on a 3-axis stage vertically with the driver section up and the test section at the bottom as shown in Figure 12. The whole shock tube was situated on a base which was free to move with the optical setup associated with it being fixed. The shock tube was oriented in such a way that the synchrotron beam traversed the shock tube perpendicularly to the direction of the propagation of the shock wave. The optical setup had a BIM diode (Hamamatsu S3590) placed between the synchrotron source and the optical section of the shock tube to measure the incident intensity of X-ray radiation and a PIN diode (Hamamatsu S3590) placed ahead of the

optical section to capture the transmitted intensity of X-ray radiation. It was possible to move the shock tube with great precision and accuracy to carry out quantitative density measurements at various locations and the experimental setup at 7BM-B at APS is shown in Figure 12 with the X-ray source placed perpendicular to the optical section of the shock tube.

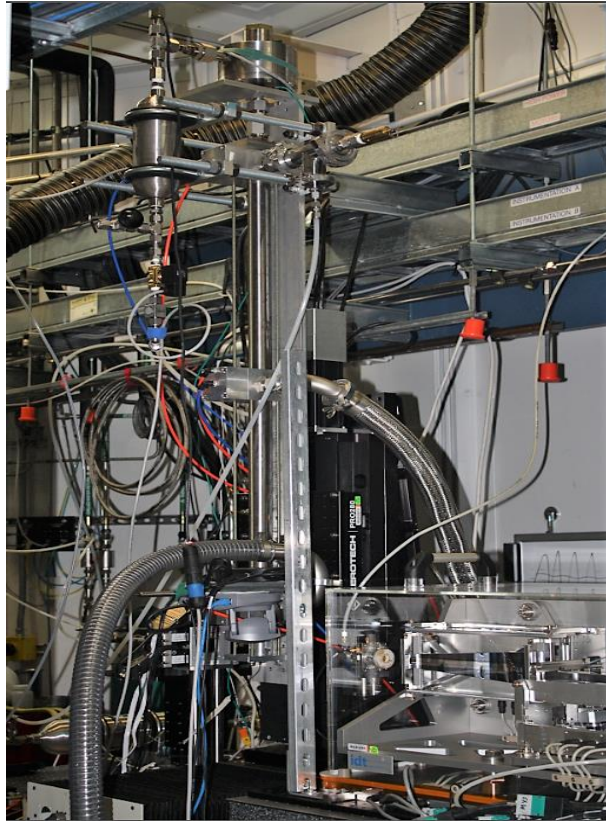


Figure 12. X-ray densitometry experimental setup at 7BM-B hutch at APS (ANL)

The vertically aligned miniature shock tube with the optical section at the bottom was precisely moved to change the measurement location. This precise movement was possible due to the setup provided at the 7-BM -B hutch at APS. Over the course of many experiments the driver section pressure was maintained constant. During the experiment, as the shock propagates towards the test section, the X-ray beam of 9keV traversed the optical section where some of the radiation is absorbed by the test gas moving behind the incident shock as well as the reflected shock. The incident and transmitted intensities were recorded by the photodiode combination. The complete setup of the X-ray densitometry experiments along with the photo

diodes can be shown by a schematic representation of the setup as shown in Figure 13 along with the optical access. The cycle rate at which the miniature HRRST was operates ranges from 0.25-0.33 Hz.

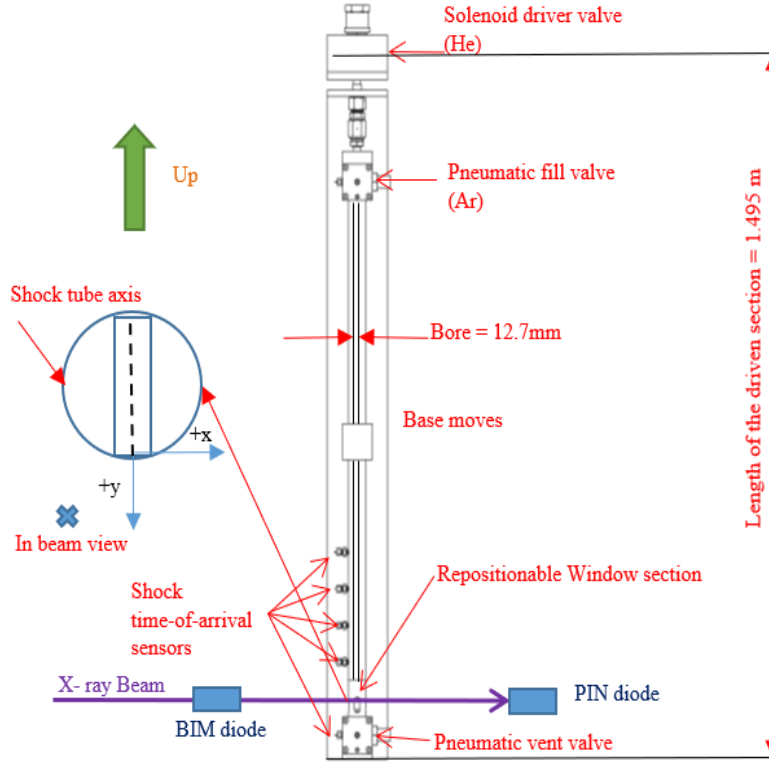


Figure 13. Schematic of HRRST while conducting X-ray densitometry experiments

2.4.1 Optical access for X-ray densitometry experiments

The inset in Fig 13. shows the optical access during the experiments which covers the whole diameter of the shock tube. The optical access is provided by a repositionable window section approximately of 13.5mm (centered on the axis of shock tube i.e. -6.75mm to +6.75mm) x 22mm measured from the end wall of the window section which is replaceable depending on the experiment without increasing the length of the driven section. The window section is comprised of a polycarbonate tube with a thickness of 1mm and the internal diameter 6.35 mm same as the shock tube which was placed carefully to avoid any disruptions from the shock tube bore. The polycarbonate is transmissive to X-rays. However, it degrades over time from the X-ray radiation for a continuous set of experiments and was replaced

periodically. The optical access is shown in Figure 13 which describes the whole coordinate axes x and y which represent the various transverse locations and various distances from the end wall. The advantage of having a repositionable window section was that it gave the ability to perform numerous experiments across different sections of the shock tube which included distances along various transverse x locations and at various distances from the end wall. These experiments summed up to a total of approximately 20,000 experiments which indicates high repeatability of the miniature HRRST. A detailed sketch of the optical section as described previously along with the distances in x and y direction is shown in the Figure 14.

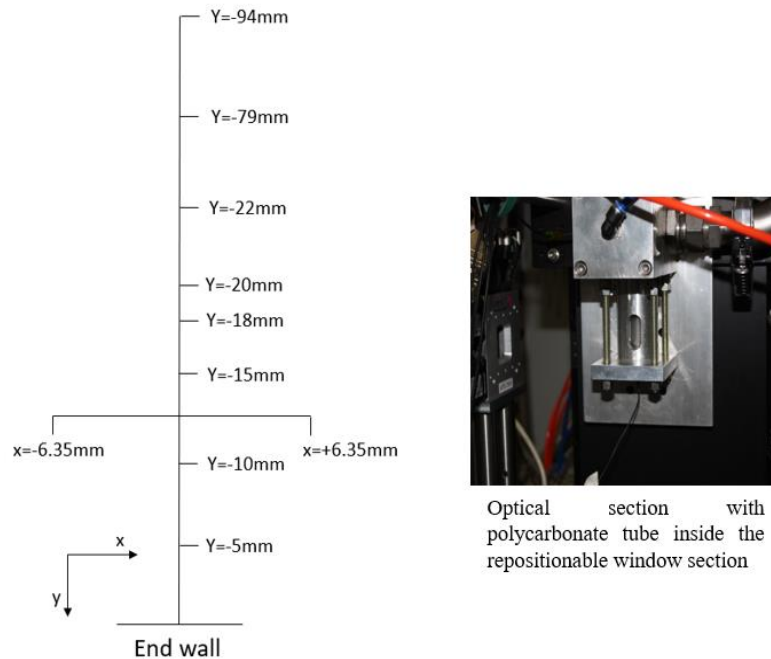


Figure 14. Schematic representation of different transverse x locations and distances from end wall and the optical section with polycarbonate tube sitting inside

The y -axis in the above figure represents the different distances from the end wall of the shock tube at which the measurements were taken and for each of these y locations corresponding measurements at various transverse x locations represented along the x -axis were taken. The experiments conducted at these locations both in positive and negative x direction helped in achieving the radially resolved density profiles. The distance $y = -5\text{mm}$ is the nearest to the end wall and the distance $y = -94\text{mm}$ is the farthest from the end

wall. For each of these locations the main measurements of time resolved density, density variation with transverse x locations and finally the radially resolved density are evaluated.

One of the important issues to be addressed is the uncertainty in experimental measurement. The final quantity being measured is the density of the test gas. However, the uncertainty in the measured quantity is not due to a single uncertain parameter involved in measurement. The density measured by conducting X-ray densitometry experiments is a complicated calculation. This is because of several uncertain parameters involved in obtaining the final density measurement. The list of parameters that govern the experimentally determined density and calculated density by using ideal normal shock relations are listed in Table 2. The descriptions of the parameters can be referred to the appendix.

Table 2. List of parameters governing the experimental and calculated densities

Experimental density ($\rho_{\text{experimental}}$)	Calculated density ($\rho_{\text{calculated}}$)
Transmitted intensity (I_1)	Initial pressure (P_1)
Transmitted intensity (dark) ($I_{1(\text{dark})}$)	Initial temperature (T_1)
Incident intensity (I_0)	Shock velocity (V_s)
Incident intensity (dark) ($I_{0(\text{dark})}$)	
Tau-empty (τ_{empty})	
Path length (PL)	
Absorption coefficient ($\sigma_{9\text{keV}}$)	

The transmitted and incident intensities during experiments and under no light conditions are denoted by I_1 , I_0 , $I_{1(\text{dark})}$, $I_{0(\text{dark})}$ respectively. The other parameters are transmissivity through the shock tube when there was no gas present denoted by τ_{empty} , path length through the shock tube denoted by PL and the absorption coefficient denoted $\sigma_{9\text{keV}}$. The number of independent variables is more in case of experimental density when compared to the independent variables in calculated density.

3 COMPUTATIONAL MODELLING

3.1 Capability of Ensemble Averaged Data

The two unique features of the miniature high repetition rate shock tube - High repeatability and reproducibility enabled the modeler to perform the ensemble averaging of data. First, the high repeatability nature of the shock tube allows the user to conduct thousands of experiments in a single experimental cycle. As previously mentioned, a total of 20,000 experiments were conducted spread through different sections of the shock tube were possible because of this unique feature. The repeatability nature of the miniature shock tube can be related by looking at the number of experiments performed in each experimental cycle and are tabulated in Table 3.

Table 3. Averaged experimental conditions for all scans of experiments

Scan file	Y location (mm)	No. of experiments	Pressure (Torr)			Temperature (K)		
			P1	P2	P5	T1	T2	T5
Scan_2390 Scan_2391	Y = -5	1710	185.85	1319.97	4948.50	300.5	806.1	1463.87
Scan_2382 Scan_2383	Y = -10	1680	194.67	1341.95	4972.52	300.29	789.55	1424.78
Scan_2401 Scan_2404	Y = -19	1680	195.78	1391.66	5219.75	300.63	818.03	1492.21
Scan_2387 Scan_2388	Y = -20	2100	197.89	1310.88	4782.24	300.08	768.57	1375.19
Scan_2389	Y = -22	1650	185.03	1293.55	4821.35	300.69	798.13	1444.61
Scan_2400	Y = -79	1650	178.05	1263.98	4738.28	300.92	806.83	1465

The ensemble average of the data is not limited to be performed for each cycle of experiments. There are various encounters in the data analysis where the ensemble average of data is performed based on a single parameter such as x locations or time after shock reflection. This other version of ensemble averaging is the binning operation which is performed over the transverse locations which is possible due to the second unique feature of high repeatability and will be discussed in the later section. In addition, the ensemble averaging was also performed based on the time of shock propagation to evaluate certain reference quantities such as the average density behind the reflected shock.

3.2 Analysis Scheme for processing the experimental data

One of the most challenging part of this study was to analyze all sets of data obtained from the experiments and reduce it to deduce important results and conclusions. Several scans of experimental data along with the calibration were analyzed by using a custom Python data processing software. Therefore, the goal of achieving the important results was by performing the analysis in a step by step fashion. The systematic approach of the analysis is highlighted in Figure 15.

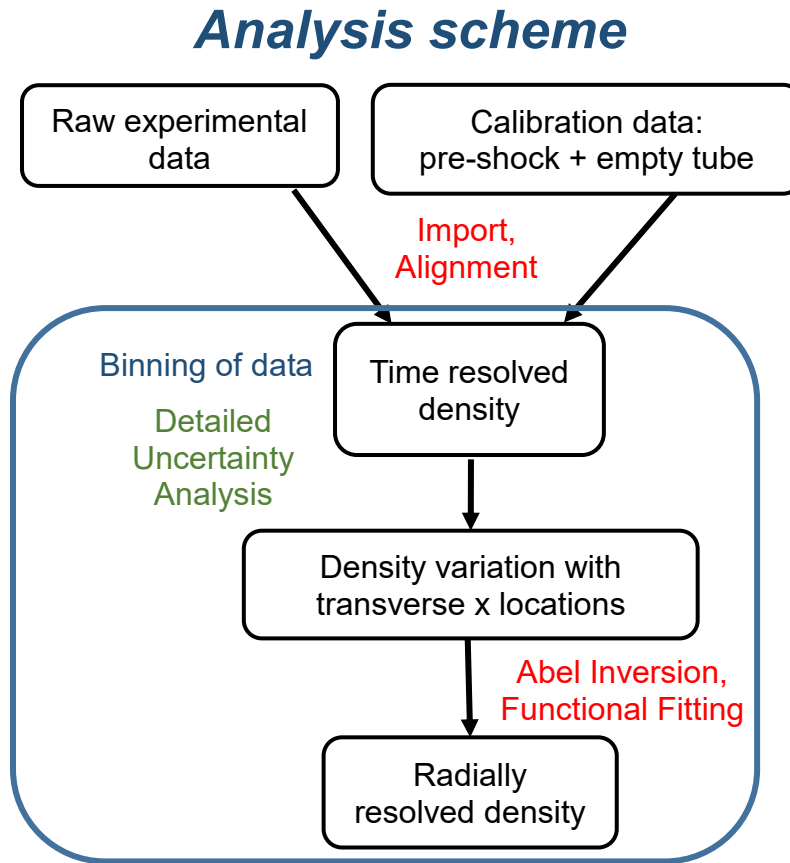


Figure 15. Analysis scheme for data processing of X-ray densitometry experiments performed in miniature HRRST

The algorithm first loads the calibration scans and the experimental scans of data. The next parts aligns the data, calibrates pre-shock and empty (no test gas) raw data, resulting with time varying density, Density variation with x locations and the final processing of radially resolved density are performed later. The scheme is shown above and elaborated in the further sub-sections.

3.2.1 Processing and alignment of Raw Data

The raw data such as the incident and transmitted intensities and end wall pressure traces are obtained from the data acquisition software. Every line-of-sight measurement conducted is a time-resolved measurement. However, the time at which the shock passes the measurement region is different for each experiment relative to the trigger even though the nominal conditions are same. The problem arises if the ensemble average is to be performed. Hence, the solution to this problem was to align the data properly with respect to the time at which the shock passed the measurement location. The alignment of the raw data was performed by locating the index (position) of the first data point with respect to the location of the shock passing through the measurement location i.e. the rise time and with respect to the time from which reflected shock reflects from the driven section end wall. Also, the relative measurements of time at which the incident shock and reflected shock arrived at the test location were determined.

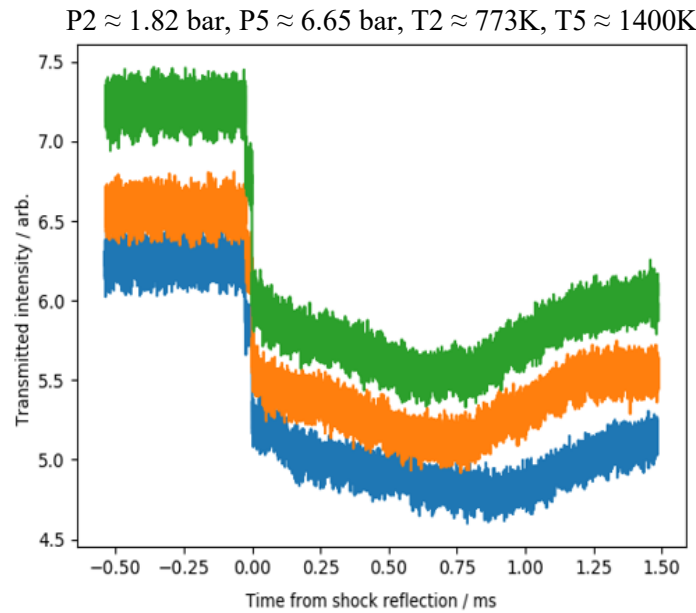


Figure 16. Transmitted intensity profiles for a random of 3 experiments for scan 2390 and scan 2391

As an example of the aligned raw data, transmitted intensity profiles for a random of 3 experiments are shown in Figure 16 for the scan 2390 and scan 2391 whose measurement region is 5mm from the end wall i.e. $y=-5\text{mm}$. The variation in the location of the shock passing through the measurement location and the reflected shock from the end wall driven section are handled by using the custom python method. However,

the high reproducibility advantage helped in performing an ensemble average of the experiments associated with these scans. The result of using this function reduces the scatter in the profiles of the data associated with the experiments. The procedure for evaluating the averaged aligned profiles accounts for the offset in times for different experiments. As an example, the averaged transmitted intensity profile for the same scans of 2390 and 2391 is shown in Figure 17.

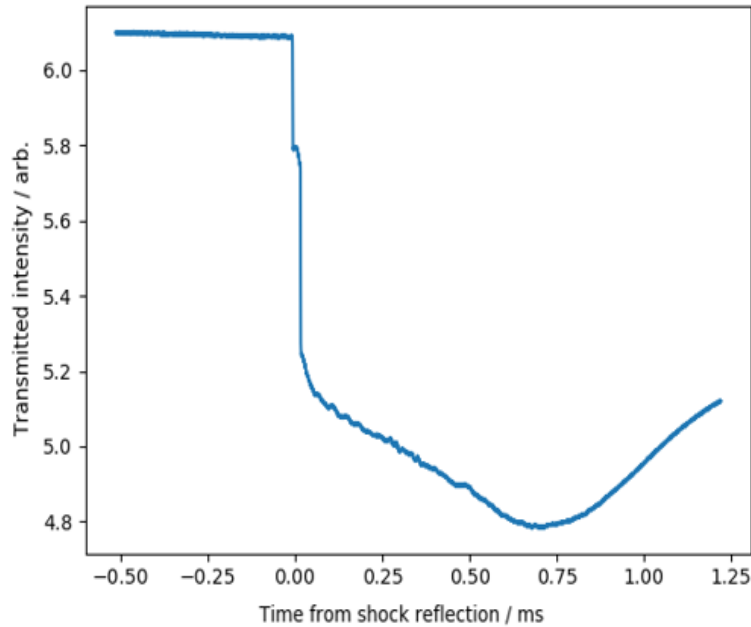


Figure 17. Flattened transmitted intensity for 1710 experiments associated with scans 2390 and 2391

Performing the ensemble average of the data obtained from experiments associated with one scan, results in less scatter as seen in Figure 17. However, there would be a penalty of losing the information specific to an experiment which interests the modeler by performing the ensemble averaging. The next part of the analysis is the calibration of the empty and pre-shock data and is performed to assess the effectiveness of the data available in each scan.

3.2.2 Calibration of empty and pre-shock data

The transmission of X-rays through the shock tube depends on density of the test gas, path length through the shock tube and the absorption coefficient as discussed previously. The path length through the

shock tube depends on the path length through the test gas region and the polycarbonate wall thickness to be traversed. This combination of the path lengths changes with every measurement section of the shock tube. Therefore, the transmissivity through the shock tube is not a simple calculation, instead it becomes a challenge to incorporate this complexity. It is important to realize that the path length through the shock tube bore or through the test gas decreases from the center of the shock tube all the way to the extreme transverse x location near to the walls. Whereas, the polycarbonate wall thickness increases from the center of the shock tube with maximum at the extreme ends as shown in Figure 18.

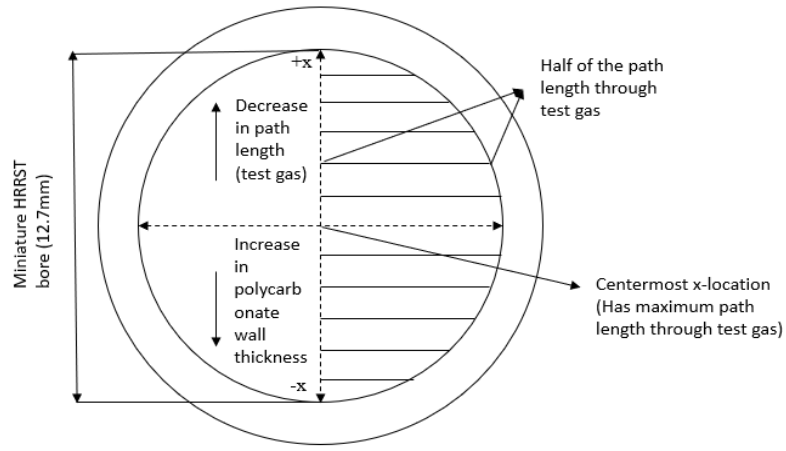


Figure 18. Half sectional view of the miniature HRRST viewed along the axis of the shock tube representing varying path length and polycarbonate wall thickness along transverse x-locations

Hence, the measured transmissivity through the shock tube during the experiments would incorporate both the transmissivity through the test gas and transmissivity when there is no gas present and can be represented by Equation 2, 3 and 4.

$$\tau = \tau_{shocktube} * \tau_{air} * \tau_{wall} \quad (2)$$

Rearranging this we get,

$$\tau_{shocktube} = \frac{\tau}{\tau_{air} * \tau_{wall}} \quad (3)$$

$$\tau_{shocktube} = \frac{\tau}{\tau_{empty}} \quad (4)$$

Where $\tau_{shocktube}$ is the transmissivity through the shock tube, τ_{empty} is the combination of τ_{air} (a small approximately constant absorption in the air columns between the beampipe and apparatus and apparatus and detector) and τ_{wall} which is the transmissivity through the shock tube when there is no gas present i.e. transmissivity through the polycarbonate wall.

The data associated with the transmission through the shock tube when there is no gas present is denoted empty data and the data associated with the transmission through the shock tube when there is no shock propagation is called the pre-shock data. The value of τ_{empty} is obtained by using a robust calibration method which linearly fits the empty and pre-shock data to the calculated models by using five parameters $R_i \rightarrow$ Inner radius, $R_o \rightarrow$ Outer radius, X_{offset} , wall slope and wall intercept. The calculated model for empty and pre-shock data essentially was dependent on the wall slope which is the absorption coefficient and wall intercept being the offset when extrapolated to zero wall thickness and is given by Equation 5

$$\ln(\tau_{calc}) = wall\ intercept + wall\ thickness * wall\ slope \quad (5)$$

Table 4. List of five parameters associated with different scans of experiments

Scan file	Y location(mm)	R _o (mm)	R _i (mm)	X _{offset} (mm)	Wall_slope	Wall_intercept
Scan_2390 Scan_2391	Y=-5	7.3525	6.3582	0.0086	0.4847	-2.3728
Scan_2382 Scan_2383	Y=-10	7.3286	6.3278	0.019	0.3957	-1.9636
Scan_2387 Scan_2388	Y=-20	7.3611	6.3355	-0.0395	0.4220	-2.1124
Scan_2389	Y=-22	7.3601	6.3545	-0.0637	0.4528	-2.2329
Scan_2400	Y=-79	7.3616	6.3786	0.0021	0.4623	-2.4571
Scan_2401 Scan_2404	Y=-94	7.3541	6.3509	-0.1019	0.4643	-2.2125

Although, the five controlling parameters discussed earlier have different contributions to the fitting function, it cuts down essentially to one parameter of wall intercept having the large contribution. To show this a table consisting of the five-parameter contribution associated with different scans is shown in Table 4. It is evident that the variation in the outer and inner radius of the shock tube is not significant when compared to the rest of the parameters. The variation in X_{offset} and wall slope is not that significant with 0.6-8% and 2-7 % respectively and hence does not contribute largely to the fitting model whereas a significant variation of 8-50% in wall intercept is directly contributing to the fitting function as seen from the Equation 5. This is due to the maximum relative variation of wall intercept in determining the calculated model and fitting the respective data to it.

These calculated models once established, are used to find the value of τ_{empty} by applying the logarithm to the Equation 4

$$\ln(\tau_{\text{empty}}) = \ln(\tau) - \ln(\tau_{\text{shocktube}}) \quad (6)$$

Taking the anti-logarithm of Equation 6, we get the value of τ_{empty} given by Equation 7

$$\tau_{\text{empty}} = e^{-(\ln(\tau) - \ln(\tau_{\text{shocktube}}))} \quad (7)$$

Where $\ln(\tau)$ is given by Equation 5 and $\ln(\tau_{\text{shocktube}})$ is given by Beer's law as stated by Equation 1 relating the density of the test gas, path length through the test gas and the absorption coefficient. However, it was observed that the polycarbonate tube thickness degraded over time from the X-ray radiation for a continuous set of experiments and was replaced periodically. However, this degradation effected the τ_{empty} calibration for which a modified calibration was employed for a whole set of experiments at various transverse x locations to a τ_{empty} function which accounted for the geometry.

The calibration of the empty and pre-shock data was possible by incorporating these equations in a custom python method. The results obtained by performing the calibration method were in good

agreement for all the y locations and only the results associated with the scan 2390 and 2391 are discussed here.

3.2.2.1 Demonstration of calibration method

The results generated for the calibration of empty and pre-shock data are discussed in this section starting with the calibration of empty data. The empty data calibration is performed by finding a fit to the experimental data using Equation 5 to calculate the empty model which is a linear equation in terms of wall intercept and slope. This led to a plot comparing the empty data (transmissivity) to the calculated model varying with the wall thickness.

1) Plot for empty data and empty model vs wall thickness

A plot showing the logarithm of empty transmissivity data being fit to the calculated empty model is shown in Figure 19.

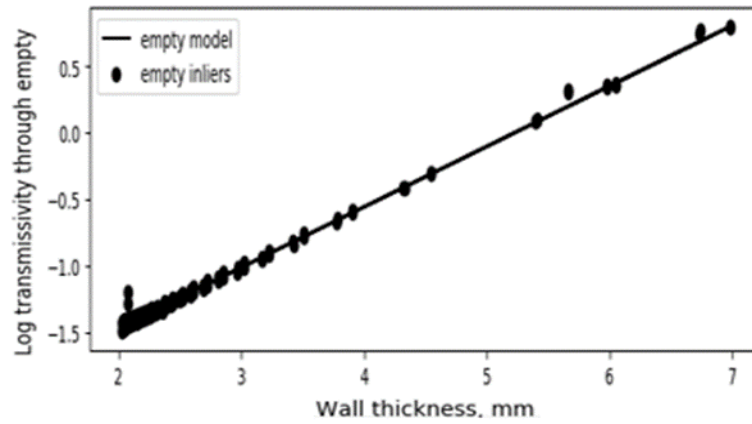


Figure 19. Calibration plot for empty data fit to calculated empty model

The plot shown is essentially the logarithm of τ_{empty} comprising of empty data represented by black dots varying with the polycarbonate wall thickness along with the empty model obtained by the parameter fit. The plot shows excellent agreement between the empty data and the calculated model having a linear relation with the increasing wall thickness as obtained from Equation 5. However, the data points at maximum wall thickness locations scatter slightly away from the model and is because of the presence of

uncertainty and noise at these locations accounting for the fact that there is only a small fraction of shock tube path length present.

2) Plot for pre-shock data and pre-shock model vs wall thickness

The success of the calibration not only depends on well calibrated empty data but also on good calibration of pre-shock data which involves transmission of X-rays through the test gas before the start of experiment. A similar comparison between the pre-shock transmissivity and the calculated pre-shock model using the Equation 5 along with the empty model is shown in Figure 20.

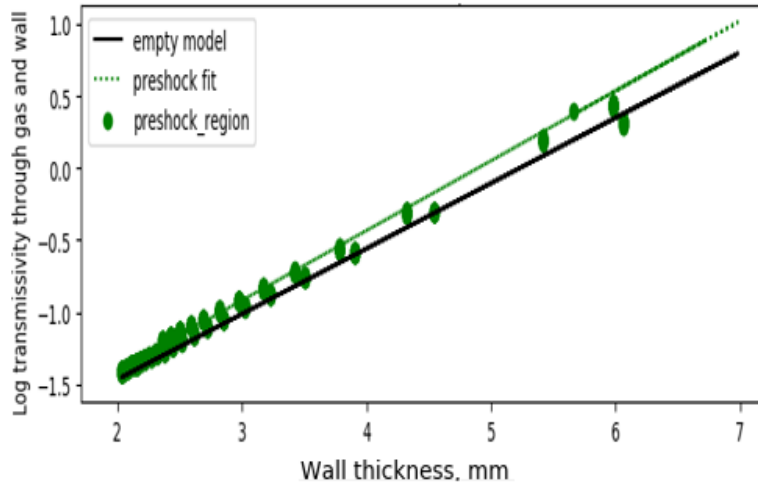


Figure 20. Pre-shock calibration plot w.r.t polycarbonate wall thickness

It is evident from the plot that, the logarithm of the pre-shock transmissivity has a very good agreement with the calculated pre-shock model and is in linear relation with the increasing wall thickness. The plot has the similar trend of increase in scatter as higher wall thickness is approached. This is due to the availability of short shock tube path length at these locations. However, the comparison between the pre-shock data and model to the empty model shows that, the transmissivity in case of pre-shock is less than the case of empty as there is absorption when there is gas present in the path of transmission. The calibration of the empty and pre-shock data has been performed using the fitting Equation 5. However, the

important discussion on the problem of varying path lengths across different sections would help in determining how good the calibration of data was performed.

3) *Combination of calibration plot vs x location*

The interesting plot which combines the empty data, pre-shock data, calculated models for both empty data and pre-shock data and a calculated empty model from the pre-shock data using the Beer's law and given by the Equation 7 is shown in Figure 21. The purpose of this plot is to determine the success of the calibration performed in the previous sections for empty and pre-shock data. In addition to this, an empty transmissivity model calculated by subtracting the transmissivity obtained through Beer's law from the fitting model is also shown in the figure below.

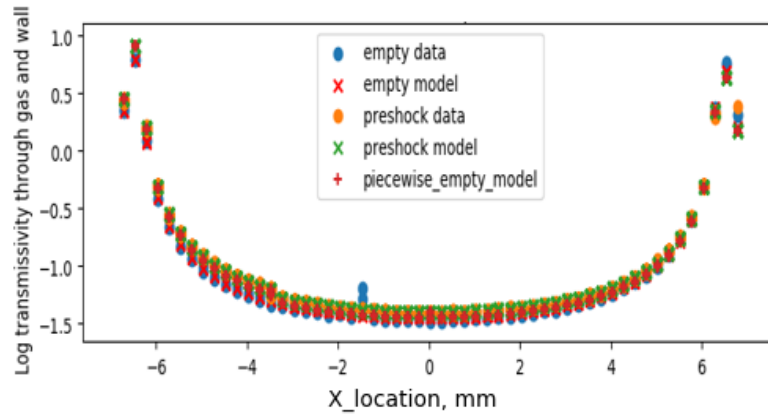


Figure 21. Combination calibration plot for empty, pre-shock data and their corresponding models

It is evident that as the x-location varies from the center i.e. 0mm to the extrema at the both ends, the agreement of the data with the model is very strong throughout with the exception at the extreme ends where the data has some uncertainty and noise due to the increased path length through polycarbonate wall and decreased path length through the shock tube test gas. Also, the transmissivity through the shock tube when there is gas present with no shock fired is low in comparison to the transmissivity when there is no gas present. The case where the polycarbonate wall thickness was degrading due to continuous X-ray radiation was handled by a customized calculation called piecewise model which accounted for the inaccuracies in geometry of measurement region. Therefore, a combination of these various calibrations

resulted in a very good agreement between the empty, pre-shock and their respective models as the measurement section was varied as shown in the figure.

4) *Pre-shock transmissivity and model vs shock tube path length*

The agreement of the pre-shock data and model varying with wall thickness has been previously discussed. However, it is important to evaluate the agreement in the pre-shock transmissivity varying with the shock tube path length calculated from the geometry. Therefore, a plot showing the logarithm of pre-shock transmissivity and its exponential version is given by Figure 22. It can be seen that there is a good agreement in the data and model as the path length through the shock tube is increased. However, the trend for the scatter in data is seen at the lowest shock tube path lengths which essentially have the largest wall thickness as seen in Figure 20. The pre-shock model in this case was calculated using Beer's law with the absorption coefficient taken to be 85.98 g/cm^2 . The same trend is observed in the exponential version of the plot with the only difference in the magnitude.

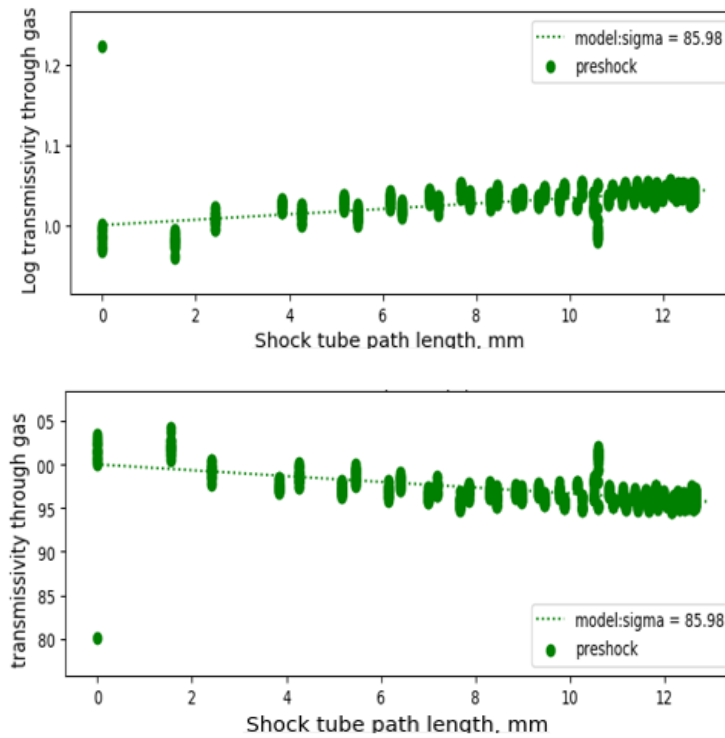


Figure 22. Calibration of pre-shock data involving pre-shock transmissivity and model varying with shock tube path length

3.2.3 Time Resolved Density measurement

The data obtained from several lines-of-sight measurements across different sections of the shock tube upon performing alignment and calibration results time resolved data. However, the desired measurement by conducting X-ray densitometry experiments was density and can be obtained by relating the X-ray transmission, path length through the shock tube and the photo-absorption coefficient by Beer's law. The formula used to get the density from the transmission of X-rays through the optical section is given by the Equation 8 which is the logarithmic form of Beer's law and Equation 9 as previously mentioned in Section 3.2.2.

$$-\log(\tau_{shocktube}) = \rho * \sigma * PL \quad (8)$$

$$\rho = \frac{-\log(\tau_{shocktube})}{\sigma * PL} \quad (9)$$

Where, ρ is density, $\tau_{shocktube}$ is the transmissivity through the shock tube, σ is the photo-absorption coefficient and PL is the pathlength through the shock tube. Concentration of the test gas was initially obtained from which the density was calculated. The time resolved density can be obtained with respect to time of incident shock arrival at the end wall or the time from which the reflected shock bounces off the end wall driven section. A detailed discussion on the density profiles at a single location, multiple distances from end wall of driven section and along transverse x locations is studied in results and discussions section.

3.2.3.1 Binning of data – Performed in later stages

In addition to the high reproducibility nature of the miniature shock tube which allowed to conduct several experiments with steady conditions in a small time-period., the high repeatability nature of the miniature shock tube gave the advantage to conduct several experiments at the same transverse x location. Most of the scans of experiments had 52 transverse x locations with each x location containing 30 experiments associated with it. This made it possible to perform the binning method which essentially computes the average of the experiments. Implementing this helped in reducing the scatter in the data obtained and made it less complicated to perform other analytical techniques. Binning of experiments was

performed by writing a custom Python method which works on the concept of finding unique x values in a whole scan of experiments and stores the experiments with same x values in their respective bins. The new generated set of experiments is created which contains the average of experimental data associated with the experiments having the same x locations.

However, having several experiments at one location always provides the advantage of averaging of experiments as an option but it became a necessity to obtain the density variation with radius of the shock tube. This is due to the procedure involved in obtaining the radially resolved density profiles which uses the averaged lines-of-sight measurements along the transverse x-locations. Every result including time resolved density, uncertainty analysis and radially resolved density are obtained for the case of binned experiments.

3.2.3.2 Uncertainty analysis using error propagation

The estimation of uncertainty in a quantity depends on how the quantity is measured or calculated. The calculation can range from being a simple mathematical operation to solving a complex equation. The measured quantity in this study which is density of the test gas is obtained via a complicated procedure which involves several uncertain parameters. Hence, a simple approach to obtain the uncertainty was not sufficient for this study. For this purpose, a comprehensive uncertainty analysis for the experimental and calculated densities is performed with the use of error propagation analysis [38] concept. The concept of error propagation analysis is based on the estimation of the uncertainty in the final measurement by calculating the sole effect of uncertainty in each quantity incorporated to get the final measured quantity. The uncertainty in a quantity which is a combination of other quantities whose uncertainty is assumed on an experimental basis is calculated using the formula adapted from [38] where the uncertainty contributed by independent variable is obtained by partially differentiating the function f with respect to that variable. It is assumed that the errors in x_i are uncorrelated. The collective uncertainty in the function f is given by Equation 10.

$$\delta f = \frac{\partial f}{\partial x_1} * \delta x_1 + \frac{\partial f}{\partial x_2} * \delta x_2 + \dots + \frac{\partial f}{\partial x_n} * \delta x_n \quad (10)$$

Where $f = f(x_1, x_2, \dots, x_n)$ is a function of measured quantities x_i and the errors associated with them are σ_i . Once, the individual contribution of the independent variables is obtained, the procedure to find the root mean square deviations is employed which essentially is squaring and adding the average of the series of measurements which essentially would lead to a final expression given by Equation 11.

$$\sigma_f^2 = \sum_{i=1}^n \left(\frac{\partial f}{\partial x_i} \right)^2 * \sigma_i^2 \quad (11)$$

Where, σ_f is the uncertainty in the function itself, σ_i is the uncertainty associated with the individual variable and $\frac{\partial f}{\partial x_i}$ is the partial derivative of the function with respect to the variable. Using this concept of error propagation, the uncertainties in the experimental and calculated densities were obtained.

3.2.4 Time resolved density variation with various transverse x-locations

One of the important steps in measuring the radially resolved density profile to interpret the boundary layer formation in a small-bore shock tube is to assess the variation of density along various transverse x-locations. The various lines-of-sight measurements at various distances from the center of the shock tube axis as a center at a specific y-location were carried out both in positive and negative x direction. Each of the transverse x location had a different shock tube path length calculated from the geometry where, the center x-location had the largest shock tube path length and the extreme x location in both positive and negative direction had smallest shock tube path length due to the nature of symmetry. However, the variation in the polycarbonate wall thickness was opposite of the path length variation where, the center x-location had the smallest path length through polycarbonate wall thickness and the extreme x locations had the largest.

The flexibility in measuring across different locations in the miniature HRRST was possible due to the free movement of the base with the shock tube mounted on it and repositionable window section. The positioning of different locations in the optical section was handled precisely by the synchrotron facilities.

A spacing of 0.25mm between two consecutive x locations was placed for most of the experiments except for the scan 2412 where the measurement location was distanced 18mm from the end wall with 0.02mm as the spacing.

The initial intuition regarding the density profiles varying along various transverse x-locations is to have very good agreement of density at the centermost locations when compared to the extreme locations due to the presence of certain uncertainty and noise at the extreme locations because of the variation in path length as discussed. The additional details along with the figures are reported in the following sections.

3.2.5 Radially resolved density measurements in miniature HRRST

The basic idea behind the interpretation of growing boundary layer in the miniature shock tube is to study the density variation with the radius of the shock tube. Thereby, indicating the effect of the boundary layer on the density as the radius is approaching the side wall. To obtain the final milestone of obtaining the radially resolved density profiles, a well-established analytical technique called Abel Inversion [39] is used which reconstructs the radially resolved density when a series of lines-of-sight density measurements across various transverse x-locations are available. Though there are several approaches to use the Abel Inversion technique, a simple and elegant approach termed as Onion Peeling approach [40,41] has been used to achieve the desired measurements.

3.2.5.1 Abel Inversion - Onion Peeling Approach

The Onion Peeling approach incorporates the principle of tomographic reconstruction of the density profile when a line of sight projection of the density is provided. The procedure involved in this approach can be emphasized in three main steps and are described in detail below-

i. Sub-division of shock tube section:

The procedure begins with assuming a circular plane perpendicular to the axis of the shock tube at a specific distance from the driven section end wall where 52 line-of-sight measurements were taken across the whole

section of the shock tube. The circularly symmetric plane is now divided into 26 equally spaced zones or annuli with a spacing of 0.25mm which is half the number of lines-of-sight measurements.

ii. Evaluation of different chord lengths associated with annuli:

The various lines-of-sight measurement across the divided shock tube section annuli results in unique chord lengths associated with each annulus and respective transverse x location. The calculation of the chord length was performed using geometry. This resulted in formulating a chord length matrix $[L]$ whose size is given by $l \times k$ where, l is the number of chords (52) and k is the number of zones (26) in which the shock tube section is divided. Although the mathematical significance of the chord length matrix has been highlighted, the physical significance of the $[L]$ matrix can be stated as- when multiplied by a hypothetical radially distributed density profile it would result in the average density measurement across a line-of-sight. This process is termed as the Forward Abel Transform and is given by the Equation 12.

$$D(r) \times [L] = \frac{1}{dr} \times D(x) \quad (12)$$

Where, $D(r)$ is the radially varying density function, $[L]$ is the chord length matrix of size $l \times k$, dr is the spacing between the zones and $D(x)$ is the density variation along transverse x locations.

The variation of chord lengths associated with different annuli varying with different transverse x locations is shown in Figure 23. The number of annuli shown in the following figure is arbitrary and will vary with the number of transverse locations associated with each scan of experiments. The calculation related to the chord depends on outer and inner radius of the shock tube.

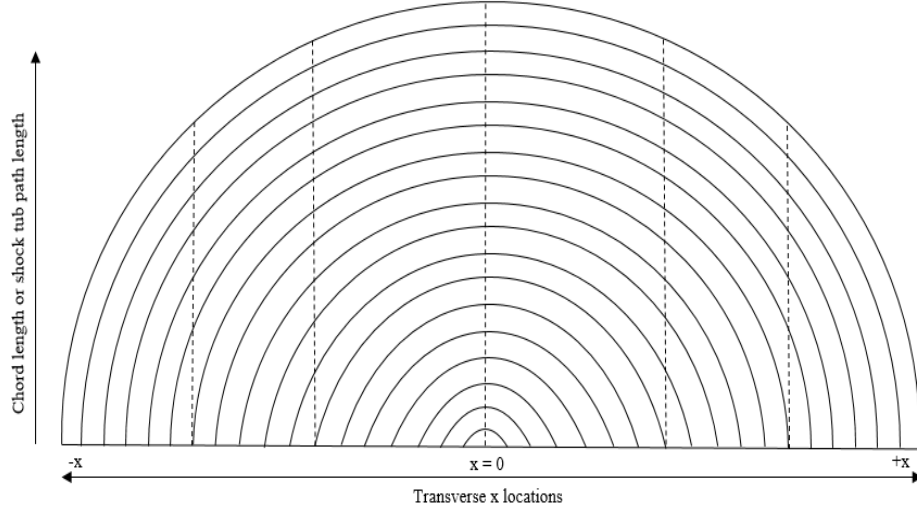


Figure 23. Chord lengths associated with different annuli along different transverse x locations

iii. Performing Abel Inversion:

The final step of the procedure is to perform the Abel Inversion which is a simple mathematical operation of inverting the chord length matrix $[L]$ and multiplying it by $D(x)$ which is the density variation along the x locations. This results in $D(r)$ which is radially varying density function as the other parameters are known ahead of this inversion. The mathematical expression for Abel Inversion is given by the Equation 13.

$$D(r) = \frac{1}{dr} \times [L]^{-1} \times D(x) \quad (13)$$

The use of Abel Inversion technique served the purpose of obtaining the radially resolved density profiles and the analysis of these profiles led to the estimation of growing boundary layer effect on the measured density along the side wall of the shock tube. Hence, addressing the cause of uncertainty in the reaction conditions behind the propagating shock wave.

4 RESULTS AND DISCUSSION

The high repeatable nature of the miniature shock tube allowed to conduct several experiments covering the whole region of optical section. The data obtained from the experiments performed at various line-of-sight measurements were analyzed by implementing the custom python data processing software. Approximately 20,000 experiments were performed at various line-of-sight measurements along the transverse locations and at various distances from the endwall as shown in Figure 14. The different scans of experiments for which the data analysis were performed and corresponding results were obtained are shown in Table 5 indicating the measure of reproducibility nature of miniature HRRST by maintaining steady operating conditions as shown in the table along with the scatter.

Table 5. Experimental pressures and temperatures associated with each scan. Upper value = average, lower value = 2σ

Scan file	Y location(mm)	No. of experiments	Pressure (Torr)			Temperature (K)		
			P1	P2	P5	T1	T2	T5
Scan_2390 Scan_2391	Y = -5	1710	185.85 8.33	1319.97 101.74	4948.50 484.25	300.5 0.88	806.1 35.95	1463.87 85.63
Scan_2382 Scan_2383	Y = -10	1680	194.67 5.66	1341.95 80.83	4972.52 412.17	300.29 0.68	789.55 29.67	1424.78 70.66
Scan_2401 Scan_2404	Y = -19	1680	195.78 49.35	1391.66 288.34	5219.75 974.92	300.63 0.91	818.03 179.50	1492.21 429.55
Scan_2387 Scan_2388	Y = -20	2100	197.89 9.63	1310.88 112.07	4782.24 558.43	300.08 0.77	768.57 46	1375.19 109
Scan_2389	Y = -22	1650	185.03 6.8	1293.55 175.10	4821.35 941.77	300.69 0.23	798.13 70.84	1444.61 169.04
Scan_2400	Y = -79	1650	178.05 5.33	1263.98 122.63	4738.28 603.04	300.92 0.5	806.83 46.46	1465 110.83

4.1 Time varying density measurement at a specific Y location

The experiments performed at various line-of-sight measurements included regions centered at various distances from the driven section endwall (i.e. the y direction in Figure 14). For these experiments, 52 transverse locations (i.e. x direction in Figure 14) were selected with a spacing of 0.25mm between each other. The reproducible nature of the miniature shock tube allowed to conduct 30 experiments at each of these transverse locations, which permitted in performing the ensemble averaging (binning) to improve the

signal to noise ratio. However, the incorporation of Beer's law led to first important result of time varying density which was obtained for every experiment performed.

As previously mentioned, the photo diodes record the incident and transmitted intensities of X-ray radiation where the former is the intensity coming from the source and the latter is the intensity after the absorption by anything in between the path. These intensities changed over the course of time due to the change in absorption by the medium. The variation between the transmitted and incident intensities for a single experiment and a binned experiment averaged over 30 experiments whose measurement region is centered at 5mm from the endwall (i.e. $y=-5\text{mm}$) and $x=0.03\text{mm}$ is shown in Figure 24.

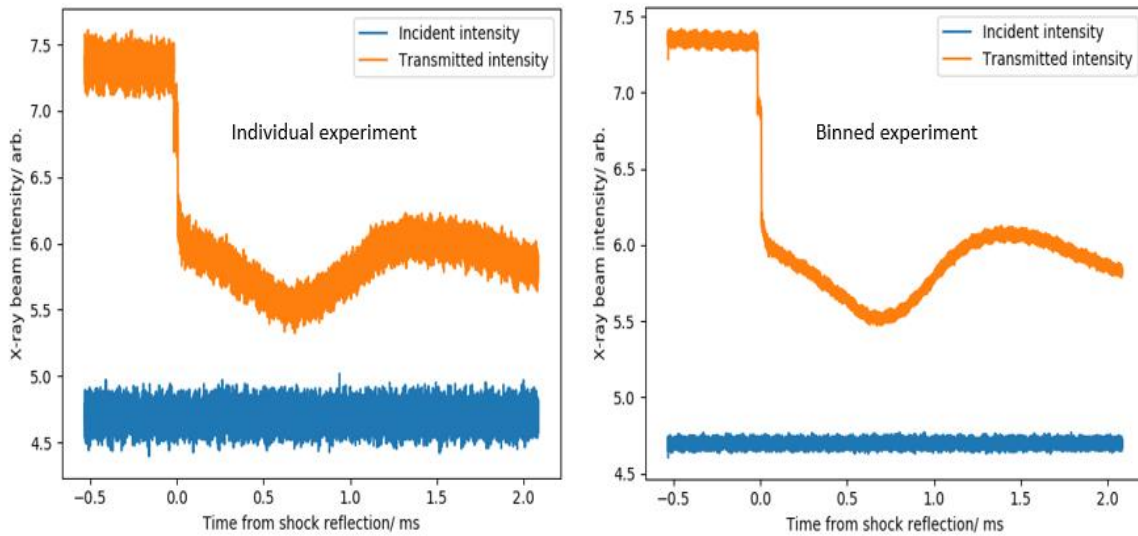


Figure 24. Incident and transmitted intensities for an individual experiment ($Y=-5\text{mm}$, $X=0.03\text{mm}$) left and binned experiment ($Y=-5\text{mm}$, $X=0.03\text{mm}$) right

The X-ray absorption in the medium is related to the path length through the polycarbonate walls and the density of gas present at the measurement location as in Beer's law, Equation (8) and (9). The transmissivity through the shock tube represented by $\tau_{shocktube}$ is the ratio of the transmitted and incident intensities along with τ_{empty} and its variation with time can be shown in Figure 25.

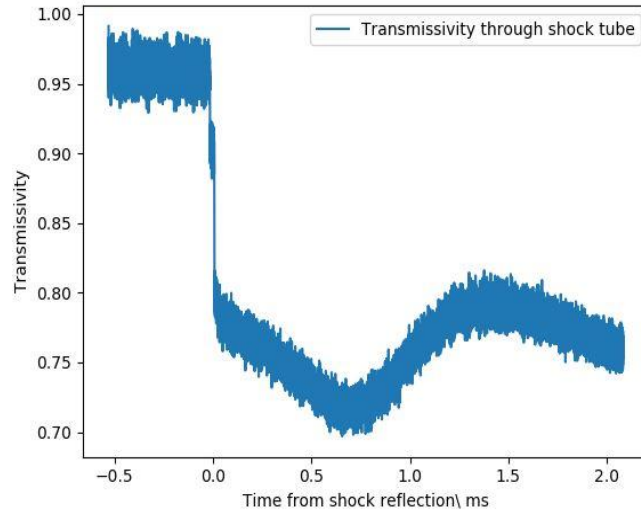


Figure 25. Time varying transmissivity through shock tube for a binned experiment ($Y=-5\text{mm}$, $X=0.03\text{mm}$)

It is evident from the profile that the transmissivity through the shock tube is constant for the time before the shock is fired i.e. the pre-shock condition and has a sudden decrease when the incident shock passes by the measurement location and further decreases when the reflected shock bounces from the end wall. The time-resolved density was measured using Beer's law which uses the transmissivity through the shock tube shown in Figure 25 and the corresponding path length. However, as previously mentioned, it was in the capability of the miniature HRRST to perform the binning of experiments at any stage of data processing and therefore, the representation of the analyzed data in the form of results is shown for both individual and binned experiments. The binning of data was performed based on the transverse x location leading to averaged values of the total set of experiments which had the same x location. A plot showing the individual experimental density as well as binned experimental density is shown in the Figure 26 associated with experiments of scan 2390 and 2391 with the measurement location of $y=-22\text{mm}$ and $x=-0.03\text{mm}$. The experimental conditions associated with these experiments were $P_1 = 0.2445\text{ bar}$, $T_1 = 300.7\text{ K}$ for pre-shock and $P_5 = 6.5\text{ bar}$, $T_5 = 1463.49\text{ K}$ for reflected shock. As seen from the figure, it is evident that the individual experimental density has more scatter in the data as compared to the binned experimental density which makes it difficult for the further analysis of radially resolved density measurements. For the sake of distinguishing between the different shock conditions during an experiment, the densities for the pre-shock,

behind the incident shock and behind the reflected shock conditions are segregated as shown in figure and are denoted by ρ_1 , ρ_2 and ρ_5 respectively.

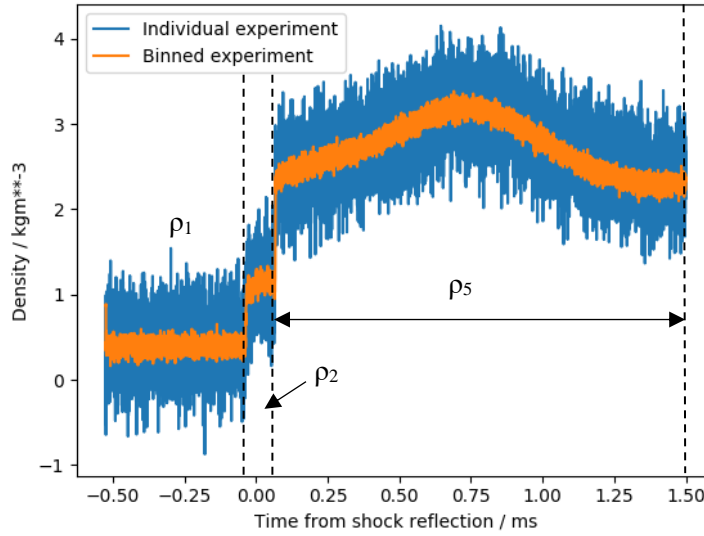


Figure 26. Density associated with an individual and binned experiment ($Y=-22\text{mm}$, $X=-0.03\text{mm}$)

A plot showing the time varying density along with calculated densities obtained by ideal normal shock equations at a binned location $y = -5\text{mm}$ and $x=-0.03\text{mm}$ is shown in Figure 27. It is seen from the figure that the density profile is not a flat profile behind the reflected shock which is usually expected in large bore shock tubes. The density plot shown in Figure 27 indicates a rise in density after the shock reflection which is not an ideal behavior when compared to the density obtained via normal shock relations. However, it is known that the density depends on pressure and temperature as given by the ideal gas equation of state represented by Equation 14, where P , T are pressure and temperature and R is the specific gas constant for argon gas ($R = 208 \text{ J/Kg-K}$).

$$\rho = \frac{P}{RT} \quad (14)$$

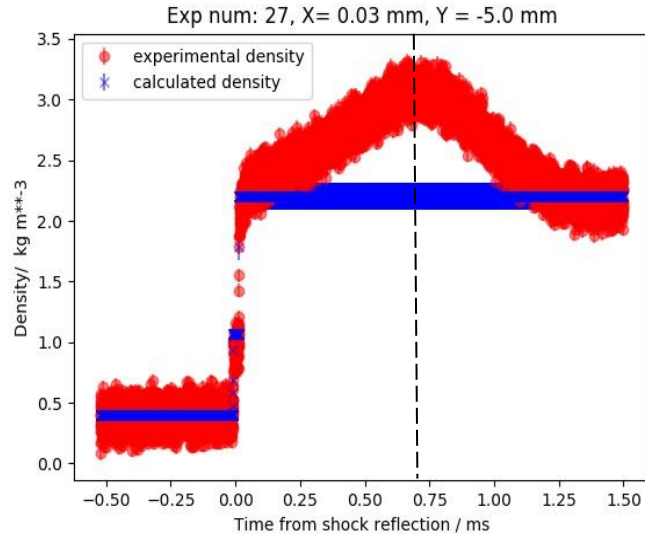


Figure 27. Experimental and calculated density for a binned experiment ($Y=-5\text{mm}$, $X=0.03\text{mm}$)

Therefore, a change in density can be related to a change in pressure and temperature conditions. The pressure during an experiment was measured by the endwall pressure transducer, which was placed at the center of the end wall section measuring the change in pressure at the end wall after the shock reflection. The endwall pressure profile for the same binned experiment ($y=-5\text{mm}$, $x=0.03\text{mm}$) is shown in Figure 28.

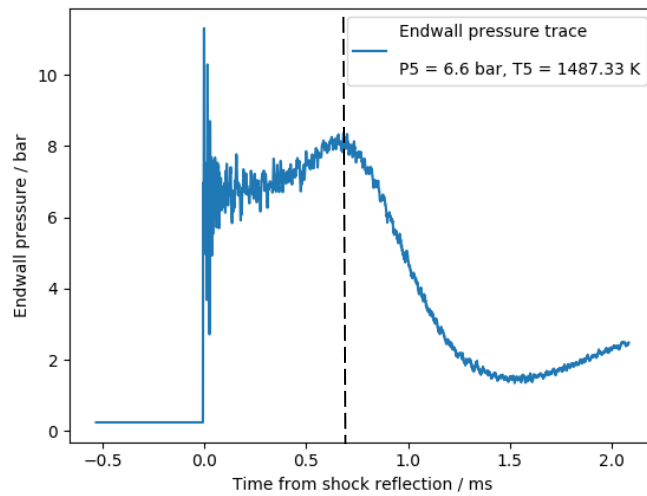


Figure 28. Endwall pressure trace for binned experiment at $Y=-5\text{mm}$, $X=0.03\text{mm}$

As seen from the figure, there is a significant increase in the pressure after the shock reflection from the end wall until $t=0.66\text{ms}$ before quenching similar to the trend seen in density profile, which is due to the magnified non-ideal effects in the miniature shock tube. The increase in pressure is evident as is the increase in density from the Figure 28. Since the pressure is changing which would mean that the temperature should also change unless there is an isothermal process existing behind the reflected shock region. However, due to the absence of temperature measurement, the increase in density suggests a complicated state history for temperature behind the reflected shock. Although the density and pressure show an increase as indicated by the above figures, it is important to notice that a density calculation by assuming a constant temperature behind the reflected shock would result in similar profile as the pressure trace with a difference in magnitude. However, this is not the case because the density profile has an immediate increase after the shock reflection and higher bump as compared to the pressure trace eliminating this assumption.

Hence, the deviation of the density profile shown in Figure 27 from the ideal flat nature is due to the presence of the non-ideal effects which is also seen in the previously discussed end wall pressure traces. The non-ideal nature of the density profile can be explained by putting forth two arguments. First, the reflected shock propagating away from the end wall into the incident shock region with the growing side wall boundary layers has the small perturbations (pressure waves) being transformed into large perturbations behind the reflected shock. This effect leads to higher pressure and temperature which directly leads to a higher density.

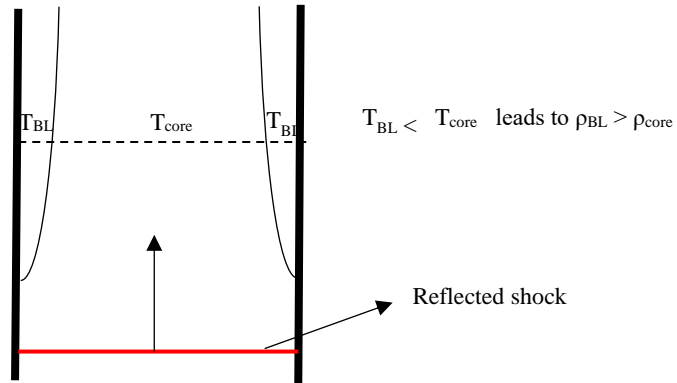


Figure 29. Temperature distribution across the length of the miniature shock tube (behind reflected shock region)

Second, the thermal boundary layer around the walls could also be a potential reason for the non-ideal behavior of the density profile. Specifically, even in the constant pressure conditions across a boundary layer, a growing fraction of the path length through the lower temperature boundary layer would lead to an increase in density with respect to time as the thermal boundary layer grows. It is important to realize that density measurement is path length averaged value and might not be homogeneous throughout. The Figure 29 shows the temperature distribution across the length of the miniature shock tube with the cold boundary layer temperature at the sides of the shock tube and the core gas temperature in the middle. Therefore, in constant pressure conditions using the Ideal Gas Equation of State, the density in the boundary layer region would be greater than the density in the core gas region and will vary as the path length through the boundary layer region is varied. This phenomenon would occur if there is cold side wall boundary layer growth leading to an increase in density.

The effectiveness of calibration of τ_{empty} is validated by comparing the initial or the pre-shock measured density value from Figure 27 with $\rho_1 = 0.4 \pm 0.01 \text{ kgm}^{-3}$ which is in excellent agreement with the calculated pre-shock density $\rho_{1, \text{calc}}$ from the shock tube metadata such as initial temperature (T_1), shock velocity (V_s) and other pre-shock conditions. It is an expected observation as this region is the one where the density is constant with time as the density is essentially a known quantity from the initial pressure and temperature of the shock tube. Following the pre-shock density, good agreement is seen in the incident shock region with $\rho_2 = 1.01 \pm 0.05 \text{ kgm}^{-3}$ but with increasing density with time from the passage of incident shock suggesting a growing boundary layer. The measured density immediately following the passage of the reflected shock region $\rho_{5, r} = 2.35 \pm 0.15 \text{ kgm}^{-3}$ is in good agreement with the calculated density only immediately after the passage of the reflected shock which increases until 0.66 ms because of the non-ideal effects such as cold boundary layer formation and then falls due to the refraction fan reaching the measurement location. The uncertainties in the densities are calculated by measuring the deviation from the average of measured and calculated density. The measured densities and their profiles are comparable to the measured pressure profiles in HRRST. The density profile presented here is the closest to the center of

the shock tube which has the least effect of boundary layer. As the measurement location shifts towards the extremities of the transverse locations, the density profile is different. This variation is primarily due to the shorter shock tube path length available at the extreme x locations and the boundary layer effect which will be described in the further section. The temporally resolved densities for different scans of experiments exhibiting the similar trend of density increase and decrease is shown in the Figure 30.

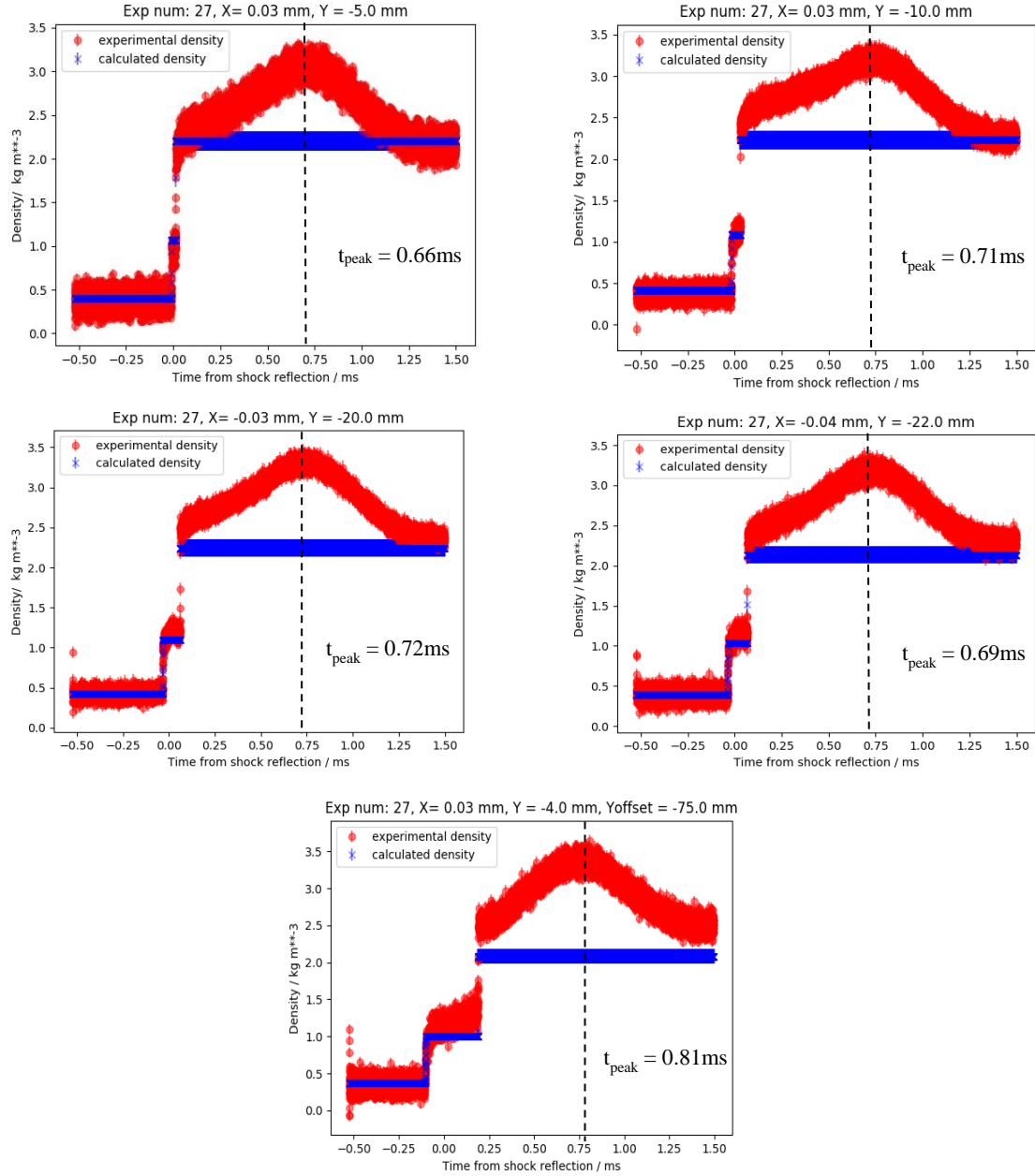


Figure 30. Temporally resolved density profiles associated with different scans of experiments ($Y=-5, -10, -20, -22, -79$ mm) with $P1 \approx 0.2505 \pm 0.01$ bar, $T1 \approx 27.5 \pm 0.3$ °C and $P5 \approx 6.58 \pm 0.12$ bar and $T5 \approx 1452.42 \pm 46$ K

4.1.1 Density variation with time after reflection from end wall at different Y locations

The time resolved density measurement was carried along various line-of-sight measurements which included measurement regions centered at various distances from the driven section endwall. The experiments performed at these measurement regions whose locations vary in y-direction gave the information on time-resolved density measurements and their variation as the measurement location is changed. However, several experiments were also conducted along various transverse x locations at each of these y locations to investigate the density variation with a change in shock tube path length whose details are mentioned in later sections. The density variation with time from the shock reflection are plotted for the various measurement regions whose distances from the driven section end wall are $y=-5, -10, -20, -22, -79, -94$ mm respectively. A plot showing the experimental densities incorporating a normalization factor which accounts for the differences in experimental conditions associated with different scans and whose transverse location varies from closest to farthest from the center of the axis of shock tube is shown in Figure 31.

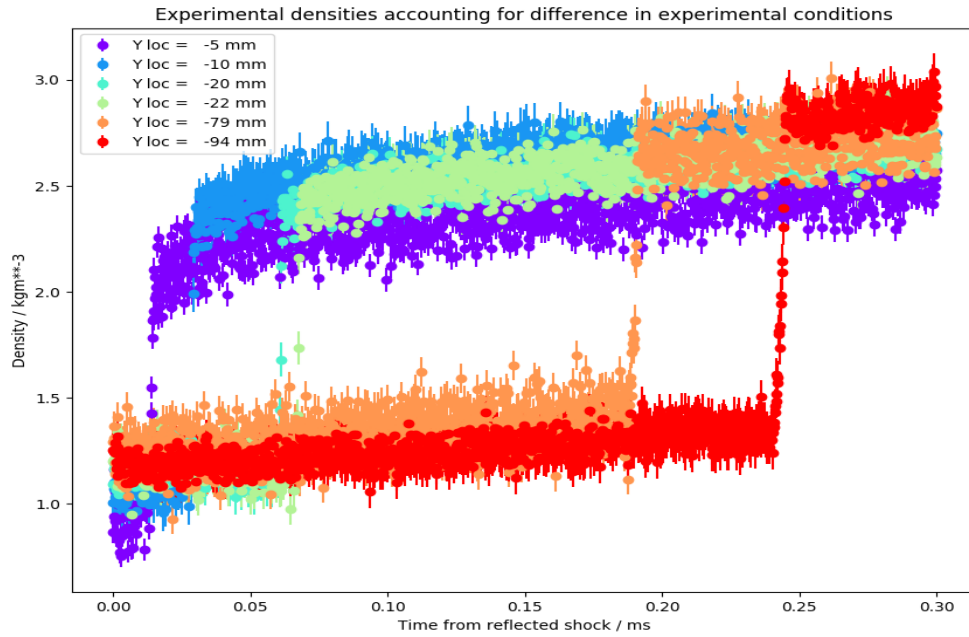


Figure 31. Density variation with time along with error bars from shock reflection at different y locations

As seen from the figure, the densities measured for the time from reflection from the end wall vary with time as the y location changes. The density profiles exhibit an expected behavior, where the reflected shock starting from the end wall takes less time to reach the measurement location closer to the end wall and more time to reach the farthest location from end wall. The density profile clearly shows the measured density ρ_5 increases with time where it has an immediate jump after $t_{\text{ref}} = 0.02\text{ms}$ at $y = -5\text{mm}$ location and has the sudden increase in density value at $t_{\text{ref}} = 0.24\text{ms}$ at the farthest y location which is $y = -94\text{mm}$. Also, the measured density profiles lie in the same range over all y locations and have the reflected shock density $\rho_5 = 2.2 \pm 0.104 \text{ kgm}^{-3}$. This is expected as the measured density at a transverse location closest to the center of the axis of the shock tube has the highest path length which means less noise and is least effected from the non-ideal effects such as the growing boundary layer. However, the densities calculated using normal shock relations and experimentally measured densities lie in an acceptable range where the pre-shock densities are respectively $\rho_{1(\text{calc})} \approx 0.4034 \pm 0.023 \text{ kgm}^{-3}$ and $\rho_{1(\text{exp})} \approx 0.3937 \pm 0.035 \text{ kgm}^{-3}$, behind the incident shock densities are $\rho_{2(\text{calc})} \approx 1.0617 \pm 0.056 \text{ kgm}^{-3}$ and $\rho_{2(\text{exp})} \approx 1.1275 \pm 0.20 \text{ kgm}^{-3}$ and the densities behind the reflected shock are $\rho_{5(\text{calc})} \approx 2.1667 \pm 0.104 \text{ kgm}^{-3}$ and $\rho_{5(\text{exp})} \approx 2.7411 \pm 0.580 \text{ kgm}^{-3}$ obtained by averaging the reflected shock density for 80% of the test time ($t \sim 0.6\text{ms}$). However, there is an excellent agreement between the calculated and measured ρ_1 with and percentage difference of 2.5% and a good agreement in the measured and calculated ρ_2 with a percentage difference of 6%. Whereas, the measured and calculated ρ_5 has a much large percentage difference of 28% and can be attributed to a combination of uncertainty in the measured quantities, absence of a perfect calibration and the non-ideal effects (boundary layer growth) causing the density to be much higher behind the reflected shock in the miniature shock tube. Also, a table showing the averaged calculated and measured pre-shock, behind the incident and reflected shock densities along with their uncertainties is presented in Table 6. The above described percentage difference between the densities rises an important question about the extent to which the uncertainty in the measuring equipment is contributing to this difference and how large the effect of the growing side wall

boundary layer is causing the incident and reflected shock densities to vary from the calculated densities using ideal normal shock relations.

Table 6. Average values of calculated and measured densities for different y locations, upper value = average density, lower value = uncertainty in density

Scan file	Y locations in mm	ρ_1 (calc) kg/m ³	ρ_1 (exp) kg/m ³	ρ_2 (calc) kg/m ³	ρ_2 (exp) kg/m ³	ρ_5 (calc) kg/m ³	ρ_5 (exp) kg/m ³
Scan_2390 Scan_2391	Y=-5	0.3944 0.0199	0.3694 0.1276	1.0449 0.0530	0.9092 0.1287	2.1568 0.1091	2.6007 0.1317
Scan_2382 Scan_2383	Y=-10	0.4151 0.0207	0.4067 0.1548	1.0891 0.0546	1.1031 0.1563	2.2365 0.1119	2.8241 0.1608
Scan_2387 Scan_2388	Y=-20	0.4223 0.0211	0.4165 0.1601	1.0925 0.0546	1.1709 0.1615	2.2265 0.1108	2.7978 0.1655
Scan_2389	Y=-22	0.3940 0.0196	0.3866 0.1625	1.0377 0.0517	1.0511 0.1638	2.1353 0.1061	2.5830 0.1674
Scan_2400	Y=-79	0.3789 0.0189	0.3582 0.1472	1.0055 0.0502	1.2351 0.1458	2.0781 0.1033	2.9001 0.1523
Scan_2401 Scan_2404	Y=-94	0.4154 0.0209	0.4245 0.0927	1.1002 0.0554	1.2953 0.0949	2.2707 0.1139	3.4360 0.1019

4.1.2 Density validation by end wall pressure transducer trace

The density profile obtained from X-ray densitometry experiments by using Beer's law showed a significant rise after the shock reflection from the endwall and would require validation. One way to accomplish this it to calculate density using the endwall pressure trace and incorporating this in the Ideal Gas Equation of State given by Equation 14.

However, the calculation of density from the end wall pressure trace requires the calculation of temperature over the period of shock propagation. However, most of the traditional shock tubes apply the principle of chemical thermometry to measure the temperature variation in the measurement region by using chemical thermometers[42,43]. Due to the absence of chemical thermometry and temperature measurement behind the reflected shock wave in this study, an alternate approach of calculating the temperature profile was implemented.

4.1.2.1 Temperature trace evaluation

The temperature behind the reflected shock region varying with time is denoted by temperature trace $T(t)$ and is calculated by using the isentropic assumption and the measured pressure trace. The derivative of the temperature can be given by

$$\frac{dT}{dt} = \frac{dP}{dt} \frac{T \bar{R}}{P \bar{c}_p(T)} \quad (15)$$

Where \bar{R} is the universal gas constant and $\bar{c}_p(T)$ is the constant pressure specific heat as a function of temperature determined by using the polynomials taken from the database of polynomials curated by Burcat and Ruscic. However, the constant pressure specific heat capacity remains as a constant with a value 520.27 J/Kg-K. The temperature estimation involves a time marching scheme with $\frac{dP}{dt}$ measured from the experimental data of end wall pressure trace and an estimate of $T(t=0)$ from normal shock equations. This method of deducing the temperature assumes the ideal gas equation of state and is marginally valid in HRRST [5] because of the 1) shorter test times and 2) the thermodynamic state is influenced by gas dynamic effects but not by chemical heat release. However, for the case of higher pressures the ideal gas equation would no longer hold good and the inclusion of real gas effects should be considered [42]. A temperature trace calculated for the binned experiment $x=0.03\text{mm}$ whose measurement location from the endwall is $y=-5\text{mm}$ is shown in the Figure 32 along with the corresponding pressure trace. However, the isentropic assumption is good enough to represent the temperature variation behind the reflected shock for low pressures and short reaction times similar to the conditions obtained in this study using the miniature HRRST.

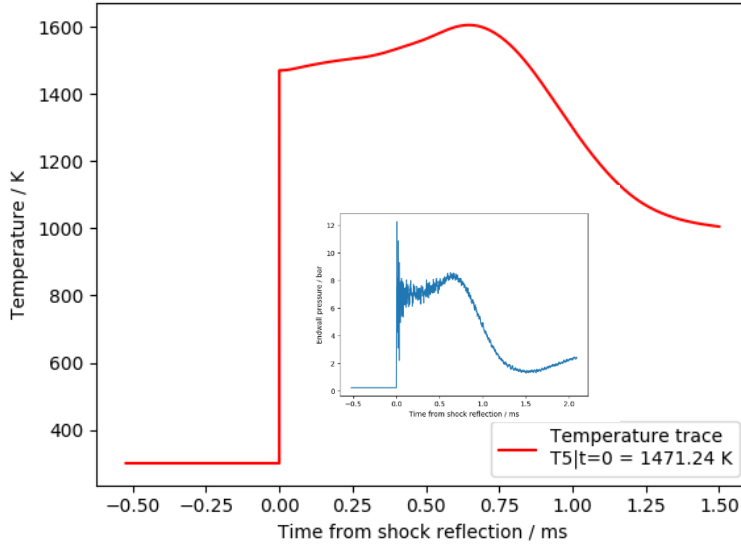


Figure 32. Temperature profile from end wall pressure trace for a binned experiment ($Y=-5\text{mm}$, $X=0.03\text{mm}$) with conditions $P1 = 0.2445\text{ bar}$, $T1 = 300.7\text{ K}$ and $P5 = 6.5\text{ bar}$, $T5 = 1463.49\text{ K}$

It is evident from the figure that the temperature behind the reflected shock wave rises after the shock reflection till time $t = 0.66\text{ms}$ which is the same time as in the previous profiles of end wall pressure trace and time varying density. The time marching temperature profile has the similar trend of increase and decrease as seen in the pressure profile which is due to the similar gradient as that of pressure trace but differing by a constant. Once the temperature trace is evaluated, it was simple to obtain the density estimate from the evaluated temperature and end wall pressure traces by using the Ideal Gas Equation of State given by Equation 14.

Density obtained using the Ideal Gas Equation should follow the isentropic behavior similar to the temperature trace and any deviation from this relates back to the complicated gas state history and was subjected to investigation. The deviation in the density profiles would suggest a non-isentropic behavior behind the reflected shock during the experiments. A profile showing the density obtained from the back calculation using the pressure and temperature traces along with the experimental density measured from the X-ray densitometry experiments is shown in Figure 33. The back calculated density profile is a smoothen profile obtained using a linear regression fitting function.

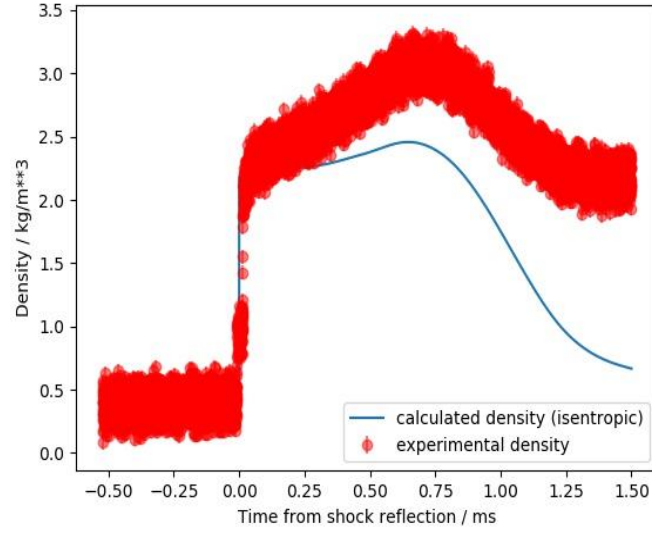


Figure 33. Experimental density and back calculated density for a binned experiment ($Y=-5\text{mm}$, $X=0.03\text{mm}$) with conditions $P1 = 0.2445\text{ bar}$, $T1 = 300.7\text{ K}$ and $P5 = 6.5\text{ bar}$, $T5 = 1463.49\text{ K}$

It is evident from the figure that the density calculated from the end wall pressure trace and the temperature trace is deviating from the experimental density obtained from the X-ray densitometry experiments. The calculated density has a less significant rise immediately after the shock reflection when compared to the experimental density indicating that the isentropic assumption does not hold true for interpreting the gas states behind the reflected shock in the miniature shock tube. This identification of non-ideal nature led to the possible explanation of presence of cold growing boundary layer as the reflected shock propagates back towards the driven section. Therefore, it becomes crucial to evaluate the boundary layer effect in the small-bore shock tube and the deviation from the theoretically calculated gas states using the ideal gas equations.

4.1.2.2 Boundary layer thickness calculation

For this purpose, a simple approach of calculating the boundary layer thickness by evaluating the temperature variation in the existing boundary layer was employed based on the concept adapted from Lifshitz et al. [3]. It is known that the partial derivative of pressure with respect to time and y location is non-zero as seen from the Figure 28. However, the partial derivative of pressure with respect to radius (r) is zero as there is no bulk velocity in this direction. Hence, this would suggest that, the density variation as

shown in Figure 27 and 33 is solely due to the temperature change because of the presence of cold side-wall boundary layer. The procedure for calculating the boundary layer thickness follows two simple steps 1) evaluating the temperature in the boundary layer region 2) estimating the boundary layer thickness using the calculated path length integrated density along the measurement location which is a function of boundary layer thickness denoted by ' χ '. However, the boundary layer model being built here based on Lifshitz's work which considers the thermal boundary layer to be pre-dominant over the viscous boundary layer. The assumptions that led to this selection criteria during the course of calculation were neglecting the effects of the viscous boundary layer [3] formed behind the incident shock as it propagates towards the test section because of the test time (0.66ms) of this study being higher than the time in which these effects prevail. The evaluation of temperature profile in the boundary layer region follows the similar procedure approached by [3]. procedure is implemented by first assuming the boundary layer gas of the miniature HRRST at the measurement location to be a semi-infinite layer where the wall temperature is taken to be the initial temperature T_i which is a constant (room temperature) simplifying the calculation.

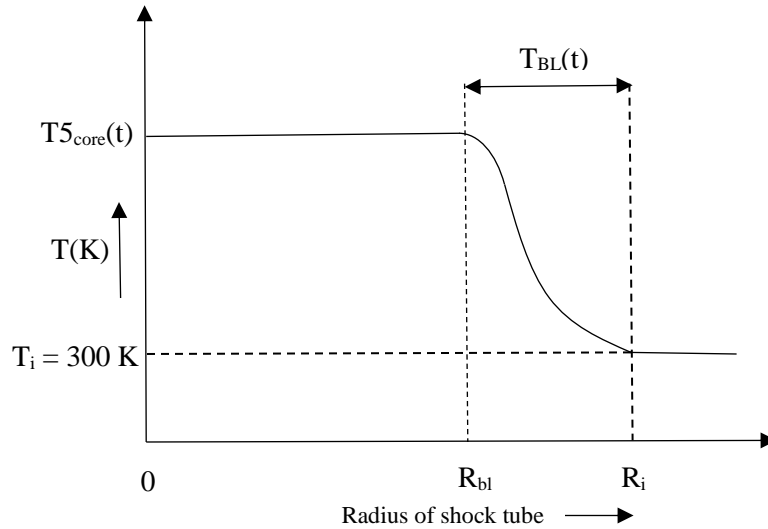


Figure 34. Temperature distribution along the line-of-sight (radius through symmetry) tube divided into core gas and boundary layer gas region

The temperature distribution along the line-of-sight measurement with center as the axis of the shock tube is shown in Figure 34. However, due to symmetry, the x axis of the plot is same as the radius of the shock

tube starting from the axis of the shock tube ($r=0$). As seen from the figure the temperature along the line of sight is divided into core gas temperature covering the distance from axis of shock tube to R_{BL} and a boundary layer temperature distributed from R_{BL} to R_i . The distance R_i is the radius of miniature HRRST and equal to 6.35mm and the boundary layer thickness is $R_i - R_{BL}$.

The procedure for obtaining the boundary layer equation involves a similar heat equation to that used by Lifshitz and is given by Equation 16. This equation on further simplification reduces to the classic ODE for transient heat conduction for a semi-infinite body with a constant wall temperature given by Equation 17. The temperature equation which is being calculated is assumed to start from the side wall of the shock tube (R_i) and progress all the way to the axis of the shock tube.

$$C_p \rho (\partial T / \partial t) = (\partial / \partial \chi) [k T (\partial T / \partial t)] \quad (16)$$

$$\frac{\partial^2 T}{\partial \eta^2} = -2\eta \frac{\partial T}{\partial \eta} \quad (17)$$

Where, T is the temperature, t is the time in seconds, k is the thermal conductivity and η which is a non-dimensional parameter called as similarity variable given by $\eta = \frac{\Psi}{2\sqrt{\frac{k \cdot p \cdot t}{C_p \cdot R}}}$ with $\Psi = \rho \chi$ as the path integrated density. Once the ODE is solved in terms of similarity variable, the solution for Equation 17 is given by Equation 18 along with constants to be evaluated.

$$T = c_1 * \int_0^\chi e^{-\eta^2} d\eta + c_2 \quad (18)$$

The c_1 and c_2 are the constants evaluated by using the boundary conditions stated as [$T(0, t) = T_1$ and $T(\eta \rightarrow \infty, t) = T5_core(t)$] in our case. The core gas temperature trace $T5_core(t)$ is the obtained from isentropic assumption as shown in Figure 32. The limits of the integration for Equation 18 are from zero to χ . However, it is well known that the thermal conductivity of a gas varies with temperature and as is the case with the test gas in the reaction zone. The temperature varies as time progresses and to incorporate this change, the equation for temperature dependent thermal conductivity of argon gas is taken from [44] and is given by Equation 19,

$$k = 4.25 * 10^{-5} * (T/300)^{0.66} \quad (19)$$

where T is absolute temperature. Using these boundary conditions, the constants were evaluated and resulted in the final equation for the boundary layer temperature varying as the distance ' χ ' from the side wall given by Equation 20

$$T(t) = T_1 + (T_{5(core)}(t) - T_1) * \operatorname{erf}\left(\frac{\rho * \chi}{2 * \sqrt{\frac{k * p * t}{Cp * R}}}\right) \quad (20)$$

The evaluated equation for boundary layer temperature as a function of time was evaluated for varying distance χ from the side wall. The way the boundary layer thickness was estimated in the study conducted by Lifshitz was by evaluating the location at which the boundary layer temperature reached 99% of the core gas temperature at different times for varying distance from the wall. Though adapting the method from previous work, the proposed method to obtain the boundary layer thickness is well agreed upon but would require this estimation of boundary layer thickness based on experimental data (density) obtained in this study.

Similar to Lifshitz's work, the different times selected for evaluation of boundary layer temperature are given as $t = 30, 300, 600, 900 \mu s$ for different y locations. The boundary layer thickness was determined by choosing the location where 99% of core gas temperature (T_5) was met by the boundary layer temperature. Figure 35 represents the boundary layer temperature calculated for different times along various y locations along with the red markers for $T_{99\%(core)}$. The profiles shown in the figure are similar to the profiles obtained by Lifshitz in his study with some variations in magnitude. The asymptotic nature of the curve decreases as the time progresses, which indicates a growing side wall boundary layer in the miniature shock tube. The similar trend is observed in all the y locations.

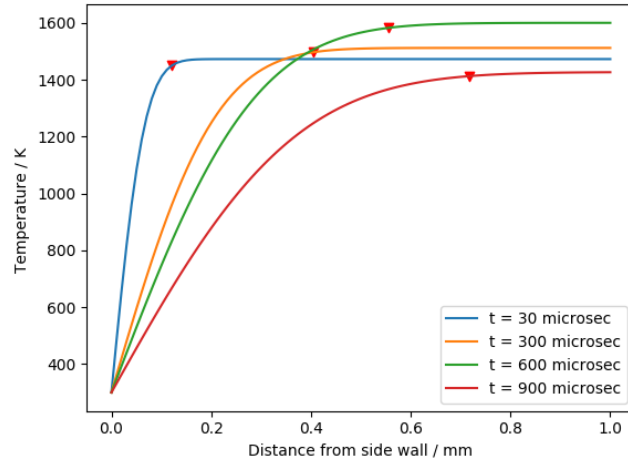


Figure 35. Comparison of boundary layer temperature profiles at different times $t=30, 300, 600, 900 \mu s$ using Equation 20 for $y = -5 \text{ mm}$ location

It can be seen from the figure that, the location at which the boundary layer temperature reaches the 99% of core gas temperature ($T_{99\%(\text{core})}$) increases as the time is increased. This increase suggests an evident increase in the boundary layer thickness as the time progresses. However, the profiles obtained for different times are similar to the profiles obtained by Lifshitz but with a deviation of intersecting profiles which is due to the changing pressure and core gas temperature with time. For instance, the boundary layer temperature profile for $y=-5\text{mm}$ for $30 \mu s$ has $T_{5(\text{core})} = 1472.86 \text{ K}$ and 1512 K for $300 \mu s$. The highest core gas temperature is for $t = 600 \mu s$ with $T_{5(\text{core})} = 1584 \text{ K}$. This difference in temperatures has direct consequence on boundary layer temperature profiles as seen from Equation 20 with the highest for $t = 600 \mu s$ in all profiles associated with different y locations. However, the boundary layer thickness considered as the location at which boundary layer temperature meets $T_{99\%(\text{core})}$ lies in the range of $\chi = 0.12 \pm 0.01 \text{ mm}$ for $t = 30 \mu s$ and reaches a maximum of $\chi = 0.7 \pm 0.04 \text{ mm}$ at $t = 900 \mu s$. It is also important to notice that, the boundary layer temperature profile at $t = 900 \mu s$ is lower than the rest of the profiles in magnitude because of the time t covers the 80% drop of the peak value.

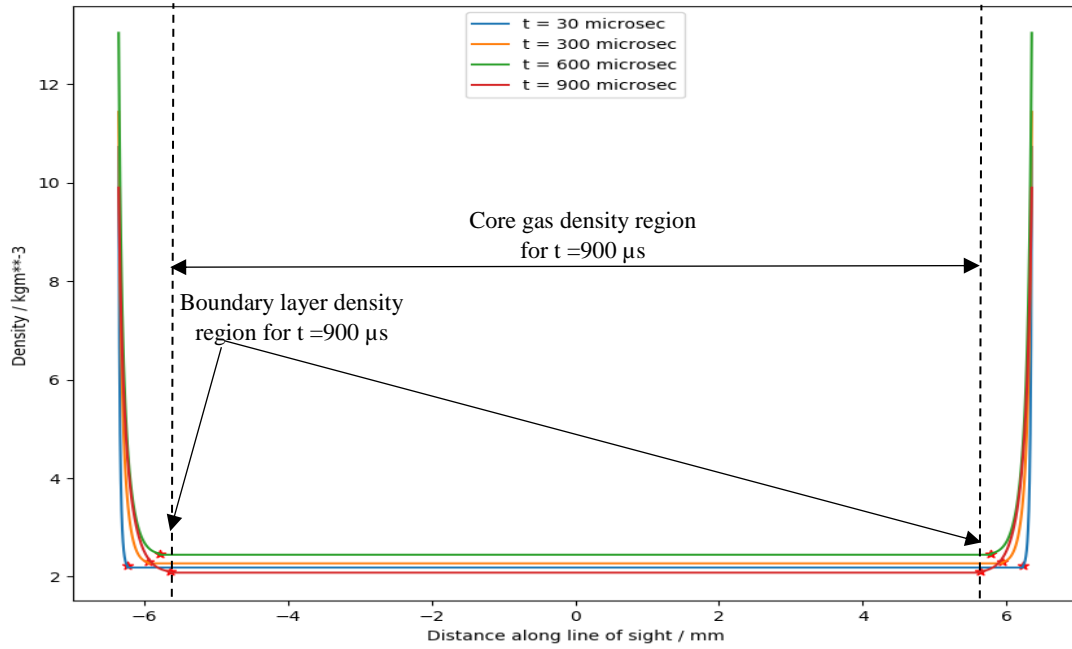


Figure 36. Density distribution along the line of sight divided into core gas and boundary layer density region separated by markers

The density distribution along the line of sight considered in calculating the boundary layer thickness is shown in Figure 36 which has the same left and right half of the profiles due to symmetry. It is evident that, the boundary layer region goes maximum to -5.63 mm on the negative side and +5.63 mm on the positive side which should be in a great agreement with the boundary layer thickness estimated from temperature profiles. This is because, the density calculated for the boundary layer region incorporates the boundary layer temperature Equation 20.

Using the Lifshitz's temperature equation the boundary layer thickness as a function of time was estimated by choosing the location at which the boundary layer temperature reached 99% of the core gas temperature. Using this boundary layer thickness, a corresponding path length integrated density was calculated and was compared to the experimental density. A plot showing the growing boundary layer thickness as a function of time and a resultant path length integrated density is shown in Figure 37.

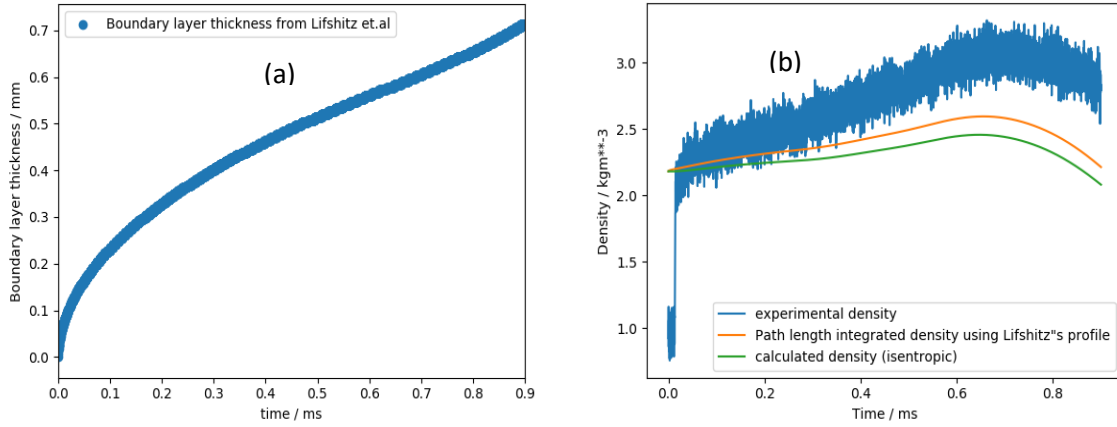


Figure 37. (a) Boundary layer thickness as a function time (b) Path length integrated density using the measured boundary layer thickness measured from Lifshitz's temperature profiles

The boundary layer thickness increases with time reaching $\chi = 0.7\text{mm}$ from the side wall of the shock tube at $t = 900\ \mu\text{s}$. The path length integrated density obtained by using this boundary layer thickness is not equal to the experimental density obtained suggesting a thicker boundary layer growth along the side wall.

Since the thermal boundary layer thickness estimated from these temperature profiles is based on the core gas temperature and pressure. It was desired to include the experimental data in determining the boundary layer thickness as a function of time and compare it to the thickness determined from temperature profiles.

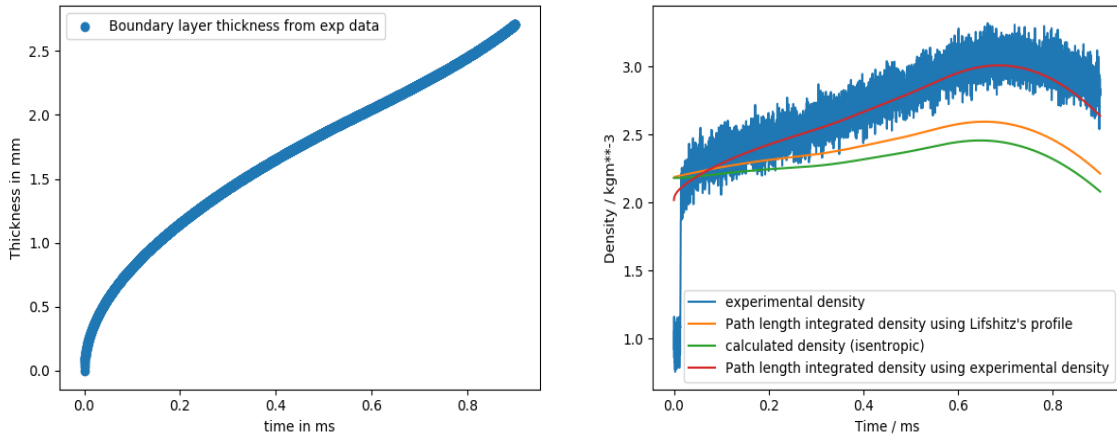


Figure 38. Boundary layer thickness calculated as a function of time at $y = -5\text{mm}$ using Equations 21 and 22 starting from $t=0$ to $900\ \mu\text{s}$

For this purpose, the thermal boundary layer thickness as a function of time was calculated using a path length integrated equation for density as shown in Figure 38 for $y=-5\text{mm}$ measurement location. The boundary layer thickness was calculated by adjusting the thickness χ to match the experimental density obtained by X-ray densitometry experiments. The above plot is obtained by using equations 21 and 22 which equates the path length integrated density to the experimental density as a time marching scheme.

$$\rho_{PL} = \frac{1}{R_i} \int_0^{R_i} \rho_{BL_new}(t, r) dr = \rho_{exp} \quad (21)$$

Where $\rho_{BL}(t)$ is given by

$$\rho_{BL_new}(t, r) = \frac{P_5(t)}{R * T_{(BL_new)}(t, r)} \quad (22)$$

The Equation 21 on piecewise separation results in

$$\rho_{exp} = \rho_{PL} = \rho_{core}(t) * \frac{R_{BL}}{R_i} + \rho_{BL}(t, \chi) * \frac{R_i - R_{BL}}{R_i} \quad (23)$$

where $T_{(BL)_new}(t, \chi)$ is given by

$$T_{(BL)_new}(t, \chi) = \left(T_1 + (T_{5(core)}(t) - T_1) * \operatorname{erf} \left(\frac{\rho * (\chi)}{10 * \sqrt{\frac{k * p * t}{Cp * R}}} \right) * e^{\left(\frac{-(t-0.043)^2}{12 * (0.04)^2} \right)} \right) \quad (24)$$

The new term in Equation 21 and 22 is the density in boundary layer region but with a modified temperature Equation which satisfies the conditions of 1) At R_{BL} , the density reaches 101% of core density and 2) The path length integrated density is equal to experimental density and $T_{(BL)_new}(t, \chi)$ is the modified Lifshitz's boundary layer temperature equation to satisfy the conditions mentioned above. The boundary layer thickness as a function of time is obtained by choosing the location at which $T_{(BL)_new}$ reaches the 99% of $T_{5(core)}$ which includes an adjusting parameter in terms of a modified function in χ and function in time 't' to match the $\rho_{exp}(t)$ at each time. The time for which the Equation 24 is iterated starts from $t=0$ to $900 \mu\text{s}$. This boundary layer thickness was calculated for all y locations using the same time marching

scheme, where the similar trend of an increase in boundary layer thickness was observed in almost all y locations with some uncertainty in them.

As seen from the Figure 38, the boundary layer thickness increases with time reaching the maximum thickness of 2.7 mm at $t = 900 \mu s$. The thickness measured from the temperature profiles and from equation 21-24 vary because of the inclusion of experimental density in calculation such that the boundary layer thickness is being adjusted to match this density as a function of time. This variation in the boundary layer thickness measurement from Lifshitz's temperature profiles and from experimental data can be shown as a plot given in Figure 39.

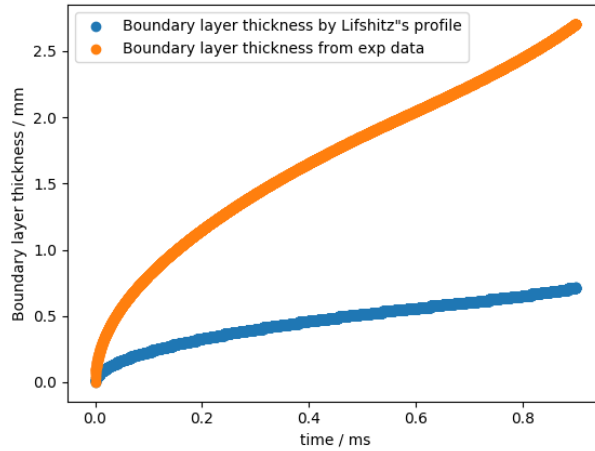


Figure 39. Comparison of boundary layer thickness as a function of time obtained from 1) Lifshitz's temperature profiles 2) Experimental density data

As seen from the figure, the profile for boundary layer thickness in the two cases has different profiles where the boundary layer thickness calculated from Lifshitz's temperature profile increases until 0.71 mm at $t = 0.9$ ms and the boundary layer thickness measured from experimental density increases until 2.7 mm at $t = 0.9$ ms. However, the thickness at the time $t_{\text{peak}} = 0.66$ ms is measured to be $\chi \approx 2.1$ mm for the case of thickness measured using experimental density and $\chi \approx 0.6$ mm in the case of thickness estimated by Lifshitz's temperature profiles. The difference in these respective boundary layer thicknesses is due to the incorporation of the adjustable parameter which is a combination of both thickness and time as given by

Equation 24 which constrains the path length integrated density to be equal to the experimental density. It can be inferred from the results obtained using the proposed model for thermal boundary layer thickness estimation that a faster growing boundary layer growth prevails behind the reflected shock. However, a much more detailed and further examination of these profiles considering other factors such as the mass flow rate and viscous boundary layer effects would give more insight on the boundary layer thickness variation with time, which is one of the aspect of future work.

4.2 Estimation of uncertainties in experimental and calculated densities

As previously discussed in modeling section, the calculation involved in obtaining the time resolved experimental density of the test gas using X-ray densitometry experiments is complicated. The procedure involves the use of formula given by Equation 11 where several measured parameters such as the incident and transmitted intensities, path length through the shock tube, τ_{empty} and the absorption coefficient having their own uncertainty are included. Since using an equation built on other measured parameters having their own uncertainty, the concept of error propagation analysis was used to calculate the final uncertainty in density. Using this approach led to the estimation of individual contribution by a specific measured parameter to the overall uncertainty. This gave an insight on how the most and least uncertain parameters affect the final uncertainty in the total measurement. The uncertainties in experimental and calculated densities were obtained using the error propagation concept whose procedure is detailed in the modeling section. The extensive formulation that goes into the calculation of uncertainty can be referred to the appendix. The uncertainty calculation begins with assigning the individual uncertainty in every parameter involved in calculation. However, recalling from Table 2, the calculation of experimental density involves 7 independent variables and the calculated density involves 3 independent variables. The more number of independent parameters in experimental density would suggest more complicated equations involved as compared to the calculated density. The uncertainty in the independent parameters for calculated density are constant throughout the different scans of experiments with a changing uncertainty in initial pressure P_1 as it is different for different scans of experiments.

It was chosen that, the uncertainty in initial temperature T_1 was about 0.5°C and shock Mach number M_s is constant with a value of 0.002 throughout the scans of experiments with a varying uncertainty in initial pressure P_1 as this pressure is different for different scans of experiments. The uncertainty in P_1 was chosen to be 5% of the initial pressure throughout all scans of experiments. In addition to this the uncertainty in the independent parameters associated with the experimental density are listed in Table 7 for the binned experiments.

Table 7. Uncertainty in individual parameters for experimental density at different scans of experiments

Scan file	Y locations in mm	σ_{I1}	$\sigma_{I1(\text{dark})}$	σ_{I0}	$\sigma_{I0(\text{dark})}$	$\sigma_{\tau_{\text{empty}}}$	σ_{PL}	$\sigma_{\text{sigma_9kev}}$
Scan_2390 Scan_2391	Y=-5	0.0340	0.0030	0.0326	0.0005	0.055	6.81E-05	0.104
Scan_2382 Scan_2383	Y=-10	0.0417	0.0030	0.0408	0.0005	0.056	7.13E-05	0.104
Scan_2387 Scan_2388	Y=-20	0.0369	0.0030	0.0373	0.0005	0.055	7.20E-05	0.104
Scan_2389	Y=-22	0.0357	0.0030	0.0355	0.0005	0.055	7.26E-05	0.104
Scan_2400	Y=-79	0.0344	0.0030	0.0293	0.0005	0.056	7.13E-05	0.104

The uncertainty analysis was performed using the equations mentioned in the appendix and resulted in uncertainty in the experimental and calculated pre-shock, behind the incident and behind the reflected shock densities for each experiment associated with the different scans. The assumptions for the uncertainty associated with the individual parameters are also mentioned in the Appendix A. Using these uncertainties associated with parameters to obtain experimental density as listed in Table 7 and the parameters for calculated densities, the final uncertainty in the experimental and calculated density is obtained. The values from the table indicate that the maximum uncertainty is caused by the uncertainty in τ_{empty} which varies from 0.05 to 0.058. The next highest uncertainty is associated with the transmitted intensity (I_1) and incident intensity (I_0). The least contributing uncertainty is by the path length through the shock tube as compared to the other uncertainty bearing parameters. The contribution from the independent parameters to the final

variance of uncertainty in density can be evaluated by multiplying the square of the uncertainty in independent parameters with the square of the partial derivative of density with respect to the independent variable. The values for these contributions are computed for the pre-shock, behind the incident shock and behind the reflected shock region. First, the contribution by each independent parameter for the pre-shock region is listed in Table 8 along with the percentage contributions for the experimental density at binned experiments.

Table 8. Contributions of individual parameters to the final variance of uncertainty in experimental density in pre-shock conditions, Upper value = Contribution value, Lower value = % contribution

Scan file	Y locations in mm	$\left(\frac{\partial \rho_{exp}}{\partial I_1} \sigma_{I_1}\right)^2$	$\left(\frac{\partial \rho_{exp}}{\partial I_{1(dark)}} \sigma_{I_{1(dark)}}\right)^2$	$\left(\frac{\partial \rho_{exp}}{\partial I_0} \sigma_{I_0}\right)^2$	$\left(\frac{\partial \rho_{exp}}{\partial I_{0(dark)}} \sigma_{I_{0(dark)}}\right)^2$	$\left(\frac{\partial \rho_{exp}}{\partial \tau_{empty}} \sigma_{\tau_{empty}}\right)^2$	$\left(\frac{\partial \rho_{exp}}{\partial P_L} \sigma_{P_L}\right)^2$	$\left(\frac{\partial \rho_{exp}}{\partial \sigma_{9keV}} \sigma_{\sigma_{9keV}}\right)^2$
Scan_2390 Scan_2391	Y=-5	0.0308 0.88	2.91E-05 8.35E-03	0.0029 0.82	5.92E-07 1.7E-04	0.3425 98.275	8.37E-06 2.4E-03	2.45E-05 7.03E-03
Scan_2382 Scan_2383	Y=-10	0.0068 1.44	5.37E-05 1.14E-02	0.0105 2.22	1.12E-06 2.37E-04	0.4544 96.32	1.32E-05 2.81E-03	2.61E-05 5.53E-03
Scan_2387 Scan_2388	Y=-20	0.0835 1.61	6.82E-05 1.32E-02	0.0127 2.45	1.42E-06 2.75E-04	0.4967 95.91	1.74E-05 3.35E-03	2.77E-05 5.53E-03
Scan_2389	Y=-22	0.0116 2	7.77E-05 1.34E-02	0.0157 2.71	1.63E-06 2.81E-04	0.551 95.25	1.67E-05 2.88E-03	2.48E-05 4.29E-03
Scan_2400	Y=-79	0.0088 1.87	7.16E-05 1.53E-02	0.0062 1.32	1.48E-06 3.17E-04	0.4357 96.77	1.50E-05 3.2E-03	2.27E-05 4.84E-03

The information provided in the table indicates that, the major contribution to the final uncertainty in pre-shock density (ρ_1) is from τ_{empty} with almost greater than 90% in all scans of experiments suggesting extra care has to be taken while calibrating the empty and pre-shock data. Also, the next highest percentage contributions are from incident and transmitted intensities ranging from 0.8~3.0% throughout the different scans of experiments. The contribution of each independent parameter is calculated to be a product of square of the partial derivative of density with respect to the parameter and square of uncertainty in that respective parameter. These percentages are calculated considering the average of variance in final uncertainties which are different from the final uncertainties in densities.

A similar representation of the contributions for the incident shock region can be given by Table 9 along with the percentage contributions to the averaged variance of final uncertainty in ρ_2 . The below table shows the similar trend of maximum contribution to the uncertainty in ρ_2 by τ_{empty} falling in the range of 95-98.5% covering all scans of experiments. The next highest contributions are from incident and transmitted intensities ranging from 0.8-2.5 % spread over all scans of experiments. However, it is important to notice that the contributions from the independent parameters are more when compared to pre-shock region.

Table 9. Contributions of individual parameters to the final variance of uncertainty in experimental density behind incident shock conditions, Upper value = Contribution value, Lower value = % contribution

Scan file	Y locations in mm	$\left(\frac{\partial \rho_{exp}}{\partial I_1} \sigma_{I_1}\right)^2$	$\left(\frac{\partial \rho_{exp}}{\partial I_{1(dark)}} \sigma_{I_{1(dark)}}\right)^2$	$\left(\frac{\partial \rho_{exp}}{\partial I_0} \sigma_{I_0}\right)^2$	$\left(\frac{\partial \rho_{exp}}{\partial I_{0(dark)}} \sigma_{I_{0(dark)}}\right)^2$	$\left(\frac{\partial \rho_{exp}}{\partial \tau_{empty}} \sigma_{\tau_{empty}}\right)^2$	$\left(\frac{\partial \rho_{exp}}{\partial P_L} \sigma_{P_L}\right)^2$	$\left(\frac{\partial \rho_{exp}}{\partial \sigma_{9keV}} \sigma_{\sigma_{9keV}}\right)^2$
Scan_2390 Scan_2391	Y=-5	0.0034 0.98	3.19E-05 9.15E-03	0.0029 0.82	5.92E-07 1.7E-04	0.3425 98.14	3.99E-05 1.14E-02	0.0001 0.04
Scan_2382 Scan_2383	Y=-10	0.0074 1.56	5.81E-05 1.23E-02	0.0105 2.22	1.12E-06 2.36E-04	0.4544 96.16	8.36E-05 1.77E-02	0.0002 0.031
Scan_2387 Scan_2388	Y=-20	0.009 1.74	7.36E-05 1.42E-02	0.0127 2.45	1.42E-06 2.75E-04	0.4967 95.74	0.0001 2.14E-02	0.0002 0.031
Scan_2389	Y=-22	0.0124 2.15	8.34E-05 1.44E-02	0.0156 2.71	1.63E-06 2.81E-04	0.551 95.09	0.0001 1.87E-02	0.00014 0.025
Scan_2400	Y=-79	0.0096 2.05	7.82E-05 1.67E-02	0.0061 1.31	1.48E-06 3.16E-04	0.4357 96.56	9.74E-05 2.07E-02	0.0002 0.034

This increase is because of lower values for transmitted and incident intensities in incident shock region which directly leads to higher values for contributions as these equations involve transmitted and incident intensities in the denominator. Finally, the contributions from the independent parameters to the final uncertainty behind the reflected shock density ρ_5 are tabulated in Table 10 along with the percentages.

It is evident that, the percentage contributions follow the same trend as mentioned for pre-shock and incident shock where contribution from τ_{empty} is the highest followed by incident and transmitted intensities. An increase in the contributions is observed when compared to pre-shock and incident shock

calculations. This increase is attributed to the fact that the transmitted intensity goes down in the region behind the reflected shock which results in higher uncertainty value as these intensities are placed in the denominator. However, these contributions are calculated for the averaged variance of total uncertainty in pre-shock, behind the incident and behind the reflected shock region, which are different from the total uncertainty listed in Table 6. However, the final uncertainty in the pre-shock, behind the incident and behind the reflected shock are calculated using the equations presented in Appendix and the same are plotted for all scans of experiments.

Table 10. Contributions of individual parameters to the final variance of uncertainty in experimental density behind reflected shock conditions, Upper value = Contribution value, Lower value = % contribution

Scan file	Y locations in mm	$\left(\frac{\partial \rho_{exp}}{\partial I_1} \sigma_{I_1}\right)^2$	$\left(\frac{\partial \rho_{exp}}{\partial I_{1(dark)}} \sigma_{I_{1(dark)}}\right)^2$	$\left(\frac{\partial \rho_{exp}}{\partial I_0} \sigma_{I_0}\right)^2$	$\left(\frac{\partial \rho_{exp}}{\partial I_{0(dark)}} \sigma_{I_{0(dark)}}\right)^2$	$\left(\frac{\partial \rho_{exp}}{\partial \tau_{empty}} \sigma_{\tau_{empty}}\right)^2$	$\left(\frac{\partial \rho_{exp}}{\partial PL} \sigma_{PL}\right)^2$	$\left(\frac{\partial \rho_{exp}}{\partial \sigma_{9keV}} \sigma_{\sigma_{9keV}}\right)^2$
Scan_2390 Scan_2391	Y=-5	0.0042 1.22	3.92E-05 1.12E-02	0.0029 0.82	5.91E-07 1.69E-04	0.3425 97.71	0.0002 0.05	0.0007 0.193
Scan_2382 Scan_2383	Y=-10	0.0090 1.89	6.87E-05 1.44E-02	0.0105 2.20	1.12E-06 2.35E-04	0.4544 95.61	0.0004 0.09	0.0009 0.191
Scan_2387 Scan_2388	Y=-20	0.0109 2.08	8.81E-05 1.69E-02	0.0127 2.43	1.42E-06 2.73E-04	0.4967 95.16	0.0007 0.12	0.0010 0.185
Scan_2389	Y=-22	0.0143 2.46	9.79E-05 1.68E-02	0.0157 2.7	1.63E-06 2.79E-04	0.551 94.56	0.0006 0.098	0.0009 0.148
Scan_2400	Y=-79	0.0116 2.44	9.39E-05 1.99E-02	0.0062 1.30	1.48E-06 3.14E-04	0.4357 95.93	0.0005 0.097	0.0010 0.21

A plot showing the uncertainties for individual experiments for the scans 2390 and 2391 whose measurement region is y=-5mm is shown in the Figure 40 for both experimental and calculated densities. The uncertainties in calculated densities are represented by squares and the uncertainties in experimental densities are represented by upward triangles. The uncertainties are represented by the higher and lower values for both the calculated and experimental densities as marked in the figure.

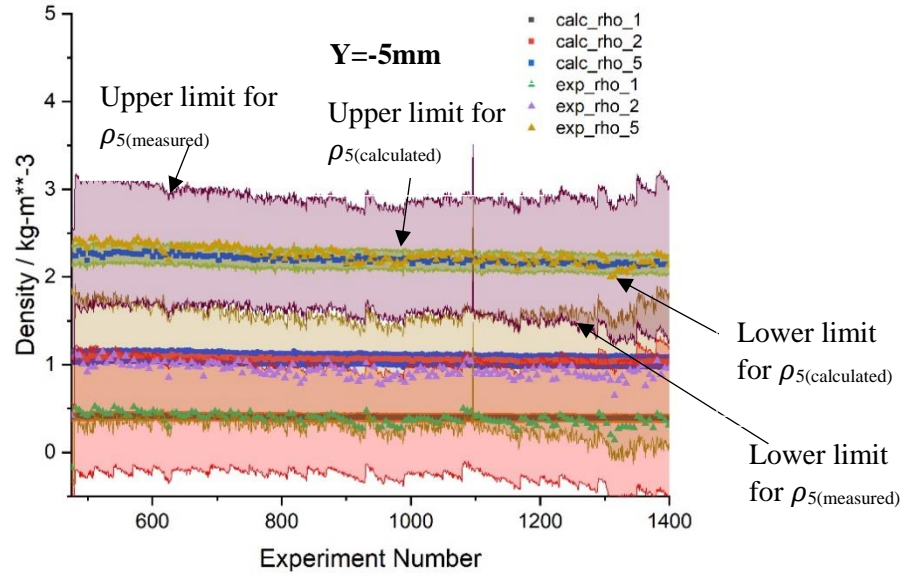


Figure 40. Uncertainties for calculated and experimental densities represented as error bars for individual experiments ($Y=-5\text{mm}$)

The above figure shows the uncertainties for both the calculated and measured densities segregated into ρ_1 , ρ_2 and ρ_5 where the uncertainty in the experimental density is the one with a wider gap between the upper and lower limit of the error bar. Whereas, the uncertainty associated with the calculated density is the one with narrow gap between the upper and lower limit of the uncertainty as denoted in the figure for $\rho_5(\text{calculated})$. However, the uncertainties were also calculated for the binned experiments leading to a better interpretation due to the reduction of noise. The averaged absolute uncertainties for experimental ρ_1 , ρ_2 and ρ_5 are given by $\sigma_{\rho_1(\text{experimental})} = 0.6591 \text{ kgm}^{-3}$, $\sigma_{\rho_2(\text{experimental})} = 0.6653 \text{ kgm}^{-3}$ and $\sigma_{\rho_5(\text{experimental})} = 0.6833 \text{ kgm}^{-3}$. Similarly, the averaged absolute uncertainties in the calculated densities are $\sigma_{\rho_1(\text{calculated})} = 0.02 \text{ kgm}^{-3}$, $\sigma_{\rho_2(\text{calculated})} = 0.0532 \text{ kgm}^{-3}$ and $\sigma_{\rho_5(\text{calculated})} = 0.1096 \text{ kgm}^{-3}$. It is evident that, the highest absolute uncertainty is in case of the density behind the reflected shock ρ_5 both in experimental and calculated densities with the $\sigma_{\rho_5(\text{experimental})}$ being 0.6391 kgm^{-3} more than the $\sigma_{\rho_5(\text{calculated})}$ whereas the uncertainty in $\rho_2(\text{experimental})$ is 0.6121 kgm^{-3} more than the $\sigma_{\rho_2(\text{calculated})}$. This large difference is attributed to the more uncertain parameters such as τ_{empty} and incident and transmitted intensities involved in obtaining the experimental density. The explanation to this

higher uncertainty in experimental density compared to calculated density can be referred to the Table 7 which lists the averaged uncertainties in individual parameters considered in the calculation.

However, the uncertainties mentioned above are relatively higher for the density measured and the reason for this is because of the individual scatter in each of the experiments. Therefore, the plots for uncertainties with less noise was obtained by performing the uncertainty analysis for the binned experiments. For this purpose, a plot for the uncertainty in densities for the binned experiments associated with the scan 2390 and 2391 is shown in Figure 41. The uncertainty calculation for the calculated and experimental densities involve the overall averaged values to obtain the final uncertainty.

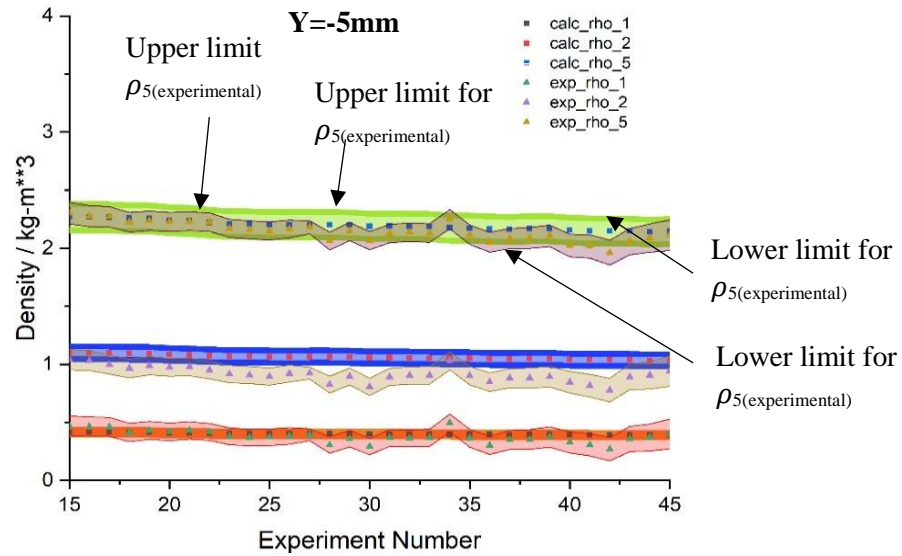


Figure 41. Uncertainty measurement in calculated and experimental densities for binned experiments ($Y=-5mm$)

As seen from the figure, the uncertainties calculated for the binned experiments have small error bars with a narrow gap between the upper and lower limits of the uncertainty. This narrow range of the uncertainty is due to the averaging performed on the experimental parameters as well as the measured densities. The uncertainty in the experimental density is given by $\sigma_{\rho 1(\text{experimental})} = 0.0891 \text{ kgm}^{-3}$, $\sigma_{\rho 2(\text{experimental})} = 0.0908 \text{ kgm}^{-3}$ which is 79.8% less than the one obtained in individual experimental case and $\sigma_{\rho 5(\text{experimental})} =$

0.095kgm⁻³ which is 80.1% less than the individual experimental case. This represents the advantage in performing the binning method leading to a less scatter in the data which is essentially due to the division of uncertainty by square root of number of experiments present in the bin.

Similarly, the uncertainty analysis was performed for the rest of the scans of experiments at different y locations and the corresponding averaged uncertainties associated with individual and binned experiments are tabulated in Table 11 for calculated density.

Table 11. Uncertainties in calculated densities for individual and binned experiments for different scans. Upper value- individual, lower value- binned

Scan file	Y locations in mm	$\rho_{1(calc)}$ (kg/m ³)	$\sigma_{\rho 1(calc)}$ (kg/m ³)	$\rho_{2(calc)}$ (kg/m ³)	$\sigma_{\rho 2(calc)}$ (kg/m ³)	$\rho_{5(calc)}$ (kg/m ³)	$\sigma_{\rho 5(calc)}$ (kg/m ³)
Scan_2390 Scan_2391	Y=-5	0.3944	0.0200	1.0449	0.0532	2.1568	0.1096
			0.0199		0.0530		0.1091
Scan_2382 Scan_2383	Y=-10	0.4151	0.0208	1.0891	0.0547	2.2365	0.1121
			0.0208		0.0547		0.1120
Scan_2387 Scan_2388	Y=-20	0.4223	0.0211	1.0925	0.0547	2.2265	0.1109
			0.0211		0.0546		0.1108
Scan_2389	Y=-22	0.3940	0.0197	1.0377	0.0518	2.1353	0.1061
			0.0197		0.0518		0.1061
Scan_2400	Y=-79	0.3789	0.0187	1.0055	0.049	2.0781	0.1
			0.0190		0.0502		0.1033

The above table shows that the uncertainties calculated for individual and binned experiments lie in similar range with minimum variation as these are constant values obtained by using ideal normal shock relations. However, the uncertainty increases from pre-shock density $\rho_{1(calc)}$ to behind the reflected shock density $\rho_{5(calc)}$ because of the increase in complexity of density dependence on initial pressure and temperature. Also, the averaged uncertainties associated with individual and binned experiments for experimental density are tabulated in Table 12 along with nominal experimental density.

Table 12. Uncertainties in experimental densities for individual and binned experiments for different scans. Upper value- individual, lower value- binned

Scan file	Y location s in mm	$\rho_{1(exp)}$ (kg/m ³)	$\sigma_{\rho 1(exp)}$ (kg/m ³)	$\rho_{2(exp)}$ (kg/m ³)	$\sigma_{\rho 2(exp)}$ (kg/m ³)	$\rho_{5(exp)}$ (kg/m ³)	$\sigma_{\rho 5(exp)}$ (kg/m ³)
Scan_2390 Scan_2391	Y=-5	0.3694	0.6591 0.1276	0.9092	0.6653 0.1287	2.6007	0.6833 0.1317
Scan_2382 Scan_2383	Y=-10	0.4067	0.7898 0.1548	1.1031	0.7979 0.1563	2.8241	0.8246 0.1608
Scan_2387 Scan_2388	Y=-20	0.4165	0.7851 0.1601	1.1709	0.7926 0.1615	2.7978	0.8155 0.1655
Scan_2389	Y=-22	0.3866	0.4773 0.1625	1.0511	0.4890 0.1638	2.5830	0.5227 0.1674
Scan_2400	Y=-79	0.3582	0.8462 0.1472	1.2351	0.8518 0.1458	2.9001	0.8740 0.1523

The above table shows that the uncertainty in the pre-shock, behind the incident and behind the reflected shock density are close to each other with a difference of $\sim 0.01 \text{ kg/m}^3$ between $\rho_{1(exp)}$ and $\rho_{2(exp)}$ and $\sim 0.04 \text{ kg/m}^3$ between $\rho_{1(exp)}$ and $\rho_{5(exp)}$ in almost all scans of experiments. A comparison of Tables 11 and 12 leads to an important observation of the uncertainties in the experimental densities being larger than the uncertainties in calculated densities. This deviation in the densities can be justified by referring to the Table 7 which shows comparatively large number of uncertainty carrying parameters (maximum in τ_{empty} , incident and transmitted intensities) in experimental density calculation. In addition to this, the highly uncertain parameters such as transmitted intensities and τ_{empty} are only associated with experimental density whereas the calculated density has low number of uncertain parameters with corresponding low uncertainties. The uncertainties for individual experiments associated with different scans of experiments are also shown in the Figure 42 along with the calculated and experimental densities. The uncertainty is represented with error bars having the upper and lower limit as the calculated uncertainty.

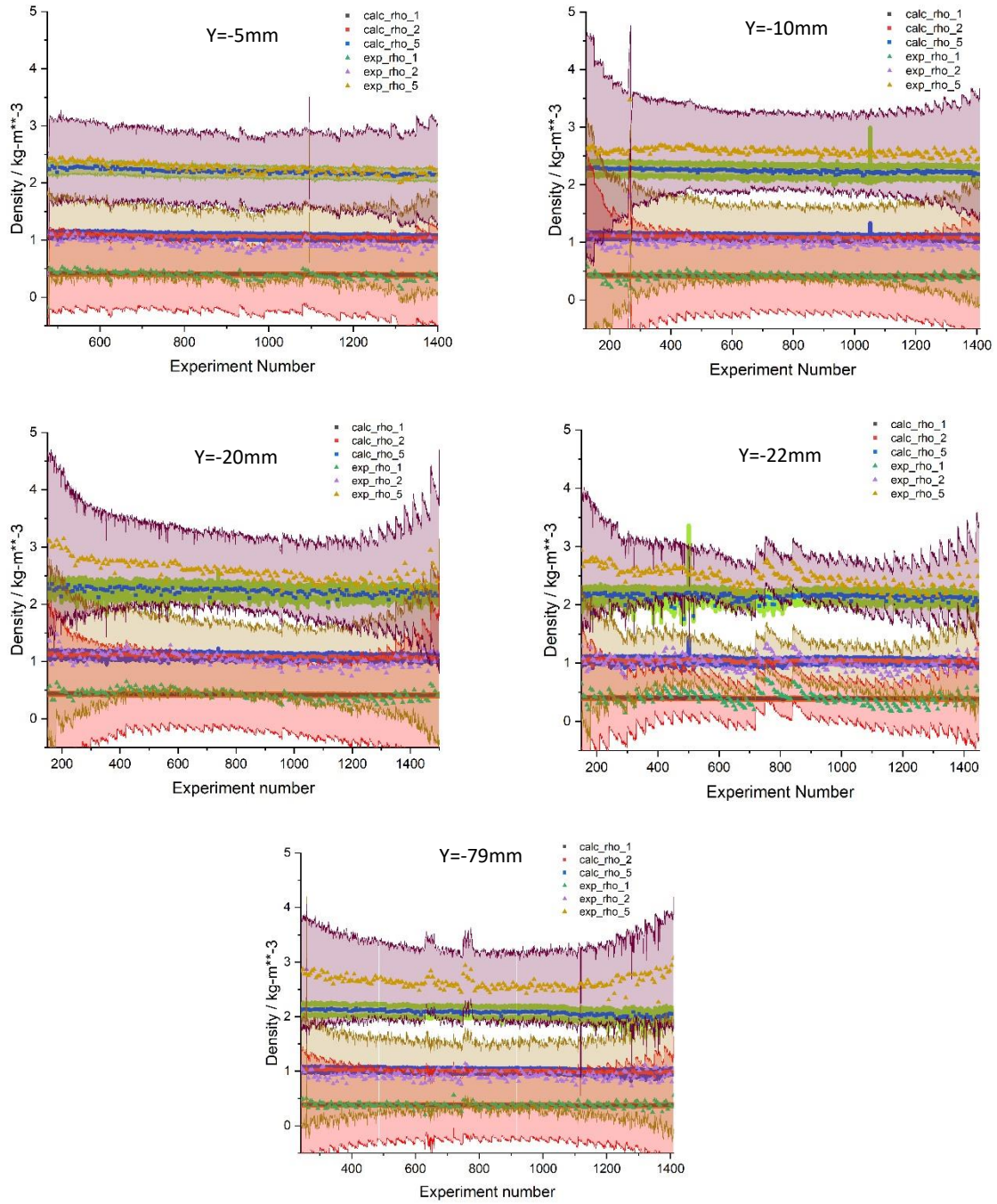


Figure 42. Uncertainties for individual experiments associated with different scans with different y locations

The uncertainties shown in the Figure 42 show a relatively flat and narrow band of uncertainties from experiments 450 to 1200. These experiments have the transverse location 'x' ranging from -3.25 mm to +3.25 mm. As previously discussed, the path length through the shock tube increases from the centermost

transverse location i.e. $x \sim 0$ mm to extreme transverse location leading to small amount of uncertainty in τ_{empty} and the transmitted intensities at these locations. However, as the extreme locations were approached the path length through the shock tube decreased and the path length to be traversed through the polycarbonate wall thickness increased leading to large uncertainty in τ_{empty} and transmitted intensities. Therefore, as uncertainties in transmitted intensities and τ_{empty} have the largest contributions to uncertainty in experimental density, an increase of uncertainty in these parameters would increase the range of uncertainty in the initial and final experiments as seen from Figure 42. The experiments at the start and the end are associated with the extreme transverse x locations and as mentioned larger uncertainty is observed.

4.3 Time varying density along transverse ‘x’ locations

Experiments conducted in this study involved various measurement locations which including various transverse x locations for every y location shown in Figure 14. Thirty experiments were conducted at each transverse x location allowing the use of binning. Transverse locations were separated by 0.25 mm covering the total bore of the shock tube with $x \approx 0$ mm being the center most location and $x \approx -6.25$ and $+6.25$ mm being the positive and negative extremes. The time varying density along all transverse x locations which covers the bore of the shock tube can be shown as a wireframe plot given by Figure 43. As shown by the figure, the 3-d plot for density variation with time and x location has noise associated with it. The noise in the density value becomes much larger at the extreme locations due to the shorter path lengths through the shock tube. However, the goal was to obtain the radially resolved density, and therefore leading to measurement of the boundary layer in the miniature shock tube. For this purpose, the analysis of temporally resolved density along transverse locations was important as the method to obtain radially resolved profiles uses the density variation with transverse x locations. The density profiles starting from $x=0$ to both extremes of $x = -6.35$ mm and $x = +6.35$ mm are similar in shape and magnitude due to the symmetry.

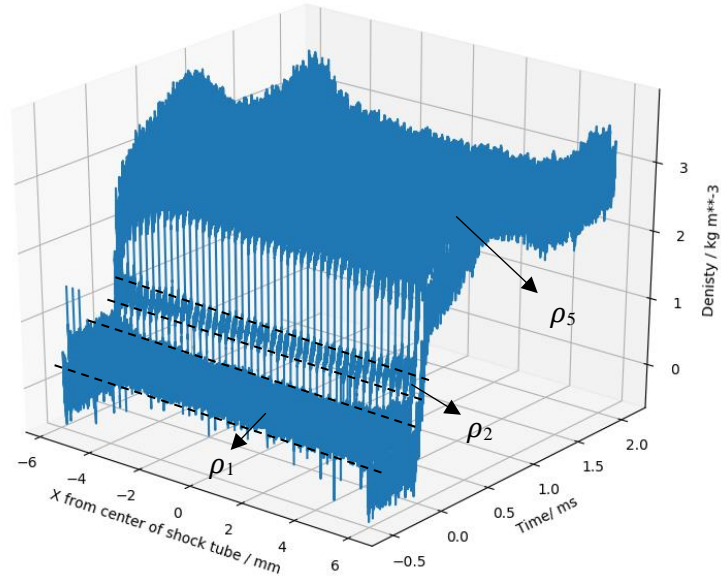


Figure 43. Density variation with time and x locations ranging from -6.25 to +6.25 mm

Time varying densities were obtained at these transverse locations. The densities obtained at various x locations can be analyzed by using the averaging of ensemble averaged data starting from the time of shock reflection from the driven section end wall which is the region of interest as there is a significant increase in density as opposed to the ideal normal shock behavior.

However, the plot shown in Figure 43 does not help in analyzing the density variation with respect to x location. This variation in density along transverse x locations can be analyzed by measuring the density change at different times. Therefore, the density variation behind the reflected shock with respect to different transverse x locations in 2D for better interpretation was accomplished by averaging the binned experimental density of unique bins for a period of 60 μ s over 20 consecutive intervals spreading up to twice the reaction time. For the sake of simplicity, the analysis shown here is attributed to a single measurement region whose distance from the end wall is 5mm i.e. $y=-5$ mm and the respective transverse x

locations associated with it. A profile showing the averaged densities at different transverse x locations at measurement location $y=-10\text{mm}$ is shown in the Figure 44.

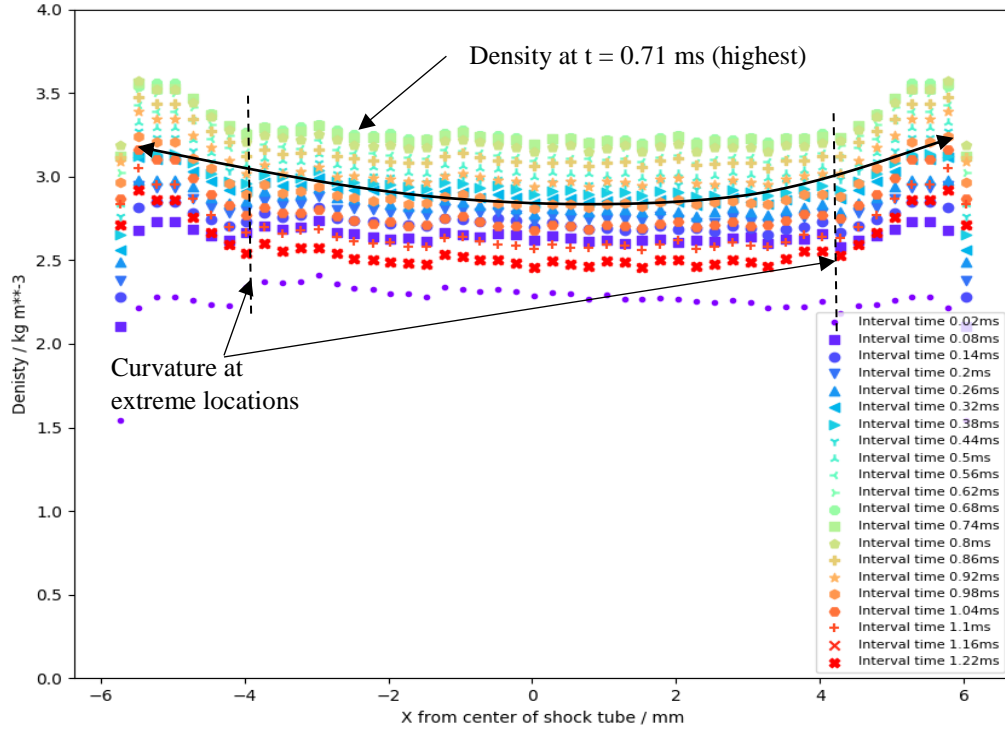


Figure 44. Time dependent average density variation along various transverse x locations

The averaged density profile data for different transverse x locations shown in the figure is noisy but show the same trend of density increase immediately after the shock reflection up until the reaction time is reached ($t=0.71\text{ms}$) and then decreases due to the quenching phenomena as the rarefaction wave reaches the measurement region. However, the variation of time resolved density with respect to x location is relatively flat in the middle section and has some curvature at the extrema as shown by the curve drawn in the middle. Also, it is important to note that the averaged experimental density at the extrema has the most uncertainty associated with it. There exist several reasons for this uncertainty including the small transverse path lengths through the shock tube at the extrema ($x\sim 0$ has a path length of 12.7mm and $x\sim 6.25\text{mm}$ has a path length of about 1mm). In addition, the increase in the path length through the polycarbonate wall

thickness to be traversed increases from the center to the extrema (~2mm at the center to approximately 5cm at extrema). A combination of these factors led to weaker signals at the extrema and hence leading to more noise. The transverse x locations ranging from $x = 4.25$ to 6.25 and $x = -4.25$ to -6.25 mm starts to show the curvature and a relative increase in the uncertainty and noise due to their small shock tube path lengths and increasing polycarbonate wall thickness as shown in the figure. Similar profiles at various y locations have been obtained which show the similar trend of increase in curvature as the extreme transverse locations are approached.

4.4 Radially varying density profiles using abel inversion – Onion Peeling Approach

As mentioned earlier, the advantage in conducting experiments at various transverse x locations was to obtain the radially resolved density to interpret the boundary layer formation in the miniature shock tube as was accomplished by using the Abel Inversion technique, specifically by onion peeling method. The details of the procedure have been mentioned earlier and only the corresponding results are plotted. The radially resolved density is obtained by multiplying the inverse of the chord length matrix with the density variation along transverse x locations. This chord length matrix gives the information on the fraction of the path length associated with each transverse location for which a plot showing the chord length associated with different annuli and transverse x locations is shown in Figure 45.

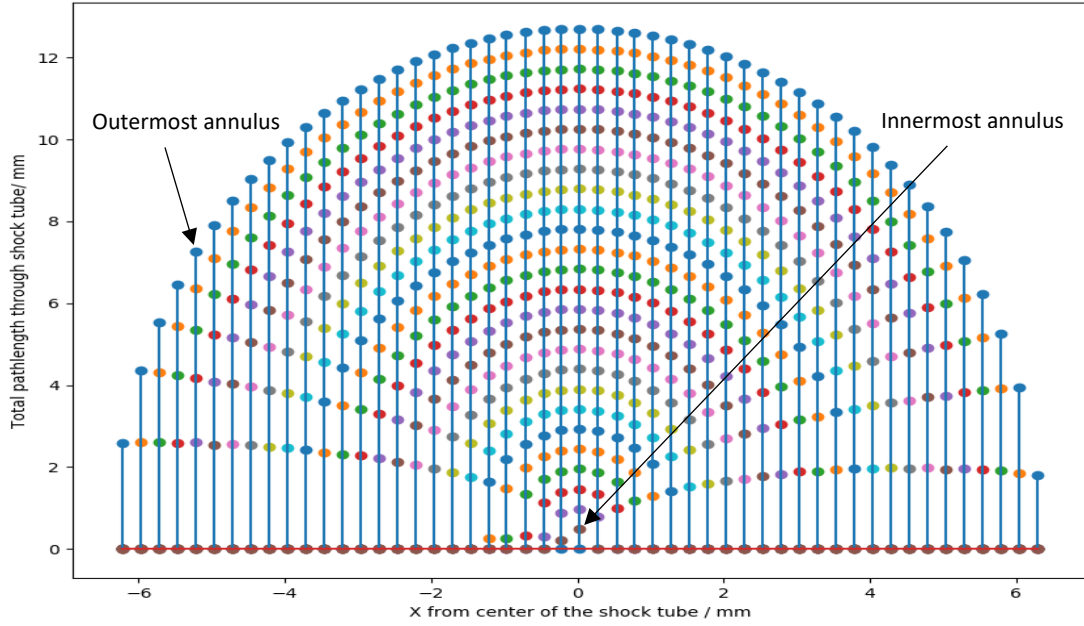


Figure 45. Chord lengths associated with 26 annuli and transverse x locations

The figure shows that the chord length or the shock tube path length is distributed over the 26 different annuli where the center most x location has very small fraction of shock tube path length associated with the center most annulus and the two extreme x locations have the major fraction of the shock tube path length associated with the outermost annuli with a total of 2.584mm on the negative extrema and with 1.8mm on the positive extrema. The rest of the path length associated with these extreme locations is contributed by the polycarbonate wall thickness leading to large uncertainty and noise in the data.

The combination of the chord length matrix and the time resolved density variation with transverse locations helped in achieving the final observation of radially varying density which would further lead to the boundary layer measurement. The radially resolved density profiles varying with time are obtained for radius starting from $r=0$ to $r=6.35$ mm. However, the trend of the radially resolved density profiles had the same increase in density till $t_{\text{peak}} = 0.71$ ms and a decrease thereafter due to the quenching. A plot showing

the radial density variation with respect to time from shock reflection is given by Figure 46. The time periods cover the peak time and the time after quenching begins.

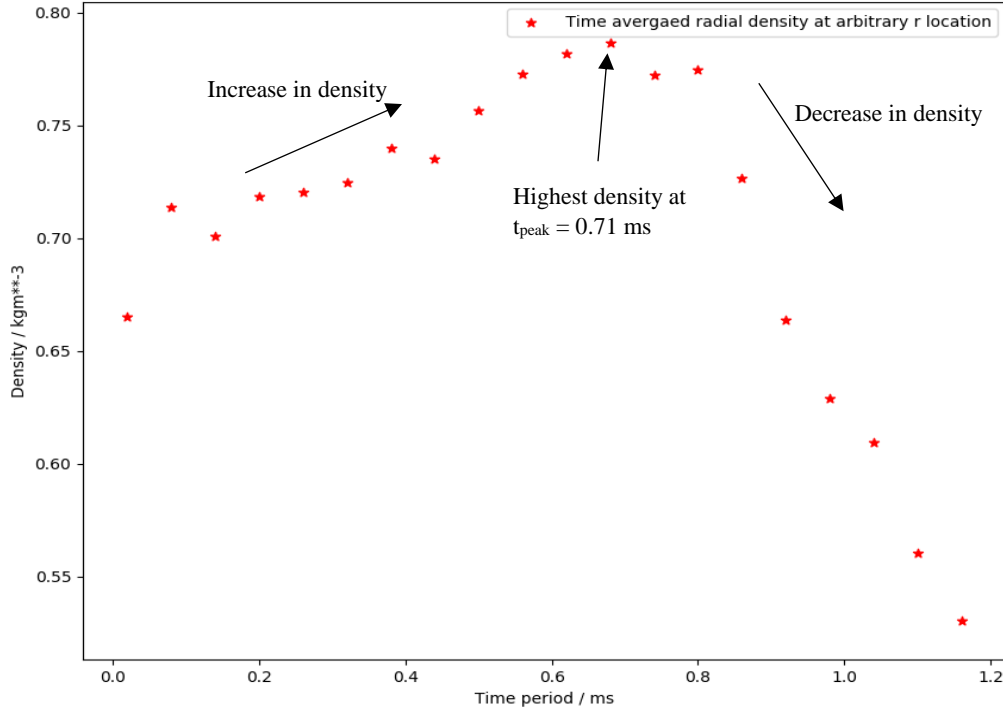


Figure 46. Time averaged radial density profile at a specific r location

The above plot confirms the increase and decrease in radial density profiles which is the same trend observed from the time resolved density profiles. The trends of these profiles are analogous to the pressure profiles as well. However, to analyze the radial density profiles and obtain information regarding the boundary layer thickness, a similar procedure used to analyze the temporal density profiles was employed.

4.4.1 Estimation of boundary layer thickness from radially resolved density profiles

The radial density profiles obtained by Abel Inversion were averaged over 60 μ s time intervals starting from the shock reflection. A profile showing the time averaged radially varying density for the measurement location of $y = -10$ mm is given in the Figure 47. The data presented here has some noise with

it as it is a direct result of implementing the time marching scheme by multiplying the density variation with x location at one time which also incorporates noise in it.

It is clear from the figure that the noise is present at the two extrema but as $r \rightarrow 0$, one would expect to have less noise as the contribution is essentially from the density measured at $x \sim 0$ which had the strongest density measurement due to a larger path length through the shock tube as seen previously. However, for $r \rightarrow 0$, the center annulus does not have a large path length through the shock tube associated with it and can be referred to the Figure 45. This small fraction of the shock tube path length is not enough to average out the error leading to more noise. Similarly, the other extrema $r \rightarrow 6.35\text{mm}$ has large noise due to the fact that,

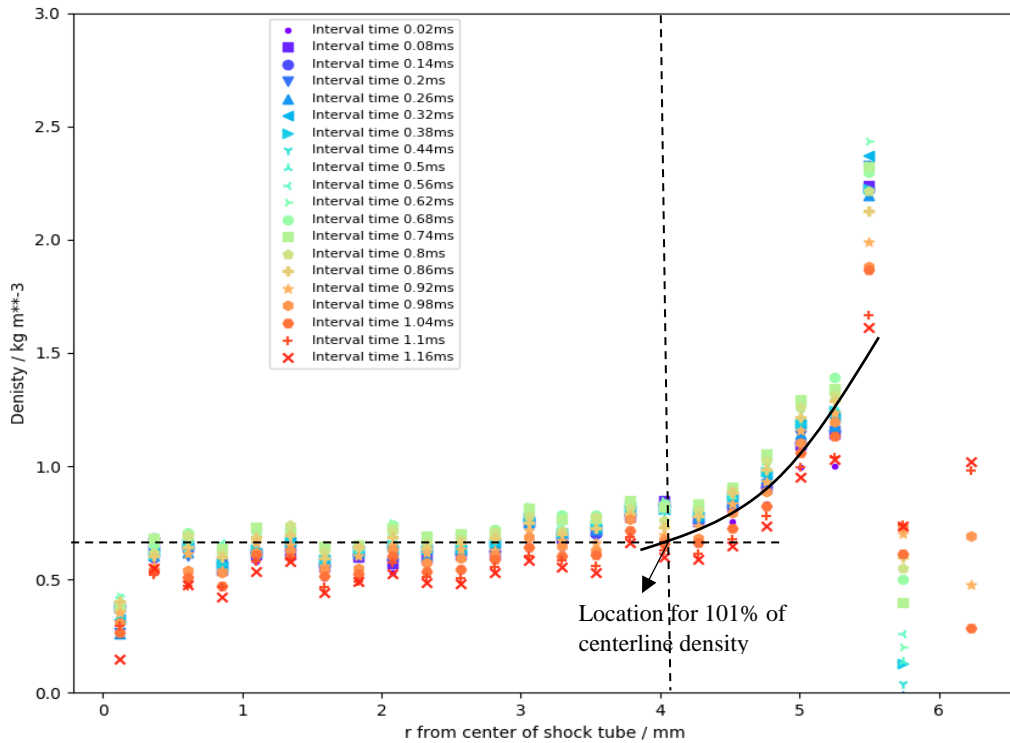


Figure 47. Time dependent density variation along various r locations obtained by Abel transform

though each transverse x location has some shock tube path length associated with the outermost annulus, the major contribution is from the extreme transverse x location ($x \rightarrow 6.35\text{mm}$) which has the low signal

level and large uncertainty because of small shock tube path length and large polycarbonate wall thickness as mentioned previously.

Despite noise, the profile shows an increase in density as the radius approaches the side-wall i.e. as $r \rightarrow 5\text{mm}$ the density profile has a significant curvature and increase till $r \rightarrow 6.35\text{mm}$. This type of behavior is an indication of a growing sidewall boundary layer because of the similar trend in radially resolved density profiles where the total average density increases up to $t = 0.71\text{ms}$ and then decreases. The boundary layer effect is evidently seen in the miniature shock tube, but a clear indication of time varying boundary layer growth would justify the statement. Although the above profile suggests the possibility of growing boundary layer, a better representation of the increase in density as the side-wall is approached was obtained by normalizing the density to a value as $r \rightarrow 0$ and is shown in the Figure 48.

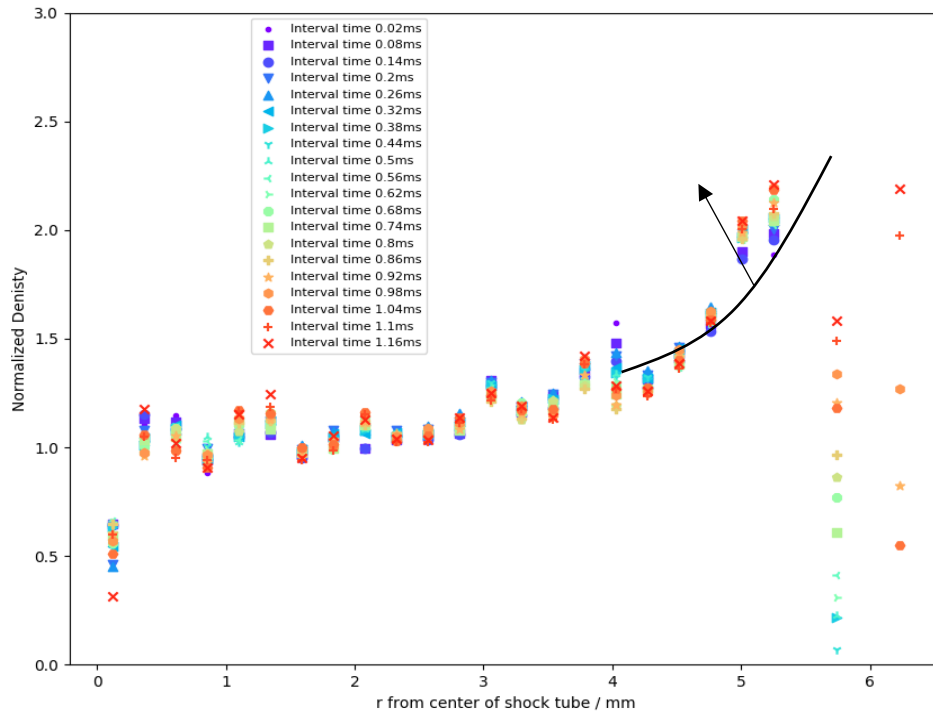


Figure 48. Time varying density variation along the radius of the shock tube obtained by Abel transform- Normalized to density at the center of the shock tube

Despite the noise, the density profile shown in the figure has an increasing profile with a convex shape as the side wall is approached regardless of the density increase or decrease. This trend for radially varying density gave a clear indication of the presence of growing boundary layer and a rough estimate of the boundary layer growth was found to be starting from $r \sim 4.15\text{mm}$, characterized based on the observation where the density approached the 101% of centerline density calculated to be 0.70 kg/m^3 . It was also interesting to notice that the boundary layer thickness observed from the radial density profiles was not changing with time and a possible reason to this could be lack of fine resolution in Abel Inversion technique. Therefore, a relation between the time and boundary layer thickness was not established for the radially resolved density profiles. The representation of boundary layer thickness not varying with time can be shown by the Figure 49, which shows the boundary layer thickness varying with time averaged intervals of $60\text{ }\mu\text{s}$.

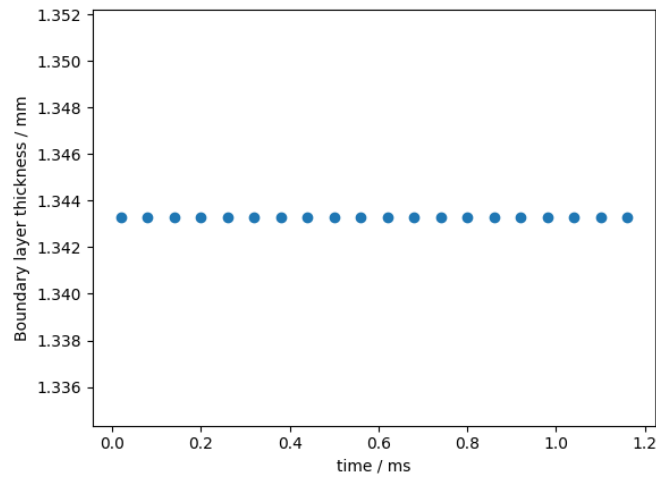


Figure 49. Estimated boundary layer thickness varying with time averaged intervals of $60\text{ }\mu\text{s}$

It is evident that the time dependence of estimated boundary layer thickness from the Abel Inversion cannot be established since there is no evident change visible. Nevertheless, there is a significant difference of 1.5mm between the estimation of growing boundary layer thickness from Abel Inversion and from Lifshitz's boundary layer temperature profiles and a difference of $\sim 0.1\text{mm}$ in the boundary layer thickness

estimated from the experimental density as the boundary layer thickness dependence on time has a similar profile where it increases even more than the thickness estimated from Lifshitz's temperature profile with respect to time. Also, this difference is because the boundary layer thickness calculated from heat conduction concept was solely measuring the thermal boundary layer, whereas the observation from radial density profiles obtained from Abel Inversion is maybe including both the thermal and viscous boundary layer and is to be examined. Also, the onion peeling method is susceptible to noise, specifically as r approaches 0 and the resulting radial density profiles also show the same. Therefore, the difference in boundary layer thickness measurement by two methods can be attributed to some of the reasons stated above and would need further examination.

4.4.2 Radially resolved density measurement using fitting functions and their distributions

One of the last aspects of this study was to evaluate the radially resolved density profiles by estimating the fitting functions to projected data (density profiles changing with x location) as a time marching problem. The fitting functions and their corresponding radial distribution functions were used from the code written by Dr. Alan Kastengren from Argonne National Laboratory. Performing this analysis helped in obtaining the noise-reduced fitting functions and radial distributions of the projected data. Some of the main fitting functions available to use were gaussian, parabolic and an elliptical method. However, out of these functions, the parabolic fitting function and its corresponding radial distribution function were used to best fit the projected data i.e. density variation with x locations.

Fitting the projected data was accomplished by finding the optimized parameters of the fitting function to best fit the projected data. However, the various fits obtained are not completely perfect but do serve the purpose of visualizing the radial density distribution with less amount of noise. For this purpose, time averaged projected data was used, and its corresponding radial distribution was obtained. The time averaged projected data over the region of pre-shock and after the shock reflection is shown in Figure 50 where the time averaged over 300 μs with starting time $t = 175, 475$ and $775 \mu\text{s}$ after shock reflection are considered covering the range of peak time and 80% of the peak time.

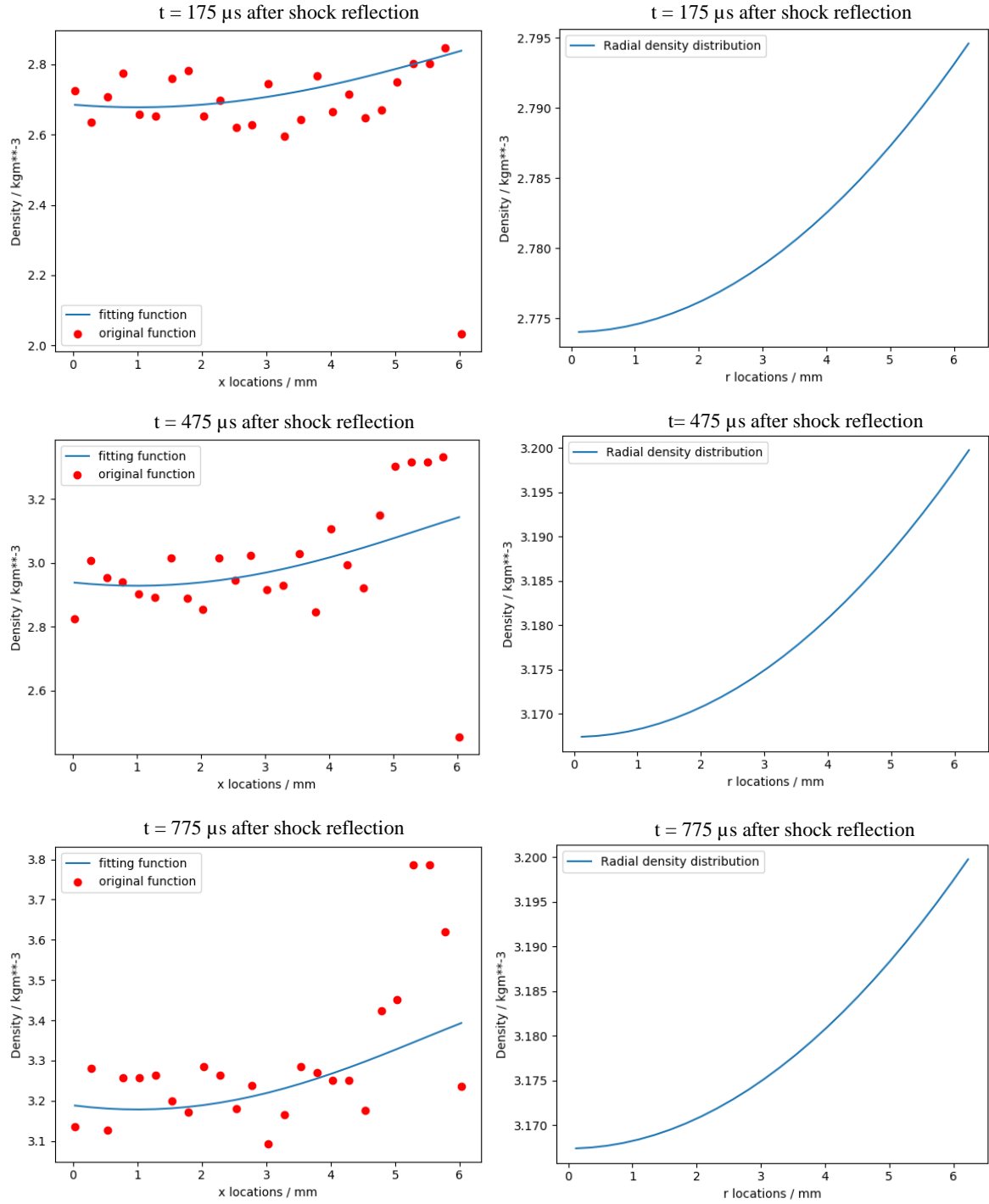


Figure 50. Profiles for fitting functions and their respective radial distributions of projected data at different times

It is evident from the figure that, the fit for the projected data follows the same trend of increase in curvature as the x location reaches the extrema. This is because, only small transverse path lengths through the shock tube are available at the extreme location along with an increase in the polycarbonate wall thickness. In addition to this, the projected data has the most uncertainty in the extreme locations which also contributes to the curvature. However, due to the lack of flat density profile at the initial transverse x locations causes an increase in radial density at the initial radii which is not the same as the one described using the Abel Inversion. Despite this anomaly, the radial density distribution profile has a convex shape as the r approaches the side wall along with less noise associated with it. However, the refinement of the fitting profiles and performing further analysis by using different fitting functions is one of the aspects of future work.

5 SUMMARY AND CONCLUSIONS

Several important results were obtained by performing the analysis of experimental data obtained from X-ray densitometry experiments. The results are highlighted as follows-

- Time varying density of the test gas segregated into pre-shock, behind the incident shock and behind the reflected shock density were obtained by using the Beer's law at different sections of the shock tube which includes various distances from the driven section end wall and along various transverse locations. These experimentally measured densities were compared to the calculated densities obtained by using ideal normal shock relations. The pre-shock densities had an excellent agreement whereas the densities behind the incident shock were in good agreement but increased with time due to the passage of incident shock indicating a growing boundary layer. However, the densities behind the reflected shock were seemingly in agreement only after the shock reflection and increased till t_{peak} in all the cases of different distances from end wall. Hence, suggesting a non-ideal behavior in the region behind the reflected shock density due to the non-ideal effects present in the miniature shock tube i.e. specifically magnified effects of growing boundary layer in small-bore shock tubes such as miniature HRRST.
- Experimental density was validated by implementing the back calculation of density from the isentropic relation and ideal gas equation of state. A significant difference between these densities led to the conclusion of the presence of growing thermal boundary layer and hence was calculated. The boundary layer thickness estimated from the boundary layer temperature profiles using Lifshitz's concept was increasing with time with $\chi \approx 0.7$ mm as the maximum thickness. However, the boundary layer thickness varying with time was also estimated by using the experimental density and the value was found to be more than the value estimated by boundary layer temperature profiles with $\chi \approx 1.51$ mm as the maximum thickness which increases with time. This difference was due to the presence of an adjustable parameter in the path length integrated density whose purpose is to match the experimental density obtained from X-ray densitometry experiments.

- Time dependent density varying along different transverse x locations was obtained at each y location which showed relative flatness in density profile for different time averaged intervals at the nearest x locations and showed some curvature at the extreme locations which was due to the short shock tube path lengths and higher polycarbonate wall thickness to be traversed. This evaluation of density variation at each transverse x location at each time helped in obtaining the radially resolved density at each time using the Abel Inversion technique, specifically the Onion Peeling approach. The radially resolved densities were analyzed by averaging over different time intervals varying with the radius of the shock tube. This analysis showed a rising radial density with a convex shape to the profile as the side wall was approached. The radial density profiles obtained are noisy and have the largest uncertainties at $r \sim 0$ mm and $r \sim 6.35$ mm.

Considering the location of 101% of centerline density as the indicator, the boundary layer thickness was estimated at this location. Significant differences in the boundary layer thickness estimated from Lifshitz's temperature profiles and radial density profiles. Also, a significantly small difference of ~ 0.1 mm between the boundary layer thickness estimated from experimental density and radial density profiles was observed which again is due to the presence of adjustable parameter which matches the experimental density. A noise-free evaluation of projected data and its corresponding radial distribution were obtained by using fitting functions which would need more robust implementation to understand precisely the density increase as the radius approaches the side-wall.

- Finally, the uncertainties in experimental density and calculated densities were obtained by using the concept of error propagation. The uncertainties were calculated by incorporating the ensemble averaging of the data associated with the pre-shock, behind the incident shock and behind the reflected shock regions. It was observed that, the uncertainty in the τ_{empty} and transmitted intensities were the largest contributors to the uncertainty in experimental density causing a larger gap between the upper and lower limit in the uncertainty. Performing the binning method also helped in obtaining the averaged uncertainties which reduced the gap between the upper and lower limit of uncertainty.

The summary presented above concludes that the cold boundary layer growth behind the reflected shock wave was evaluated by using the path length averaged density measurements obtained from the X-ray densitometry experimental data. Various boundary layer models were established and their corresponding boundary layer thicknesses were calculated. The ability to take several line-of-sight measurements was only possible due to the synergy between the attributes of miniature HRRST and synchrotron sources. Performing this study helped in evaluating the non-ideal behavior of the experimental density which held good for isentropic assumption in core gas region but failed for the isotropic assumption in the boundary layer region. The Lifshitz's temperature profile predicted a slower boundary layer growth when compared to the modified Lifshitz's temperature profile which had a fast-growing cold side-wall boundary layer. The boundary layer thickness estimated by performing the Abel Inversion also turned out to be close to the one estimated by modified Lifshitz's temperature profile.

However, the models described here considered the thermal boundary layer growth which related the density rise to the temperature drop in the boundary layer region. Though the model holds true for the isentropic assumption it would need further advancement in formulation to incorporate the other aspect of increase in mass behind the reflected shock which causes the density to increase. Since, the goal of the study was to measure the thermal boundary layer thickness using available tools, it can be concluded with a fair amount of confidence that the study presented here would form one the bounds to an extended version of the new boundary layer models. These models are the few aspects of the future work would take into account several other factors such as increase in mass flow, incident shock attenuation and viscous boundary layer effects and help in refining the existing boundary layer models.

6 RECOMMENDATIONS AND FUTURE WORK

The work presented in this study focuses on the boundary layer measurement in small bore shock tubes such as the miniature HRRST using various techniques. However, several improvements can be incorporated which would give further details on the several measurements presented in this study and would be included in the future work. Some of the important aspects of the future work include-

- Performing more number of experiments would certainly help in eliminating the noise in the data, also achieve low signal to noise ratio by performing ensemble averaging which is one aspect of the future work.
- Developing an advanced model using the current model as a one of the boundary conditions and incorporating the factors of mass flow and viscous boundary layer effects
- Incorporate other boundary layer estimation techniques such as measurement carried out by characterizing and conducting temperature measurements behind the reflected shock region would add another dimension to the estimation of the boundary layer thickness as it depends on temperature.
- Developing a sophisticated model based on this study which could be integrated with the shock tube experiments resulting in measurement of boundary layer effects for every experiment carried out
- The study presented here is for a non-reactive case. However, evaluation of boundary layer thickness for the reactive cases such acetone is in line for immediate future work.
- Finally, implementing this study on the experiments performed in the miniature HRRST with some modifications such as tailoring of driver gas and heating of the shock tube.

CITED LITERATURE

- [1] E.L. Petersen, R.K. Hanson, Nonideal effects behind reflected shock waves in a high-pressure shock tube, *Shock Waves*. 10 (2001) 405–420. doi:10.1007/PL00004051.
- [2] S. Li, W. Ren, D.F. Davidson, R.K. Hanson, Boundary layer effects behind incident and reflected shock waves in a shock tube, 28th Int. Symp. Shock Waves. (2011) 1–6.
- [3] A. Lifshitz, Boundary Layer Effects on Chemical Kinetics Studies in a Shock Tube, *J. Chem. Phys.* 53 (1970) 3050. doi:10.1063/1.1674448.
- [4] P.T. Lynch, G. Wang, Chemical thermometry in miniature HRRST using 1,1,1-trifluoroethane dissociation, *Proc. Combust. Inst.* 36 (2017) 307–314. doi:10.1016/j.proci.2016.05.057.
- [5] M. Tao, A. Laich, P. Lynch, P. Zhao, On the Interpretation and Correlation of High-Temperature Ignition Delays in Reactors with Varying Thermodynamic Conditions, *Int. J. Chem. Kinet.* (2018). doi:10.1002/kin.21170.
- [6] A.G. Gaydon, I.R. Hurle, *The Shock Tube in High Temperature Chemical and Physics*, Reinhold Publishing Corporation, New York, 1963.
- [7] G. Rudinger, Effect of Boundary-Layer Growth in a Shock Tube on Shock Reflection from a Closed End, *Phys. Fluids*. 4 (1961) 1463. doi:10.1063/1.1706244.
- [8] Z. Hong, An Improved Hydrogen/Oxygen Mechanism Based On Shock Tube/Laser Absorption Measurements, *J. Chem. Inf. Model.* (2010) 1689. doi:10.1017/CBO9781107415324.004.
- [9] D.L. Osborn, P. Zou, H. Johnsen, C.C. Hayden, C.A. Taatjes, V.D. Knyazev, S.W. North, D.S. Peterka, M. Ahmed, S.R. Leone, The multiplexed chemical kinetic photoionization mass spectrometer: A new approach to isomer-resolved chemical kinetics, in: *Rev. Sci. Instrum.*, 2008. doi:10.1063/1.3000004.
- [10] C.A. Taatjes, Enols Are Common Intermediates in Hydrocarbon Oxidation, *Science* (80-.). 308

- (2005) 1887–1889. doi:10.1126/science.1112532.
- [11] Y. Li, F. Qi, Recent applications of synchrotron VUV photoionization mass spectrometry: Insight into Combustion Chemistry, *Acc. Chem. Res.* (2010). doi:10.1021/ar900130b.
- [12] F.-X. Ouf, P. Parent, C. Laffon, I. Marhaba, D. Ferry, B. Marcillaud, E. Antonsson, S. Benkoula, X.-J. Liu, C. Nicolas, E. Robert, M. Patanen, F.-A. Barreda, O. Sublemontier, A. Coppalle, J. Yon, F. Miserque, T. Mostefaoui, T.Z. Regier, J.-B.A. Mitchell, C. Miron, First in-flight synchrotron X-ray absorption and photoemission study of carbon soot nanoparticles, *Sci. Rep.* 6 (2016) 36495. <http://dx.doi.org/10.1038/srep36495>.
- [13] J.H. Frank, A. Shavorskiy, H. Bluhm, B. Coriton, D.L. Osborn, In situ soft X-Ray absorption spectroscopy of flames, in: 8th US Natl. Combust. Meet. 2013, 2013.
- [14] N. Hansen, R.S. Tranter, J.B. Randazzo, J.P.A. Lockhart, A.L. Kastengren, Investigation of sampling-probe distorted temperature fields with X-ray fluorescence spectroscopy, *Proc. Combust. Inst.* (2018). doi:<https://doi.org/10.1016/j.proci.2018.05.034>.
- [15] A.L. Kastengren, C.F. Powell, Spray density measurements using X-ray radiography, *J. Automob. Eng.* 221 (2007) 653–662. doi:10.1243/09544070JAUTO392.
- [16] P.T. Lynch, T.P. Troy, M. Ahmed, R.S. Tranter, Probing combustion chemistry in a miniature shock tube with synchrotron VUV photo ionization mass spectrometry, *Anal. Chem.* 87 (2015) 2345–2352. doi:10.1021/ac5041633.
- [17] A.M. Gänzler, M. Casapu, A. Boubnov, O. Müller, S. Conrad, H. Lichtenberg, R. Frahm, J.D. Grunwaldt, Operando spatially and time-resolved X-ray absorption spectroscopy and infrared thermography during oscillatory CO oxidation, *J. Catal.* (2015). doi:10.1016/j.jcat.2015.01.002.
- [18] G.A. Garcia, X. Tang, J.-F. Gil, L. Nahon, M. Ward, S. Batut, C. Fittschen, C.A. Taatjes, D.L. Osborn, J.-C. Loison, Synchrotron-based double imaging photoelectron/photoion coincidence

- spectroscopy of radicals produced in a flow tube: OH and OD, *J. Chem. Phys.* 142 (2015) 164201. doi:10.1063/1.4918634.
- [19] F. Battin-Leclerc, O. Herbinet, P.A. Glaude, R. Fournet, Z. Zhou, L. Deng, H. Guo, M. Xie, F. Qi, New experimental evidences about the formation and consumption of ketohydroperoxides, *Proc. Combust. Inst.* 33 (2011) 325–331. doi:10.1016/j.proci.2010.05.001.
- [20] D. Felsmann, K. Moshhammer, J. Krüger, A. Lackner, A. Brockhinke, T. Kasper, T. Bierkandt, E. Akyildiz, N. Hansen, A. Lucassen, P. Oßwald, M. Köhler, G.A. Garcia, L. Nahon, P. Hemberger, A. Bodi, T. Gerber, K. Kohse-Höinghaus, Electron ionization, photoionization and photoelectron/photoion coincidence spectroscopy in mass-spectrometric investigations of a low-pressure ethylene/oxygen flame, *Proc. Combust. Inst.* (2015). doi:10.1016/j.proci.2014.05.151.
- [21] P.M. De Lurgio, G.R. Drake, A.S. Kreps, G. Jennings, J.T. Weizeorick, M.J. Molitsky, I.S. Naday, J.P. Hessler, A high-speed one-dimensional detector for time-resolved small-angle X-ray scattering: Design and characterization, *IEEE Trans. Nucl. Sci.* 57 (2010) 1706–1715. doi:10.1109/TNS.2010.2045233.
- [22] J.B.A. Mitchell, J.L. Legarrec, G. Saidani, F. Lefevre, S. Di Stasio, Synchrotron radiation studies of additives in combustion, III: Ferrocene, in: *Energy and Fuels*, 2013. doi:10.1021/ef400758a.
- [23] F. Ossler, L. Vallenhag, S.E. Canton, J.B.A. Mitchell, J.L. Le Garrec, M. Sztucki, S. Di Stasio, Dynamics of incipient carbon particle formation in a stabilized ethylene flame by in situ extended-small-angle- and wide-angle X-ray scattering, *Carbon N. Y.* (2013). doi:10.1016/j.carbon.2012.07.038.
- [24] M.B. Olatinwo, K. Ham, J. McCarney, S. Marathe, J. Ge, G. Knapp, L.G. Butler, Analysis of Flame Retardancy in Polymer Blends by Synchrotron X-ray K-edge Tomography and Interferometric Phase Contrast Movies, *J. Phys. Chem. B.* (2016). doi:10.1021/acs.jpcc.5b12775.

- [25] C. D. Radke, P. McManamen, A. L. Kastengren, B. R. Halls, T. Meyer, Quantitative time-averaged gas and liquid distributions using x-ray fluorescence and radiography in atomizing sprays, 2015. doi:10.1364/OL.40.002029.
- [26] D.J. Duke, A.L. Kastengren, F.Z. Tilocco, A.B. Swantek, C.F. Powell, X-Ray Radiography Measurements of Cavitating Nozzle Flow, *At. Sprays*. (2013). doi:10.1615/AtomizSpr.2013008340.
- [27] M. Linne, Analysis of X-ray radiography in atomizing sprays, *Exp. Fluids*. (2012). doi:10.1007/s00348-012-1312-6.
- [28] E.R. Mysak, K.R. Wilson, M. Jimenez-Cruz, M. Ahmed, T. Baer, Synchrotron radiation based aerosol time-of-flight mass spectrometry for organic constituents, *Anal. Chem.* (2005). doi:10.1021/ac050440e.
- [29] A. Braun, Application of small angle and wide angle X-ray scattering for the characterization of carbonaceous materials, aerosols, and particles, 2006.
- [30] R.S. Tranter, P.T. Lynch, A miniature high repetition rate shock tube, *Rev. Sci. Instrum.* 84 (2013). doi:10.1063/1.4820917.
- [31] A. Kastengren, C.F. Powell, D. Arms, E.M. Dufresne, H. Gibson, J. Wang, The 7BM beamline at the APS: A facility for time-resolved fluid dynamics measurements, *J. Synchrotron Radiat.* (2012). doi:10.1107/S0909049512016883.
- [32] R.L. Burton, J.C. Slaybaugh, A laser interferometer schlieren system for high frequency gas density measurements, *Rev. Sci. Instrum.* 41 (1970) 581–584. doi:10.1063/1.1684583.
- [33] B.R. Giri, H. Xu, R. Sivaramakrishnan, J.H. Kiefer, R.S. Tranter, Thermal decomposition of vinyl fluoride: A combined time of flight mass spectrometry/laser schlieren densitometry shock tube study, in: 5th US Combust. Meet. 2007, 2007: pp. 1089–1096.

- [34] J.D. Anderson, Modern Compressible Flow with Historic Perspective, Third, McGraw Hill Education (India), 2012.
- [35] J.H. Kiefer, R.W. Lutz, Recombination of oxygen atoms at high temperatures as measured by shock-tube densitometry, *J. Chem. Phys.* 42 (1965) 1709–1714. doi:10.1063/1.1696181.
- [36] B.L. Henke, E.M. Gullikson, J.C. Davis, X-Ray Interactions: Photoabsorption, Scattering, Transmission, and Reflection at $E = 50\text{--}30,000$ eV, $Z = 1\text{--}92$, *At. Data Nucl. Data Tables.* 54 (1993) 181–342. doi:10.1006/ADND.1993.1013.
- [37] P.T. Lynch, Note: An improved solenoid driver valve for miniature shock tubes, *Rev. Sci. Instrum.* 87 (2016). doi:10.1063/1.4953115.
- [38] L. Lyons, A Practical Guide to Data Analysis for Physical Science Students, 1991.
- [39] M. Kalal, K. a Nugent, Abel inversion using fast Fourier transforms., *Appl. Opt.* 27 (1988) 1956–1959. doi:10.1364/AO.27.001956.
- [40] N.Y. Joshi, P.K. Atrey, S.K. Pathak, Abel inversion of asymmetric plasma density profile at Aditya tokamak, in: *J. Phys. Conf. Ser.*, 2010. doi:10.1088/1742-6596/208/1/012129.
- [41] Y.T. Cho, S.J. Na, Application of Abel inversion in real-time calculations for circularly and elliptically symmetric radiation sources, *Meas. Sci. Technol.* 16 (2005) 878–884. doi:10.1088/0957-0233/16/3/032.
- [42] W. Tang, K. Brezinsky, Chemical kinetic simulations behind reflected shock waves, *Int. J. Chem. Kinet.* 38 (2006) 75–97. doi:10.1002/kin.20134.
- [43] R.S. Tranter, R. Sivaramakrishnan, N. Srinivasan, K. Brezinsky, Calibration of reaction temperatures in a very high pressure shock tube using chemical thermometers, *Int. J. Chem. Kinet.* (2001). doi:10.1002/kin.1069.

- [44] D. Bershader, J. O. Bunting, R. S. Devoto, Thermal Conductivity of Shock-Heated Argon, 1969.
doi:10.1063/1.1692637.

APPENDIX

Formulae used in uncertainty calculation for densities:

1. Experimental density

The experimental density which is calculated from beer's law is given by the formula

$$\rho_{\text{exp}} = \frac{-\log(\tau_{\text{shocktube}})}{\sigma_{9\text{kev}} * \text{PL}} \quad (1)$$

Where, $\tau_{\text{shocktube}}$ is given by

$$\tau_{\text{shocktube}} = \frac{(I_t - I_{1(\text{dark})})}{\frac{(I_{\text{inc}} - I_{0(\text{dark})})}{(\tau_{\text{empty}})}} \quad (2)$$

The uncertainty in the experimental density from error propagation analysis is given as

$$\sigma_{(\rho_{\text{exp}})} = \sqrt{\left[\left(\frac{\partial \rho_{\text{exp}}}{\partial I_1} \right)^2 * (\sigma_{(I_t)})^2 + \left(\frac{\partial \rho_{\text{exp}}}{\partial I_{1(\text{dark})}} \right)^2 * (\sigma_{(I_{1(\text{dark})})})^2 + \left(\frac{\partial \rho_{\text{exp}}}{\partial I_{\text{inc}}} \right)^2 * (\sigma_{(I_{\text{inc}})})^2 \right.} \\ \left. + \left(\frac{\partial \rho_{\text{exp}}}{\partial I_{0(\text{dark})}} \right)^2 * (\sigma_{(I_{0(\text{dark})})})^2 + \left(\frac{\partial \rho_{\text{exp}}}{\partial \tau_{\text{empty}}} \right)^2 * (\sigma_{(\tau_{\text{empty}})})^2 \right. \\ \left. + \left(\frac{\partial \rho_{\text{exp}}}{\partial \text{PL}} \right)^2 * (\sigma_{(\text{PL})})^2 + \left(\frac{\partial \rho_{\text{exp}}}{\partial \sigma_{9\text{kev}}} \right)^2 * (\sigma_{(\sigma_{9\text{kev}})})^2 \right] \quad (3)$$

Where, the partial derivatives and their notations are given by

- Partial derivative of experimental density w.r.t transmitted intensity is given by

$$\frac{\partial \rho_{\text{exp}}}{\partial I_1} = \frac{-1}{(I_1 - I_{1(\text{dark})}) * (\text{PL} * \sigma_{9\text{kev}})} \quad (4)$$

- Partial derivative of experimental density w.r.t Transmitted intensity (dark) given by

$$\frac{\partial \rho_{\text{exp}}}{\partial I_{1(\text{dark})}} = \frac{1}{(I_1 - I_{1(\text{dark})}) * (PL * \sigma_{9\text{kev}})} \quad (5)$$

- Partial derivative of experimental density w.r.t incident intensity given by

$$\frac{\partial \rho_{\text{exp}}}{\partial I_{\text{inc}}} = \frac{1}{(I_{\text{inc}} - I_{0(\text{dark})}) * (PL * \sigma_{9\text{kev}})} \quad (6)$$

- Partial derivative of experimental density w.r.t incident intensity (dark) given by

$$\frac{\partial \rho_{\text{exp}}}{\partial I_{\text{inc(dark)}}} = \frac{-1}{(I_{\text{inc}} - I_{0(\text{dark})}) * (PL * \sigma_{9\text{kev}})} \quad (7)$$

- Partial derivative of experimental density w.r.t tau empty given by

$$\frac{\partial \rho_{\text{exp}}}{\partial \log(\tau_{\text{empty}})} = \frac{1}{(PL * \sigma_{9\text{kev}})} \quad (8)$$

- Partial derivative of experimental density w.r.t path length given by

$$\frac{\partial \rho_{\text{exp}}}{\partial PL} = \frac{\log\left(\frac{I_t - I_{1(\text{dark})}}{\frac{I_{\text{inc}} - I_{0(\text{dark})}}{\tau_{\text{empty}}}}\right)}{((PL)^2 * \sigma_{9\text{kev}})} \quad (9)$$

- Partial derivative of experimental density w.r.t absorption coefficient given by

$$\frac{\partial \rho_{\text{exp}}}{\partial \sigma_{9\text{kev}}} = \frac{\log\left(\frac{I_t - I_{1(\text{dark})}}{\frac{I_{\text{inc}} - I_{0(\text{dark})}}{\tau_{\text{empty}}}}\right)}{(PL * (\sigma_{9\text{kev}})^2)} \quad (10)$$

The uncertainties in the individual parameters are considered as follows and are similarly tabulated in Table 7.

- $\sigma_{(I_t)}$ = Uncertainty in transmitted intensity given by $\sigma_{(I_t)} = 2 * \text{stdev}$, where stdev is the standard deviation in transmitted intensities
- $\sigma_{(I_{1(\text{dark})})}$ = Uncertainty in transmitted intensity (dark) is given by

$$\sigma_{(I_{1(\text{dark})})} = 2 * \frac{\text{average}(\text{transmitted intensity stdev})}{\sqrt{n}}$$

- iii. $\sigma_{(I_{\text{inc}})}$ = Uncertainty in incident intensity and is given by $\sigma_{(I_{\text{inc}})} = 2 * \text{stdev}$ where stdev is the standard deviation in incident intensities

- iv. $\sigma_{(I_{0(\text{dark})})}$ = Uncertainty in incident intensity (dark) is given by

$$\sigma_{(I_{0(\text{dark})})} = 2 * \frac{\text{average}(\text{incident_intensity_stdev})}{\sqrt{n}}$$

- v. $\sigma_{(\tau_{\text{empty}})}$ = Uncertainty in $\ln(\tau_{\text{empty}})$ is calculated using the student t-distribution uncertainty formula for the scattered data at the location of least wall thickness which can referred to Figure 19.

$$\sigma_{(\tau_{\text{empty}})} = \frac{t * s}{\sqrt{N}}$$

Where $t = 2.003$ is the student-t value for 95% confidence level and

s = Standard deviation

- vi. $\sigma_{(\text{PL})}$ = Uncertainty in pathlength is calculated by using the concept of geometry and is given by the formula

$$\sigma_{(\text{PL})} = \sqrt{\left(\frac{4 * R_t^2}{R_t^2 - X_t^2}\right) * \sigma_{(R_t)}}, \text{ with } \sigma_{(R_t)} = 1.27\text{e-}5 \text{ mm}$$

- vii. $\sigma_{(\sigma_{9\text{kev}})}$ = Uncertainty in the absorption coefficient is taken to be the difference between the value obtained from X-ray properties of elements and calculated value (8.598-8.494)

2. Calculated densities

The calculated densities are obtained by using the *ideal normal shock equations* given by

For behind incident shock conditions P_2, T_2

$$\frac{P_2}{P_1} = 1 + \frac{2\gamma}{\gamma + 1} ((M_s)^2 - 1) \quad (11)$$

$$\frac{T_2}{T_1} = \frac{1 + \frac{\gamma-1}{\gamma+1} * \left(\frac{P_2}{P_1}\right)}{1 + \frac{\gamma-1}{\gamma+1} * \left(\frac{P_1}{P_2}\right)} \quad (12)$$

Substituting Equation 11 in 12, we get

$$\frac{T_2}{T_1} = \frac{[(\gamma-1) * (M_s)^2 + 2] * [2\gamma * (M_s)^2 - (\gamma-1)]}{(\gamma+1)^2 * (M_s)^2} \quad (13)$$

For behind reflected shock conditions P_5, T_5

$$\frac{P_5}{P_1} = \left[\frac{2\gamma * (M_s)^2 - (\gamma-1)}{(\gamma+1)} \right] * \left[\frac{-2(\gamma-1) + (M_s)^2 * (3\gamma-1)}{2 + (M_s)^2 * (\gamma-1)} \right] \quad (14)$$

$$\frac{T_5}{T_1} = \left\{ \frac{[2(\gamma-1) * (M_s)^2 + 3 - \gamma] * [(3\gamma-1) * (M_s)^2 - 2(\gamma-1)]}{(\gamma+1)^2 * (M_s)^2} \right\} \quad (15)$$

Now,

2.1 Pre-shock density (ρ_1):

The pre-shock density is given by the Ideal Gas Equation of state where,

$$\rho_1 = \frac{P_1}{R * T_1} \quad (16)$$

And the uncertainty in ρ_1 is given by

$$\sigma_{(\rho_1)} = \sqrt{\left(\frac{\partial \rho_1}{\partial P_1}\right)^2 * (\sigma_{(P_1)})^2 + \left(\frac{\partial \rho_1}{\partial T_1}\right)^2 * (\sigma_{(T_1)})^2} \quad (17)$$

Where the partial derivatives are given by:

- Partial derivative of ρ_1 w.r.t P_1 is given by

$$\frac{\partial \rho_1}{\partial P_1} = \frac{1}{R * T_1} \quad (18)$$

- Partial derivative of ρ_1 w.r.t T_1 is given by

$$\frac{\partial \rho_1}{\partial T_1} = \frac{-P_1}{R * T_1^2} \quad (19)$$

And the uncertainties considered are $\sigma_{(P_1)} = 0.05 * P_1$, $\sigma_{(T_1)} = 0.5$ and the specific gas constant $R = 8314/39.95 = 208 \text{ J/kg-K}$ (for Argon gas)

2.2 Behind incident shock density (ρ_2):

We know from Ideal Gas Equation of state that

$$\rho_2 = \frac{P_2}{R * T_2} \quad (20)$$

And the uncertainty in ρ_2 is given by

$$\sigma_{(\rho_2)} = \sqrt{\left(\frac{\partial \rho_2}{\partial P_2}\right)^2 * (\sigma_{(P_2)})^2 + \left(\frac{\partial \rho_2}{\partial T_2}\right)^2 * (\sigma_{(T_2)})^2} \quad (21)$$

The behind the incident shock density ρ_2 when converted in terms of P_1 and T_1 by using Equation 11 and 13 results in a new uncertainty equation is given by

$$\sigma_{(\rho_2)} = \sqrt{\left(\frac{\partial \rho_2}{\partial P_1}\right)^2 * (\sigma_{(P_1)})^2 + \left(\frac{\partial \rho_2}{\partial T_1}\right)^2 * (\sigma_{(T_1)})^2 + \left(\frac{\partial \rho_2}{\partial M_s}\right)^2 * (\sigma_{(M_s)})^2}$$

Where, the partial derivatives are given by

- Partial derivative of ρ_2 w.r.t P_1 is given by

$$\frac{\partial \rho_2}{\partial P_1}$$

$$= \frac{1}{R * T_1} * \left[\frac{(\gamma + 1)^2 * (M_s)^2 + 2\gamma(\gamma + 1) * [(M_s)^4 - (M_s)^2]}{2\gamma(\gamma - 1) * (M_s)^4 - (\gamma - 1)^2 * (M_s)^2 + 4\gamma * (M_s)^2 - 2(\gamma - 1)} \right] \quad (22)$$

- Partial derivative of ρ_2 w.r.t T_1 is given by

$$\frac{\partial \rho_2}{\partial T_1}$$

$$= \frac{-P_1}{R * T_1^2} * \left[\frac{(\gamma + 1)^2 * (M_s)^2 + 2\gamma(\gamma + 1) * [(M_s)^4 - (M_s)^2]}{2\gamma(\gamma - 1) * (M_s)^4 - (\gamma - 1)^2 * (M_s)^2 + 4\gamma * (M_s)^2 - 2(\gamma - 1)} \right] \quad (23)$$

- Partial derivative of ρ_2 w.r.t M_s is given by

$$\frac{\partial \rho_2}{\partial M_s} = \frac{P_1}{R * T_1} * \frac{4(\gamma + 1) * M_s}{((\gamma - 1) * (M_s)^2 + 2)^2} \quad (24)$$

Where the uncertainties in P_1 and T_1 are the same as the ones used in previous calculation.

The uncertainty in shock Mach number is given by $\sigma_{(M_s)}$ and for which we have the formula for Mach number given by

$$M_s = \frac{V_s}{\sqrt{\gamma * R * T_1}} \quad (25)$$

Here, V_s is the shock velocity, R is the specific gas constant for Argon gas and T_1 is the initial temperature.

The uncertainty in shock Mach number is given by

$$\sigma_{(M_s)} = \sqrt{\left(\frac{\partial M_s}{\partial V_s}\right)^2 * (\sigma_{(V_s)})^2 + \left(\frac{\partial M_s}{\partial T_1}\right)^2 * (\sigma_{(T_1)})^2} \quad (26)$$

Where, the partial derivatives are given by

- Partial derivative of M_s w.r.t shock velocity V_s is given by

$$\frac{\partial M_s}{\partial V_s} = \frac{1}{\sqrt{\gamma * R * T_1}} \quad (27)$$

- Partial derivative of M_s w.r.t shock velocity T_1 is given by

$$\frac{\partial M_s}{\partial T_1} = \frac{-V_s}{2\sqrt{\gamma * R * (T_1)^3}} \quad (28)$$

For which the uncertainty in shock velocity is given by

$$\sigma_{(V_s)} = \sqrt{\left(\frac{\partial V_s}{\partial d}\right)^2 * (\sigma_{(d)})^2 + \left(\frac{\partial V_s}{\partial t}\right)^2 * (\sigma_{(t)})^2} \quad (29)$$

Where the partial derivatives in the equation are given by:

- Partial derivative of shock velocity w.r.t distance between the time arrival sensors (spacings) is given by

$$\frac{\partial V_s}{\partial d} = \frac{1}{t} \quad (30)$$

- Partial derivative of shock velocity w.r.t time between the shock arrival at each sensor is given by

$$\frac{\partial V_s}{\partial t} = \frac{-d}{t^2} \quad (31)$$

For which the uncertainty in distance and time is given by $\sigma_{(d)} = 5e - 5$, $\sigma_{(t)} = 2e - 7$ respectively

2.3 Behind the reflected shock density (ρ_5):

We know from Ideal Gas Equation of state that

$$\rho_5 = \frac{P_5}{R * T_5} \quad (32)$$

And the uncertainty in ρ_5 is given by

$$\sigma_{(\rho_5)} = \sqrt{\left(\frac{\partial \rho_5}{\partial P_5}\right)^2 * (\sigma_{(P_5)})^2 + \left(\frac{\partial \rho_5}{\partial T_5}\right)^2 * (\sigma_{(T_5)})^2} \quad (33)$$

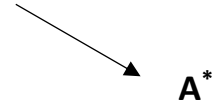
The behind the reflected shock density ρ_5 when converted in terms of P_1 and T_1 by using Equation 14 and 15 results in a new uncertainty equation is given by

$$\sigma_{(\rho_5)} = \sqrt{\left(\frac{\partial \rho_5}{\partial P_1}\right)^2 * (\sigma_{(P_1)})^2 + \left(\frac{\partial \rho_5}{\partial T_1}\right)^2 * (\sigma_{(T_1)})^2 + \left(\frac{\partial \rho_5}{\partial M_s}\right)^2 * (\sigma_{(M_s)})^2} \quad (34)$$

And the density behind the reflected shock is converted to

$$\rho_5 = \frac{P_1}{R * T_1} * \left\{ \frac{[2\gamma * (M_s)^2 - (\gamma - 1)] * [-2(\gamma - 1) + (M_s)^2 * (3\gamma - 1)] * [(\gamma + 1) * (M_s)^2]}{[2(\gamma - 1) * (M_s)^2 + 3 - \gamma] * [(3\gamma - 1) * (M_s)^2 - 2(\gamma - 1)] * [2 + (M_s)^2 * (\gamma - 1)]} \right\}$$

considered as A^*



Where, the partial derivatives are given by

- Partial derivative of ρ_5 w.r.t P_1 is given by,

$$\frac{\partial \rho_5}{\partial P_1} = \frac{1}{R * T_1} * A^* \quad (35)$$

- Partial derivative of ρ_5 w.r.t T_1 is given by

$$\frac{\partial \rho_5}{\partial T_1} = \frac{-P_1}{R * T_1^2} * A^* \quad (36)$$

- Partial derivative of ρ_5 w.r.t M_s is given by

$$\begin{aligned} \frac{\partial \rho_5}{\partial M_s} = \frac{P_1}{R * T_1} * & \left[\frac{4(\gamma + 1)^2 * M_s}{(\gamma - 1) * (\gamma * (M_s)^2 - (M_s)^2 + 2)^2} \right. \\ & \left. + \frac{4 * M_s * (\gamma^2 - 2\gamma - 3)}{(\gamma - 1) * (2\gamma * (M_s)^2 - \gamma - 2(M_s)^2 + 3)^2} \right] \end{aligned} \quad (37)$$

Where the uncertainties in P_1 and T_1 are the same as the ones used in previous calculation.

The uncertainty in shock Mach number is given by $\sigma_{(M_s)}$ whose details are mentioned in the previous section.

The reflected shock velocity is given by equation

$$\frac{M_R}{M_R^2 - 1} = \frac{M_s}{M_s^2 - 1} \sqrt{1 + \frac{2(\gamma - 1)}{(\gamma + 1)^2} (M_s^2 - 1) \left(\gamma + \frac{1}{M_s^2} \right)} \quad (38)$$

NOMENCLATURE

Description	Symbol	Units
Incident Shock Mach number	M_s	No unit
Path length (1mm = 0.001 m)	PL	mm
Pre-shock / Initial pressure (1 bar = 100000 N/m ²)	P_1	bar
Behind the incident shock pressure	P_2	bar
Behind the reflected shock pressure	P_5	bar
Pre-shock / Initial temperature	T_1	K
Behind the incident shock temperature	T_2	K
Behind the reflected shock temperature	T_5	K
Transmitted Intensity	I_1	Arb.
Transmitted Intensity (dark)	$I_{1(dark)}$	Arb
Incident Intensity	I_0	Arb
Incident Intensity (dark)	$I_{0(dark)}$	Arb
Photo absorption cross section coefficient	σ_{9kev}	m ² /kg
Experimental density	ρ_{exp}	kg/m ³
Pre-shock density	ρ_1	kg/m ³
Behind the incident shock density	ρ_2	kg/m ³
Behind the reflected shock density	ρ_5	kg/m ³
Transmissivity through shock tube (empty)	τ_{empty}	No unit
Partial derivative of ρ_{exp} w.r.t I_1	$\frac{\partial \rho_{exp}}{\partial I_1}$	$\frac{kg}{m^3 * cd}$
Partial derivative of ρ_{exp} w.r.t $I_{1(dark)}$	$\frac{\partial \rho_{exp}}{\partial I_{1(dark)}}$	$\frac{kg}{m^3 * cd}$
Partial derivative of ρ_{exp} w.r.t I_{inc}	$\frac{\partial \rho_{exp}}{\partial I_{inc}}$	$\frac{kg}{m^3 * cd}$

Partial derivative of ρ_{exp} w.r.t $I_{0(\text{dark})}$	$\frac{\partial \rho_{\text{exp}}}{\partial I_{0(\text{dark})}}$	$\frac{\text{kg}}{\text{m}^3 * \text{cd}}$
Partial derivative of ρ_{exp} w.r.t τ_{empty}	$\frac{\partial \rho_{\text{exp}}}{\partial I_{\tau_{\text{empty}}}}$	$\frac{\text{kg}}{\text{m}^3}$
Partial derivative of ρ_{exp} w.r.t path length	$\frac{\partial \rho_{\text{exp}}}{\partial I_{\text{PL}}}$	$\frac{\text{kg}}{\text{m}^4}$
Partial derivative of ρ_{exp} w.r.t $\sigma_{9\text{kev}}$	$\frac{\partial \rho_{\text{exp}}}{\partial I_{9\text{kev}}}$	$\frac{\text{kg}^2}{\text{m}^5}$
Partial derivative of ρ_1 w.r.t P_1	$\frac{\partial \rho_1}{\partial P_1}$	kg/N-m
Partial derivative of ρ_1 w.r.t T_1	$\frac{\partial \rho_1}{\partial T_1}$	$\text{kg/m}^3 * \text{K}$
Partial derivative of ρ_2 w.r.t P_1	$\frac{\partial \rho_2}{\partial P_1}$	kg/N-m
Partial derivative of ρ_2 w.r.t T_1	$\frac{\partial \rho_2}{\partial T_1}$	$\text{kg/m}^3 * \text{K}$
Partial derivative of ρ_2 w.r.t M_s	$\frac{\partial \rho_2}{\partial M_s}$	kg/m^3
Partial derivative of ρ_5 w.r.t P_1	$\frac{\partial \rho_5}{\partial P_1}$	kg/N-m
Partial derivative of ρ_5 w.r.t T_1	$\frac{\partial \rho_5}{\partial T_1}$	$\text{kg/m}^3 * \text{K}$
Partial derivative of ρ_5 w.r.t M_s	$\frac{\partial \rho_5}{\partial M_s}$	kg/m^3
Partial derivative of M_s w.r.t. shock velocity	$\frac{\partial M_s}{\partial V_s}$	$\frac{\text{kg}^{1/2}}{\text{J}^{1/2}}$
Partial derivative of M_s w.r.t. T_1	$\frac{\partial M_s}{\partial T_1}$	$\frac{\text{m} * \text{kg}^{1/2}}{\text{J}^{1/2} * \text{K} * \text{s}}$
Partial derivative if shock velocity w.r.t distance (spacings)	$\frac{\partial V_s}{\partial d}$	$1/\text{s}$

Partial derivative of shock velocity w.r.t time	$\frac{\partial V_s}{\partial t}$	$\frac{m}{s^2}$
Uncertainty in transmitted intensity	$\sigma_{(I_t)}$	Arb
Uncertainty in transmitted intensity (dark)	$\sigma_{(I_{1(dark)})}$	Arb
Uncertainty in incident intensity	$\sigma_{(I_{inc})}$	Arb
Uncertainty in incident intensity (dark)	$\sigma_{(I_{0(dark)})}$	Arb
Uncertainty in τ_{empty}	$\sigma_{(\tau_{empty})}$	No unit
Uncertainty in path length	$\sigma_{(PL)}$	m
Uncertainty in absorption coefficient	$\sigma_{(\sigma_{9kev})}$	m ² /kg
Uncertainty in initial	σ_{P1}	N/m ²
Uncertainty in initial temperature	$\sigma_{(T1)}$	K
Uncertainty in spacings	$\sigma_{(d)}$	m
Uncertainty in time	$\sigma_{(t)}$	s (seconds)

VITA

Name	Rizwan A. Shaik
Education	<p>Bachelor of Engineering (B.E.), Mechanical Engineering, <i>Osmania University, Hyderabad-India</i>, 2016</p> <p>Master of Science (M.S.), Mechanical Engineering, <i>University of Illinois at Chicago, Chicago-Illinois</i>, 2018</p>
Work Experience	<p>Graduate Research Assistant, UIC - Lynch Laboratory, <i>University of Illinois at Chicago, Chicago- Illinois</i>, 2017-2018</p> <p>Engineering Intern – Manufacturing Engineering, <i>Bharat Dynamics Limited, Hyderabad-India</i>, 2015</p>
Membership	Society of Automotive Engineers (SAE), <i>Formula SAE team member</i> (2014-2016)